N° d'ordre 199-2009
LYCEN – T 2009-19

Thèse

présentée devant

l'Université Claude Bernard Lyon-I

Ecole Doctorale de Physique et d'Astrophysique

pour l'obtention du

DIPLOME de DOCTORAT
Spécialité : Physique des Particules

(arrêté du 7 août 2006)

par

Silvia SCORZA

EDELWEISS-II, direct Dark Matter search experiment : first data analysis and results

Soutenue le 6 novembre 2009
devant la Commission d'Examen

Jury :	M.	B.	Ille	Président du jury
	M.	J.	Gascon	Directeur de thèse
	M.	G.	Gerbier	
	M.	A.	Giuliani	Rapporteur
	M.	J.	Jochum	Rapporteur

Acknowledgements

Many people have followed directly and indirectly my work and my ventures during these years in Lyon. I owe much to them, but first of all I would like to thank my supervisor Jules Gascon for being always present and patient enough to answer my questions, willing to help me with suggestions and encouragement whenever I needed it. I am also very grateful to him for communicating to me the greatest enthusiasm for research.

I am glad to thank the EDELWEISS collaboration especially the astroparticle group in Lyon for the warm welcome, for always giving me valuable suggestions about my work and career and for their help and patience.

I would like to thank the members of the committee, Bernard Ille, Gilles Gerbier and Jules Gascon and in particular a special thank to the referees, Andrea Giuliani and Josef Jochum, for having read and evaluated my work and provided me with fruitful and valuable comments.

I will remain grateful to my officemate Marc-Antoine for putting up with me in comic and tragic circumstances, and for amusing me with interesting discussions in both cases. I am also grateful to the whole third floor for thoughtfully tolerating the aforementioned discussions and my singing performances from the adjacent offices. Un grand merci aux services techniques du laboratoire, en particulier l'équipe informatique, pour leur soutien.

I would like to greatly thank all my friends and colleagues at IPNL and elsewhere for being always nice and fun and helping me to enjoy the past three years.

Tout d'abord je remercie les doctorants et non-doctorants qui ont su transformer en moments très conviviaux les repas de midi, pauses, goûters, etc, etc, toutes ces choses qui rendent le quotidien agréable e un particolare ringraziamento all'irriducibile gruppo di italiani del laboratorio (Silvia, Federica, Giulia, Marco, Mauro, Giacomo e Silvano) sempre presente.

Un merci special à Myriam, une amie très chère toujours prête à rigoler et qui a su me remonter le moral dans mes phases de down. Les soirées, le Martini, les bières, la musique, les enceintes, la chevalerie et la ritirata.

Un merci à qui m'a accompagné dans mes pauses cafés éternelles avec des sujets de conversation passionants et les bâillements qui vont avec.

Come dimenticare gli ex compagni di studio di Genova, Ilaria, Tommaso, Lorenza, Enrico, Andrea e Leo, ottimi amici dispersi per il mondo; Valeria e Marta divise tra Padova e Genova ma sempre presenti e la coppia Franceschini-Ponzano che hanno saputo rallegrare le ormai rare serate genovesi.

Infine ringrazio di cuore la mia famiglia: in primis i fratelli Simo e Ste per il loro buonumore contagioso, per il supporto costante sebbene a distanza e per le chiacchierate ed i consigli ed i miei genitori per avermi sempre sostenuto, appoggiato e sopportato anche nei momenti di maggior tensione, ultimamente frequenti.

Contents

Introduction

One of the greatest mysteries of the universe that, for the present, puzzles the mind of most astronomers, cosmologists and physicists is the question: "What makes up our universe?". This is due to how a certain substance named Dark Matter came under speculation. It is believed this enigmatic substance, of type unknown, accounts for almost three-quarters of the cosmos within the universe, could be the answer to several questions raised by the models of the expanding universe astronomers have created, and even decide the fate of the expansion of the universe.

A great deal of effort has been made since 1687, when Newton introduced the notion of gravity discussing it in terms of forces between "bodies" (i.e. visible baryonic objects) stating in the introduction of his " *Philosophiae Naturalis Mathematica*" that "I have no regard in this place to a medium, if any such there is, that freely pervades the interstices between the parts of bodies". Since then, the deviations of observed motions from expected trajectories have proved very effective in deepening our understanding of universe. Whenever anomalies were observed in the motion of planets in the Solar system, the question arose: should such anomalies be regarded as a refutation of gravitation laws or as an indication of the existence of unseen objects?

The modern problem of dark matter is conceptually very similar at the old one about unseen planets: we observe in large astrophysical system at all length scales, from galactic to cosmological one, some inconsistencies that can only be explained either by assuming the existence of a large amount of invisible, *dark*, matter, or by assuming a deviation from the well-known gravitation laws and the general relativity theory.

There is strong observational evidence for the dominance of non-baryonic Dark Matter (DM) over baryonic matter in the universe. Such evidence comes from many independent observations over different length scales. The most stringent constraint on the abundance of DM comes from the analysis of the Cosmic Microwave Background (CMB) anisotropies. In particular, the WMAP (Wilkinson Microwave Anisotropy Probe) experiment restricts

the abundance of matter to lie in the range $\Omega_M h^2 = 0.1358^{+0.0037}_{-0.0036}$ and the abundance of baryonic matter to be in the range $\Omega_b h^2 = 0.02267^{+0.00058}_{-0.00059}$ [1], in good agreement with predictions from Big Bang Nucleosynthesis $0.018 < \Omega_b h^2 < 0.023$ [2].

It is commonly believed that such a non-baryonic component could consist of new, as yet undiscovered, particles, usually referred to as WIMPs (Weakly Interacting Massive Particles). Some extensions of the standard model (SM) of particle physics predict the existence of particles that would be excellent DM candidates. In particular great attention has been dedicated to candidates arising in supersymmetric theories: the Lightest Supersymmetric Particle (LSP). In the most supersymmetric scenarios, the so-called *neutralino* seems to be a natural candidate, being stable in theories with conservation of R-parity and having masses and cross sections of typical WIMPs.

One way of probing the nature of dark matter particles is to look for their annihilations signal [3]. A wide literature exists discussing the prospects of observing annihilation radiation from the galactic centre, high energy neutrinos from the Sun, gamma-rays and synchrotron from dark matter clumps in the galactic halo, gamma-rays from external galaxies, positrons and antiprotons and more. Large uncertainties are associated with predictions of annihilation fluxes, due to our poor knowledge of the distribution of dark matter, especially in the innermost regions of Galaxy. Other promising strategies include collider searches for dark matter and associated particles and direct detection experiments designed to observe the elastic scattering of dark matter particles with nuclei.

I would like to emphasize that the detection of dark matter particles in any one of the experimental channels discussed will not alone be sufficient to conclusively identify the nature of dark matter. The direct or indirect detection of the dark matter particles making up our galaxy's halo is highly unlikely to provide enough informations to reveal the underlying physics (supersymmetry, etc.) behind these particles. In contrast, collider experiments may identify a long-lived, weakly interacting particle, but will not be able to test its cosmological stability or abundance. We should solve the mystery of dark matter particle nature only by combining the information provided by many different experimental approaches.

The EDELWEISS collaboration is a direct dark matter search experiment, aiming to detect directly a WIMP interaction in a target material, high purity germanium crystal working at cryogenic temperatures. It relies in the measurement of nuclear recoils that produce measurable effects in the crystal such ionization and heat.

This thesis is organized as follows. The **first chapter** aims to provide an introduction to the theoretical framework and the scientific motivation for the

following work. The nature of DM has been one of the most challenging topics in contemporary physics since the first evidences of its existence had been found in the 1930s. Cosmologists and astrophysicists on one side, together with particle theorists on the other have put a lot of effort into this field: I will briefly account for their achievements and for the experimental strategies which can be set in this scenario. Since this thesis work was carried out within the EDELWEISS-II direct dark matter experiment, I will focus the next chapter on this topic, describing the main features.

The **second chapter** is related to the set-up of the EDELWEISS-II, the current stage of the EDELWEISS experiment necessary after a first phase that achieved the best upper limit on the WIMP elastic scattering on nucleon as a function of WIMP mass in 2004 [4]. The set-up was conceived to reduce radioactive background observed in the first experiment phase. Thus, describing the starting point for this second stage, I will present detectors involved in, with a peculiar regard to the Ge-NTD type, the same implied in EDELWEISS-I, on which I have focused my thesis work.

In the **third chapter** the performed Ge-NTD analysis chain is presented. Starting with the signal processing of the recorded data, I will enter in the essential analysis steps from calibration signals passing through measurements of thresholds and resolutions in order to predict nuclear and electronic recoil band and definition of fiducial zone to conclude determining a selection for likely WIMP candidate.

These suggestions are applied in the **fourth chapter**, which presents the analysis and the results of the 8^{th} cool down that takes places from November 2007 to March 2008. This cool down allows a first real look at the EDELWEISS-II environment and it represents a first real test of Ge-NTD type detectors at large scale. Thus, it follows that two goals are envisaged: a better understanding of radiative background overwhelming the experiment and an improvement of current upper limit on the WIMP scattering cross section.

Chapter 1

Dark Matter Challenge

1.1 Theoretical framework

In this section I will briefly present theoretical ingredients to make up a cosmological model in order to understand why we need a dark matter contribution in universe. Included short history of universe is drawn.

1.1.1 Standard Cosmology

Following the progress in technologies of experiments measuring cosmological parameters, a lot of cosmological models have been proposed even if most cosmologists agree on a fundamental picture, the *Big-Bang* scenario. It describes the universe as a system evolving from a highly compressed state existing about 10^{10} years ago, experimentally well motivated by Hubble's law discovery [5]. This model explains in a satisfactory way most of properties of universe, such as its thermal history, background radiation and abundance of elements. A cosmological model is composed by three fundamental ingredients:

- *Einstein's equation*, relating the geometry of the universe with its matter and energy content;
- *Metrics*, describing the symmetries of the problem;
- *Equation of state*, specifying the physical properties of the matter and energy content

For the Einstein field equation we need to assume three hypothesis: firstly, the equation is invariant under general coordinate transformations, the equation has to tend to Newton's law in the weak field's limit and lastly the

equation is of second differential order and linear in the second derivative [6]. The resulting equation is generally written:

$$R_{\mu\nu} + \frac{1}{2} g_{\mu\nu} R = -\frac{8\pi G_N}{c^4} T_{\mu\nu} + \Lambda g_{\mu\nu} \tag{1.1}$$

where R and $R_{\mu\nu}$ are respectively the Ricci scalar and tensor (obtained by contraction of the Riemann curvature tensor), $g_{\mu\nu}$ is the metric tensor, G_N the Newton's constant, $T_{\mu\nu}$ is the energy-momentum tensor and Λ is the so-called cosmological constant. If we ignore for a little while the term concerning the cosmological constant, the equation Eq. (1.1) is pretty well understood. It relates the geometry of the universe, described by the left-handed side terms, to its energy content. It characterized by the energy-momentum tensor on the right-handed side resulting in the well known relationship between matter content and geometry of the universe: the key concept of general relativity.

The cosmological constant term, firstly introduced by Einstein to have a stationary solution for the universe and afterward abandoned due to the universe's expansion discovery, represents a "vacuum energy" more related to time-space itself rather than its matter content. It is a source of gravitational field even in the absence of matter. Usually we assume an universe with properties of homogeneity and isotropy as symmetry of the problem, made for mathematical convenience. Such properties have been confirmed by many observations; in particular, observations of the Cosmic Microwave Background (CMB) have shown remarkable isotropy, once the contribution from galactic plane and the dipole component were subtracted. Isotropy alone if combined with Copernican principle [1] would imply homogeneity. However, direct evidence of homogeneity comes from galaxy surveys, suggesting a homogeneous distribution in excess at scales of $\sim$100 Mpc; it means that any $>$ 100 Mpc diameter sphere centered in any place of the universe should contain the same amount of matter.

The properties of isotropy and homogeneity and the assumption that spatial component of metric can be time dependent imply a specific metric. The line element in reduced-circumference polar coordinates can be expressed as:

$$ds^2 = -c^2 dt^2 + a(t)^2 \left(\frac{dr^2}{1 - k\ r^2} + r^2 d\Omega^2 \right), \tag{1.2}$$

[1] it state the Earth is not in a central, specially favored position, afterwards generalized to the relativistic concept that humans are not privileged observers of the universe

where $d\Omega^2 = d\Theta^2 + \sin^2\Theta d\phi^2$ and r, Θ and ϕ are the (fixed) comoving coordinates carried by the fundamental observers. In succession, $a(t)$ is the scale factor and the constant k, describing the spatial curvature can vary between k= -1, 0, +1. For the simplest case, k=0, the Eq. (1.2) comes back to the metric of ordinary (flat) Euclidean space. The Einstein equation can be solved with this metric and its time-component lead to the Friedmann equation, having the following form:

$$\left(\frac{\dot{a}}{a}\right)^2 + \frac{k}{a^2} = \frac{8\pi G_N}{3}\rho_{tot}, \tag{1.3}$$

where ρ_{tot} is the total average energy density of the universe: it consists in the sum of matter, radiation and vacuum energy density contribution $\rho_{tot} = \rho_m + \rho_r + \rho_\Lambda$. In particle physics units, $\hbar = c = 1$, the Newton's constant G_N has the same order of magnitude of an inverse squared mass, the Plank mass whose value is 1.22×10^{19} GeV.

Since only relative changes have measurable effects and thus the whole scale factor value is arbitrary, it is common to introduce a parameter H that depends on time according to the following formula

$$H(t) = \frac{\dot{a}(t)}{a(t)} \tag{1.4}$$

and that manages the local expansion as stated by the Hubble's law, $v = Hd$, where v is the recession velocity and d the physical distance. Recent astrophysical observations [7] sets the present value of the Hubble parameter to $H_0 = 73 \pm 3$ km s^{-1} Mpc^{-1} (1 Mpc$\sim$3.1 10^{22} m). We can notice from the Eq. (1.3), we have a flat universe (k=0) when the energy density is equal to a critical density, ρ_c:

$$\rho_c \equiv \frac{3H^2}{8\pi G_N} \tag{1.5}$$

Usually the abundance of a substance in the universe (matter, radiation or vacuum energy) is normalized to ρ_c, so we thus define a quantity Ω_i of a substance of species i and density ρ_i as

$$\Omega_i \equiv \frac{\rho_i}{\rho_c} \tag{1.6}$$

So for the total amount in the universe it is normal to define

$$\Omega = \sum_i \Omega_i \equiv \sum_i \frac{\rho_i}{\rho_c}, \tag{1.7}$$

$\rho < \rho_c$	$\Omega < 1$	k = -1	Open
$\rho = \rho_c$	$\Omega = 1$	$k = 0$	Flat
$\rho > \rho_c$	$\Omega > 1$	$k = 1$	Closed

Table 1.1: Classification of cosmological models according to averaged density value (ρ) in units of the critical density (ρ_c).

that allows a re-styling of the Friedmann equation, Eq. (1.3), as follow

$$\Omega - 1 = \frac{k}{H^2 a^2}. \tag{1.8}$$

The sign of k is therefore determined by the value that Ω can assume (see Tab. 1.1).

1.1.2 History of the universe in a nutshell

According to the Big Bang model, universe originates in an explosion after which every single particle started to quickly move away from other particles behaving like a hot gas of fundamental particles in fast expansion. The early universe description is based on the extrapolation of the known physics up to the Plank era at time $t \simeq 10^{-43}$ s, that means in terms of energy the gravitational interaction began strong at the order of Plank mass $M_{Pl} \simeq 10^{19}$ GeV. Starting at this epoch the universe evolution can be described by the following phase transitions:

* T $\sim 10^{16}$ GeV First phase transition: The Grand Unification (GUT: Grand Unified Theory) epoch ends up. The single unified field in which the strong nuclear, the weak nuclear and the electromagnetic forces were fused breaks down into Standard Model groups. The electroweak epoch began: strong and electroweak forces (weak nuclear and electromagnetic force) are different; some models predict that such epoch get under way with an hyper expansion of the universe (inflation). Quarks and leptons are distinct entities and bosons can decay into them leading an asymmetry between matter and anti-matter.

* T $\sim 10^2$ GeV Second phase transition: electroweak symmetry breaking, electromagnetic and weak forces are no longer unified. This breaking could be the origin of baryogenesis [8] and of primordial magnetic field [9].

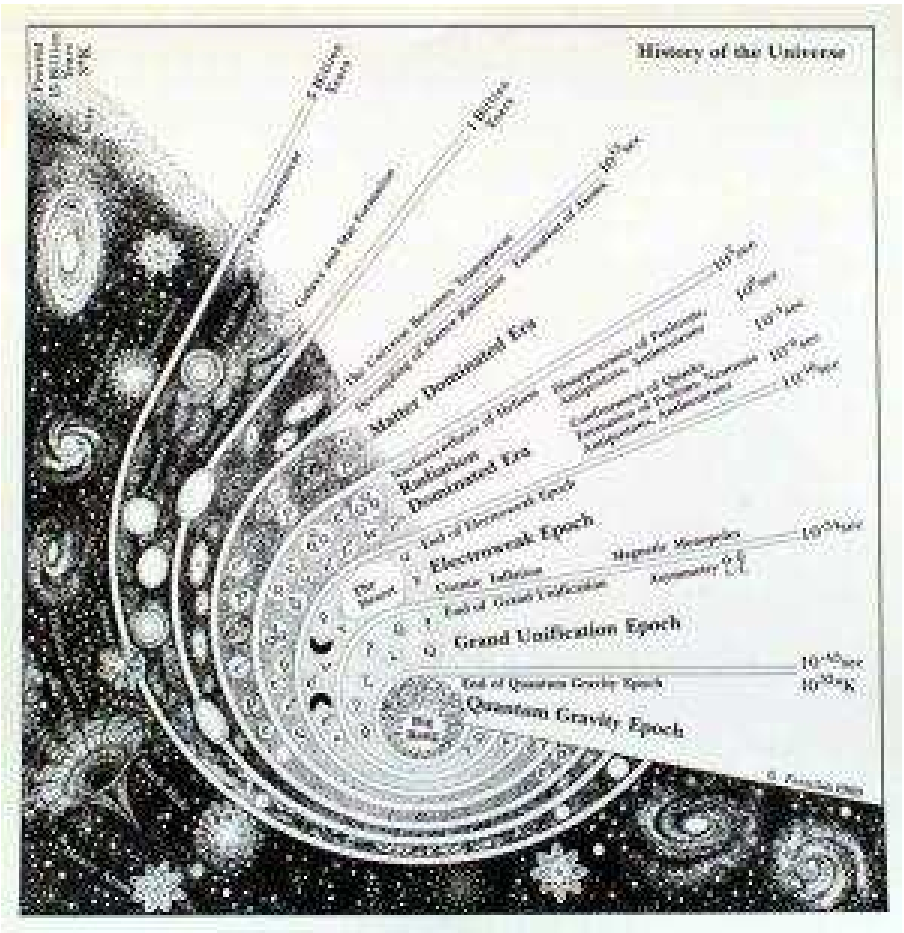

Figure 1.1: History of universe (http://home.fnal.gov/ dawson/themes/backgrounds/tall/history.universe.jpg).

* T $\sim$ 10^1-10^3 GeV Quark-antiquark (q-$\bar{q}$) annihilation occurs: weakly interacting dark matter candidates with GeV-TeV scale masses freeze-out.

* T $\sim$ 0.3 GeV QCD phase transition: confinement of quarks and gluons into hadrons.

* T $\sim$ 1 MeV Neutrinos decoupling, neutrons freeze-out and e^+-e^- annihilations occur.

* T $\sim$ 100 keV Nucleosynthesis: protons and neutrons fuse into light elements (D, ^{3}He, ^{4}He, Li). The Standard Big Bang nucleosynthesis provides by far one stringent constraints to the Big Bang theory and predictions agree with observations, see Fig. 1.7.

* T $\sim$ 1 eV Matter and radiation densities are equal: the structure formation begins.

* T $\sim$ 0.4 eV Photon decoupling produces cosmic background radiation (CMB).

* T=2.7 K $\sim$ 10^{-4} eV Today.

1.2 Motivations and evidences for Dark Matter

The first interest in a matter which does not emit radiation having no coupling with photon ("dark") and thus can be observed only by its gravitational effects dates back to Öpik's 1915 studies about dynamical matter density in the Solar vicinity [10]. The current connotation of dark matter appears in 1933, in the first Zwicky's work on the dynamics of galaxies in the Coma cluster [11]. Since then astrophysical evidences of the presence of some "mass excess" with respect to the visible fraction accumulate throughout the ages, while cosmologists and particles physicists seek to fit observations into a theoretical structure. The cold dark matter scenario was then established as a likely cosmological explanation [12], while on the particle side the debate is still wide open. Here I outline the main dark matter evidences from an observational point of view [13].

1.2.1 The galactic scale

The most direct and intelligible evidence for DM comes from observation of the rotation curves of galaxies, i.e. the well-known plot of stars and gas circular velocities versus their distance from galactic center as shown in Fig. 1.2

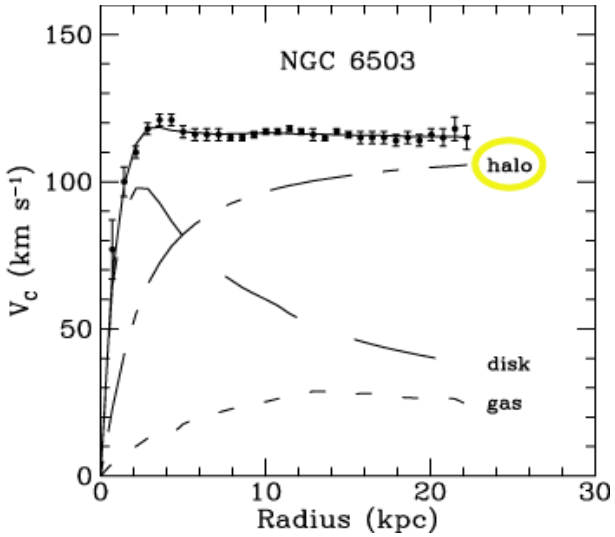

Figure 1.2: Rotation curve of NGC6503. Figure from [14].

(Fig. 1.3 gives a visual explanation of this evidence). A simple Newtonian approach gives:

$$v(r) = \sqrt{\frac{GM(r)}{r}} \tag{1.9}$$

where $M(r) \equiv 4\pi \int \rho(r)\dot{r}^2 dr$ and $\rho(r)$ is the mass density profile that should be falling $\propto 1/\sqrt{r}$ beyond the optical disc. If the matter density was given only by the known visible mass, one would expect the velocity to fall like $1/\sqrt{r}$ outside the galactic disk. Instead, experimental data show that the velocity keeps a constant trend even far beyond the visible disk, probing the existence of a dark matter halo with $\rho(r) \propto 1/\sqrt{r^2}$. The density profile of the innermost part of the spherical halo is still unknown. However adding a dark matter halo allows a good fit to data.

The standard method used to measure masses is to balance the kinetic and potential energies using the virial theorem [2].

Limitations of rotations curves arise from the fact that one can only look out as far as there is light or neutral hydrogen (21 cm), namely to distances of tens of kpc. Therefore, we can see the beginnings of DM halos, but cannot trace where most of DM is. Lensing experiments go beyond these limitations,

[2]It provides a general equation relating the average over time of the total kinetic energy of a stable system, bound by potential forces, with that of the total potential energy. A description in Subsection. 1.2.2

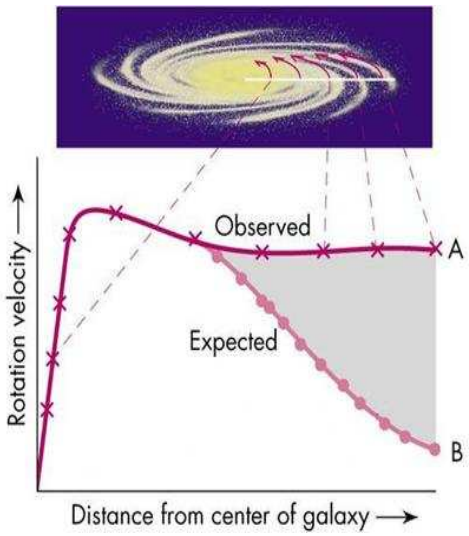

Figure 1.3: Explanation of the rotation curves of galaxies (http://philica.com/uploads/images/145/Image/image006.jpg).

see next section.

1.2.2 Galaxy cluster scale

As we have already seen, the first DM evidence came from a much larger scale than that of a single galaxy (out to tens of kpc), the Coma galaxy cluster. Galactic clusters are aggregates of a few hundred to a few thousand galaxies, gravitationally bound to each other and otherwise isolated in space. The relative contribution of dark matter component in a galactic cluster is specified by the Mass-to-Light Ratio (M/L), that represents the ratio of gravitational mass and luminosity for an object. Studies of the M/L ratio at different scales confirmed that these structures are utterly dominated by non luminous matter since the M/L ratio increases from the luminous parts of galaxies to their fainter halos, and increases further when considering local groups of galaxies and galaxy clusters [15]. The method used to determine the mass-to-light ratios from galaxy clusters includes measuring the velocities of individual galaxies in the clusters at dynamical equilibrium [16] and estimating the total cluster mass from the virial theorem. According to this theorem the kinetic and potential energies of a system are related by the following equation

$$\langle T \rangle = -\frac{1}{2}\langle V \rangle \tag{1.10}$$

where $\langle T \rangle$ is the average kinetic energy derived from the dispersion in the velocities and $\langle V \rangle$ is the average potential energy. The latter is used to determine the mass of the cluster.

The X-ray emission of hot intra-cluster gas, assumed to be at hydrostatic equilibrium, can also be used to estimate the mass of cluster [17]. X-ray profiles of the gas are measured and then fit to temperature and density distribution models to determine the mass of the cluster.

The mass of a cluster can also be determined by gravitational lensing method [18]: general relativity in fact states that compact gravitational bodies bend nearby photon paths (namely, make a space-time geodesic curve) and thus act as lenses for light sources behind them in the line of sight. Thus, when light rays pass through large gravitational masses such as galaxy clusters they are deflected by the gravitational field produced by the cluster, in a manner similar to the way an optical lens bends light to form an image. By analyzing the amount of bending of light, we can be able to determine the cluster mass. The estimates show that there is far more mass exerting gravitational effect than suggested by luminous matter. Figure 1.4 illustrates the gravitational lens effect produced by Cluster 0024+1654 as seen through Hubble Space Telescope.

1.2.3 Cosmological scale

The experimental evidence presented earlier indicates that a substantial part of the universe is made up of a non luminous component. By considering the constraints set on the amount of luminous matter in the universe based on astronomical observations of galaxies and galaxy clusters alone, we conclude that $\Omega_{lum} \sim 0.005$. Measurements of clusters are consistent with a matter density of the universe $\Omega_m = 0.341^{+0.031}_{-0.029}$[19]. In summary, the evidences are overwhelming for the existence of an unknown component of DM that comprises 95% of the mass in galaxies and clusters.

The cosmic abundances tell a consistent story in which the preponderance of the mass in the universe consists of an unknown DM component. The Cosmic Microwave Background provides the most powerful measurements of the cosmological parameters. Primordial nucleosynthesis restricts the abundance of baryonic matter, and Type IA supernovae provide powerful evidence for the acceleration of the universe, possibly explained by Dark Energy as the major constituent of the cosmic energy density.

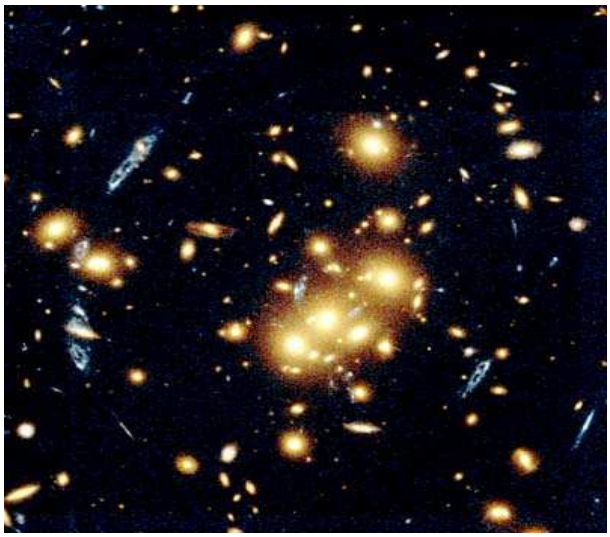

Figure 1.4: Image of galaxy cluster 0024+1654 taken by the Hubble Space Telescope demonstrates gravitational lensing by large galaxy cluster. Light from distant galaxies passes by the gravitational cluster's mass and gets bent, creating a lensing effect. Figure from [18].

The Cosmic Microwave Background (CMB) Further evidence for dark matter comes from measurements on cosmological scales of anisotropies in the CMB. The CMB is the remnant isotropic radiation from the hot early days of the universe.

By studying this radiation, we are able to examine the conditions in the universe 400000 years after the Big Bang, known as the "surface of last scattering". Though the virtual isotropy of the CMB is better than one part in 10^5, there exist tiny ripples in the temperature of microwave sky which provide us information about the seed fluctuations that existed at the time of the decoupling of matter and radiation, much prior to the formation of galaxy structures. These seed fluctuations grew by gravitational attraction into the stars, galaxies and galaxy clusters we see today. Measurements of the anisotropies in the CMB may thus be employed to determine various cosmological parameters.

There have been different studies in recent years of the angular anisotropy power spectrum of the CMB characterizing the size of the temperature fluctuations. Peaks in the power spectrum are indicative of the harmonics in the sound waves that filled the early universe. Until 400000 years after the Big Bang, the universe was so hot that matter and radiation were entangled in a primordial soup in which sound (pressure) waves could vibrate. At the time

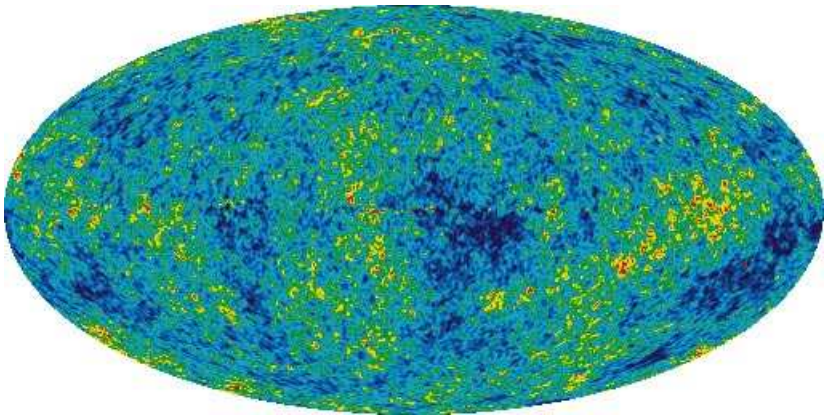

Figure 1.5: Full sky maps of the cosmic microwave background anisotropy. Figure from http://map.gsfc.nasa.gov/.

of the decoupling of matter and radiation, these pressure waves left traces of their existence in the temperature fluctuations seen in the CMB radiation today, see Fig. 1.5.

Cosmological models predict the existence of acoustic peaks in the angular power spectrum, see Fig. 1.6. The relative position and height of the peaks provide estimates on Ω and Ω_m. Studies of the peaks in the CMB angular anisotropy power spectrum by experiments such as DASI [21] and MAXIMA [22] point to $\Omega_m + \Omega_\Lambda \simeq 1$, suggesting a flat universe. This has been corroborated by the Wilkinson Microwave Anisotropy Probe launched in 2001 to study the microwave background sky with unprecedented accuracy. From WMAP data combined with the distance measurements of Type Ia Supernovae (SN) and Baryon Acoustic Oscillations (BAO) in the galaxy distribution, we find (at 68% C.L.. uncertainties) the following values for the abundance of baryons and matter [1]:

$$\Omega_m h^2 = 0.1358^{+0.0037}_{-0.0036}; \quad \Omega_b h^2 = 0.02267^{+0.00058}_{-0.00059} \tag{1.11}$$

that is to say, roughly speaking, that ordinary matter ("baryons") accounts only for 1/6 of the total matter density in the universe, the other 5/6 being attributed to dark matter. WMAP collaboration derives also the value of $\Omega_m = 0.27 \pm 0.04$ and of the vacuum energy density $\Omega_\Lambda = 0.73 \pm 0.04$ compatible with a flat universe. The value of $\Omega_b h^2$ thus obtained is consistent with predictions from Big Bang Nucleosynthesis [2].

$$0.018 < \Omega_b h^2 < 0.023 \tag{1.12}$$

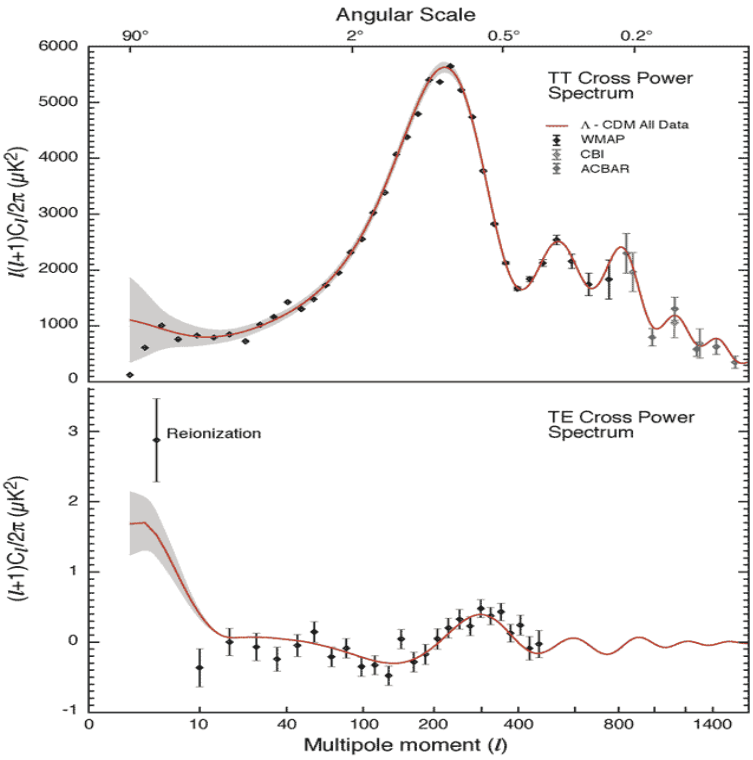

Figure 1.6: The WMAP angular power spectrum. The curve is the consensus cosmology model; the gray band includes cosmic variance. Figure from [20].

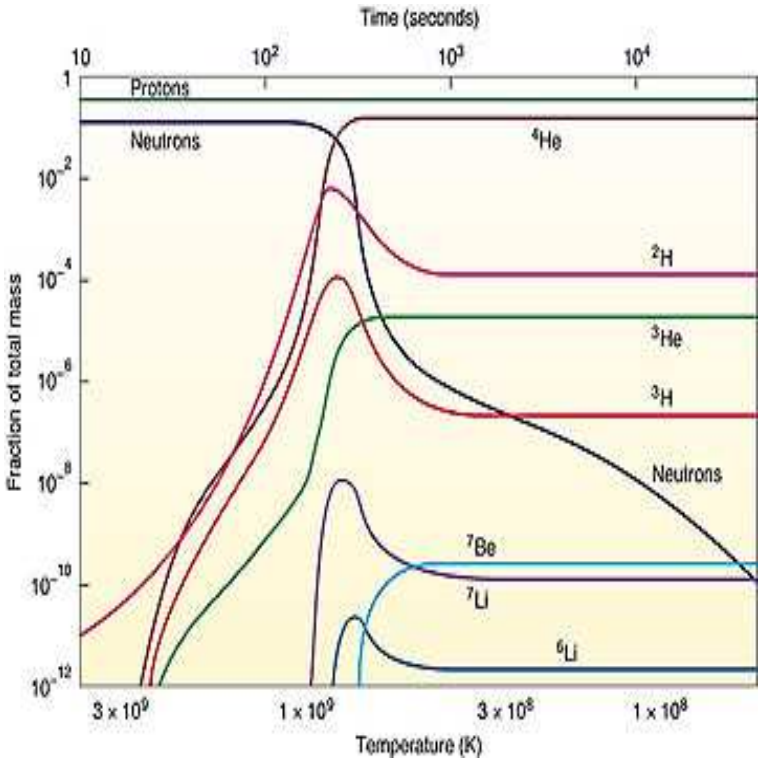

Figure 1.7: Evolution of light elements abundances over time (or temperature). When the universe has cooled sufficiently, the light elements are not dissociated by the energetic photons. Nucleosynthesis proceeds until the supply of free neutrons is exhausted. Figure from [25].

Primordial Nucleosynthesis To determine the nature of most of this dark matter, we turn to Big Bang Nucleosynthesis. This term refers to the calculations of the abundances of the light elements such as ^2H, ^3H, ^4He and ^7Li relative to photons within the framework of the Big Bang model describing the universe [23], [24]. Less than one second after the Big Bang, the neutron-to-proton ratio is maintained in thermal equilibrium through the following reactions:

$$p + e^- \longleftrightarrow n + \nu \tag{1.13}$$

$$n + e^+ \longleftrightarrow p + \nu \tag{1.14}$$

About 1 second after the Big Bang these reactions become slower than the expansion rate of the universe, and the neutron-to-proton ratio freezes out at about 1:7. The temperature of the universe falls from the pheno-

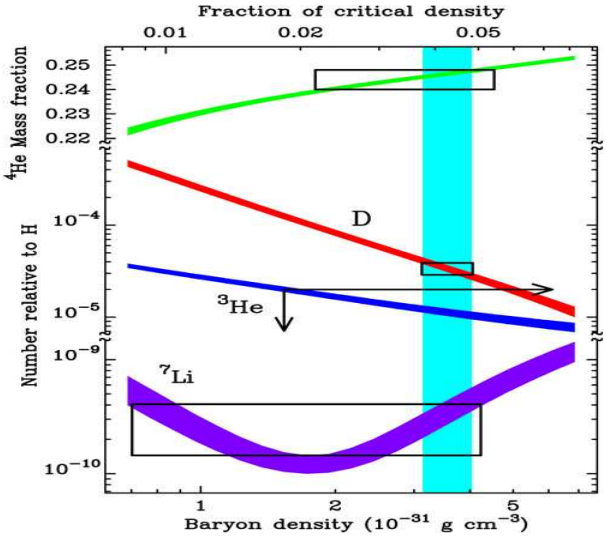

Figure 1.8: The predicted abundance of the light elements as a function of baryon density. The vertical band indicates the narrow range of baryon densities consistent with the deuterium measurements; the boxes (the arrows for ^3He) indicate the range in baryon density (horizontal extent of box) that is consistent with the measured light-element abundance (vertical extent of box). The overlap of the boxes with the deuterium and indicates the general consistency of the observed abundances of the other light elements with their predicted abundances for this baryon density. Figure from [25].

menally hot 10^{32} Kelvin to 10^9 Kelvin, below the nuclear binding energies, suppressing the number of photons with energies high enough to disassociate these nuclei. Light elements begin to form. Figure 1.7 gives the evolution of the abundances of light elements over time (and temperature) in the first few minutes after the Big Bang.

By the time the temperature of the universe fell to T≈0.003 MeV, the light elements ^4He, ^3He, ^3H, ^7Li and ^7Be have established their final abundances.

When all neutrons have been used, the intermediate nuclei do not form but the reactions, through which they combine, continue. The amount of leftover deuterium is very sensitive to the density because this gets frozen in once the processes through which the deuterium and other elements that form helium stop. Hence, the neutron-to-proton ratio set at the time of the freeze out is important in deciding the final abundances of these elements in the early universe. For a neutron-to-proton ratio of 1:7 the time of the formation of these elements, 25% of the mass of universe ends up in Helium. Measurements of the abundance of light elements in the universe

can, therefore, place limits on the baryonic density. Increased accuracy in astrophysical measurements have placed tighter constraints on the baryonic matter-density. These include studies of quasars [25] and the abundance of ^2H in high redshift clouds [26]. Current measurements corroborate the WMAP results constraining the baryonic matter density in the range deduced by Eq. (1.12).

Given our knowledge of the matter density $\Omega_m \simeq 0.3$, this suggests that most of the matter in the universe is non-baryonic in nature. The density of ordinary baryons within a narrow range is the predicted production consistent with what is actually measured, see Fig. 1.8. BBN theory and baryonic dark matter density measurements, combined with CMB measurements, suggest that non-baryonic dark matter is an important component of matter in the universe.

Dark Energy Evidence for the 70% dark energy in the universe comes from observations of distant supernovae ([27] and [28]). The further supernovae are dimmer than expected, as is most easily explained by an accelerating universe. There are two different approaches to the dark energy:

- a vacuum energy such as a cosmological constant or time dependent vacuum may be responsible [29];
- it is possible that General Relativity is incomplete and that Einstein's equations need to be modified ([30] and [31]).

Note, however, that this dark energy does not resolve or contribute to the question of dark matter in galaxies.

1.3 The WIMP Hypothesis

In this thesis, I limit the discussion to dark matter candidates which are heavy, electrically neutral and weakly interacting. This class of particles, known as WIMPs, is particularly well motivated by their thermal history. At sufficiently early times after the Big Bang, when the temperatures are greater than the mass of the particle, $T \gg m_\chi$, the equilibrium number density of such particles is $n_\chi \propto T^3$, but for lower temperatures, $T \ll m_\chi$, the equilibrium abundance is exponentially suppressed, $n_\chi \propto \exp^{-m_\chi/T}$. If the expansion of the universe were slow enough that thermal equilibrium were always maintained, the number of WIMPs today would be infinitesimal. But since the universe is not static so we have to take into account non-equilibrium thermodynamics.

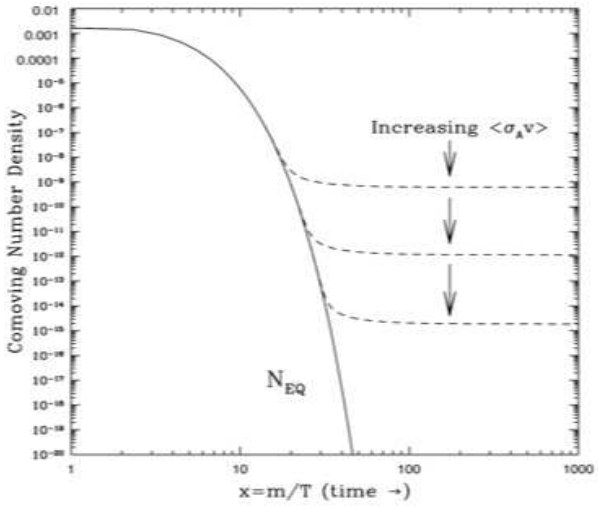

Figure 1.9: A thermal relic starts in LTE (Local Thermodynamic Equilibrium) at T » m_X. When the rates keeping the relic in chemical equilibrium become smaller than the expansion rate, the density of the relic relative to the entropy density becomes constant. This is known as *freeze out.* [33]

At high temperatures ($T \gg m_\chi$), χ particle is abundant and rapidly converting to lighter particles and vice versa ($\chi\overline{\chi} \rightarrow l\bar{l}$, where $l\bar{l}$ are quark-antiquark and lepton-antilepton pairs, and if m_χ is greater than the mass of the gauge and/or Higgs bosons, $l\bar{l}$ could be gauge and/or Higgs boson pairs as well). Shortly after temperature T drops below m_χ, the number density of χ drops exponentially and the rate $\Gamma = \langle\sigma v\rangle\, n_\chi$ for annihilation of WIMPs, where $\langle\sigma v\rangle$ is the thermal average cross section σ for annihilation of $\chi\overline{\chi}$ into lighter particles times relative velocity v, drops below the expansion rate, $\Gamma \sim H$.

Now, the χ's cease to annihilate efficiently, they fall out of equilibrium, and a relic cosmological abundance remains. The equilibrium (solid line) and actual (dashed line) abundances of WIMPs per comoving volume are shown in Fig. 1.9 as a function of the fraction $x = m_\chi/T$ which increases with increasing time. As the annihilation cross section is increased, the WIMPs stay in equilibrium longer, so we are left with smaller relic abundance when they do finally freeze out. An approximate solution to the Boltzmann equation yields the cosmological WIMP abundance Ω_χ (in units of the critical density ρ_c) [32],

$$\Omega_\chi h^2 = \frac{m_\chi n_\chi}{\rho_c} \simeq 0.1(\frac{3 \times 10^{-26} cm^3 sec^{-1}}{\langle \sigma v \rangle}) \tag{1.15}$$

The result is to a first approximation independent of the WIMP mass and is fixed primarily by the annihilation cross section.

The WIMP velocities at freeze-out are typically some appreciable fraction of the speed of light. Therefore, from the Eq. (1.15), the WIMP will have a cosmological abundance $\Omega_\chi h^2 \sim 0.1$ today if the annihilation cross section times c is roughly $3{\times}10^{-26}$ cm^3 sec^{-1}, or in particle-physics units (obtained using $\hbar c = 2 \times 10^{-14}$ GeV-fm), 10^{-8} GeV^{-2}. Curiously, this is the order of magnitude one would expect from a typical electroweak cross section,

$$\sigma_{weak} \simeq (\frac{\alpha^2}{m^2_{weak}}) \tag{1.16}$$

where $\alpha \simeq O(0.01)$ is the fine-structure constant and $m_{weak} \simeq O(100\ \text{GeV})$. The numerical constant in Eq. (1.15) needed to provide $\Omega_\chi h^2 \sim 0.1$ comes essentially from the expansion rate (which determines the critical density). This relation between the expansion rate and the electroweak scale suggests that if a new, as yet undiscovered, stable massive particle with electroweak interactions exists, it should have a relic density suitable to provide a good candidate for the dark matter.

This has been the reason encouraging the massive experimental effort to detect WIMPs.

1.3.1 Particle Candidate

The undeniable existence of some kind of substance whose effects are, as far as we know, only gravitational in nature, brought immediately the question of its particle composition. Namely, the dark matter particle candidate must show the following observed proprieties [34]:

1. It must have extremely weak or no electromagnetic nor strong interactions. As a consequence, dark matter cannot cool by radiating photons and thus, unlike baryons, does not collapse to the center of galaxies. In other words, one could state that dark matter is very nearly dissipationless.

2. Assuming it is a thermal component of the early universe, it must be sufficiently cold (non-relativistic) at the epoch of its decoupling from the other thermal species. Simulations show that a *hot* dark matter hypothesis leads to the formation of large scale structures before the

small ones (*top-down* formation), which contradict the astrophysical data.

3. It must account for the measured density Ω_m.

A wealth of WIMP candidates has been proposed, from Standard Model neutrinos to the most exotic ones. In fact, while astrophysical and cosmological constraints are more or less definite, the great uncertainties about what direction to take in order to go beyond the limits of Standard model of Particle make room for fantasy. I will focus my attention on a very limited number of dark matter candidates, conscious anyhow that every choice is somewhat arbitrary, and that the great favor encountered today by the neutralino and other supersymmetric particles, could vanish suddenly if tomorrow a new big discovery points elsewhere.

Neutrino. The first WIMPs considered were massive Dirac neutrinos (particle different from its antiparticle) or Majorana neutrinos (particle coincident with its own antiparticle) with masses in the range of a few GeV to a few TeV; due to the Yukawa coupling which gives a neutrino its mass, neutrino interactions become strong above a few TeV, and the neutrino no longer remains a suitable WIMP candidate [35]. The LEP (Large Electron-Positron) collider exclude neutrino masses below half Z^0 mass. Moreover, heavier Dirac neutrinos have been ruled out as the primary component of the Galactic halo by direct detection experiments [36], and heavier Majorana neutrinos have been ruled out by indirect detection experiments, e.g. [37] and [38], over much of their mass range. Therefore, Dirac neutrinos cannot comprise the halo dark matter [39]; Majorana neutrinos can, but only over a small range of fairly large masses.

Supersymmetric Candidates A much more promising WIMP candidate comes from electroweak-scale supersymmetry [40] (SUSY). SUSY was hypothesized in particle physics to solve Standard Model inconsistencies such as the naturalness problem with fundamental Higgs bosons at the electroweak scale. In the GUT theory, the parameter that controls the Higgs-boson mass must be extremely small, but it may be closer to unity (that it means in particle theory idiom more "natural") in supersymmetric theories. Unification of the strong and the electroweak coupling constant at the GUT scale seems to need SUSY and SUSY seems to be indispensable in theories that unify gravity with the other three fundamental forces.

How SUSY has been created from the well-known Standard Model? It "just" need to enlarge the SM gauge group to a new symmetry group where

bosons and fermions are coupled in common multiplets. Every known particle is then provided a *superpartner* with the same quantum numbers, except spin which differs for 1/2. Since no bosons with the same charge and mass of the electron nor any other superpartners have ever been observed, it is clear that SUSY is broken in the low energy world in which we are supposed to live, and that supersymmetric particles must have masses above current lower bounds (∼100 GeV). Anyhow, this scenario introduces a severe imperfection allowing a supersymmetric particle to mediate a $qq \rightarrow \tilde{l}\tilde{q}$ process, providing thus an efficient channel for proton decay. Current experimental limits on proton lifetime are however on the order of 10^{33} years. Therefore, it has been proposed to add to the SUSY a new discrete symmetry, the *R-parity*, to distinguish ordinary particles (R=+1) from their superpartners (R=-1). If R-parity holds with a broken SUSY, supersymmetric particles can decay only in an odd number of superpartners, plus ordinary particles, preventing thus the proton from decaying and guaranteeing the lightest supersymmetric particle (LSP) to be stable.

We will consider the Minimal Supersymmetric extension of the Standard Model (MSSM) that contains the smallest possible number of fields to give rise correctly to the Standard Model when the symmetry is broken. Without entering into details, here we list the populations in the MSSM

- all ordinary quarks with their spin 0 superpartners (*squarks* $\tilde{q}$);
- all known leptons and their bosonic counterparts (*sleptons* $\tilde{l}$):
- all gauge bosons (gluons, W^i and B) and their fermionic partners (respectively *gluinos*, *Winos* and *Binos*) commonly called *gauginos*;
- the standard Higgs bosons, an additional Higgs doublet with opposite hypercharge and a couple of spin 1/2 *Higgsinos*.

Considering mass eigenstates, electroweak gauginos mix into eight different states: the charged parts of Winos and Higgsinos appear as two couples of *charginos* ($\chi_1^{\pm}$, $\chi_2^{\pm}$), while Bino, the neutral charge Wino and the neutral states of the Higgsinos form four *neutralinos* ($\chi^0_{1,2,3,4}$).

Sneutrino. The supersymmetric partner of standard neutrino should represents an interesting dark matter candidate if its mass was in the energy range from 0.5 to 2.3 TeV. Such a particle, anyway, has a quite large cross section for scattering on nucleons, and hence it should has been already observed by direct detection experiments.

Axino and Gravitino. They are superpartners of particles introduced in extensions of Standard Model and hence they are not present in the MSSM frame. The spin 1/2 partner of axion, the *axino*, and the spin 3/2 *gravitino*, superpartners of the unseen graviton, the gauge boson that mediates gravitational interaction, show similar phenomenology as WIMP candidates. Depending on the SUSY model adopted and on the early universe conditions, axino or gravitino can be the LSP, although their lightness could originate rather a "warm" dark matter.

Lightest Neutralino. The lightest of the four neutralinos, χ_1^0, usually referred to simply as *the* neutralino (χ), is at the present day regarded as the most suitable WIMP candidate. The features of such a particle, completely developed in a particle physics framework, fit well the astrophysical constraints for dark matter, without need for any *ad hoc* hypothesis. Its mass can range from 150 GeV (electroweak scale) to several TeV. Being the LSP (Lightest Supersymmetric Particle) of the theory, it is stable, since R-parity conservation prohibits every decay process other than self-annihilation. Neutralino has a quite low annihilation rate and it is heavy enough to represent a good dark matter candidate.

1.4 DM Detection

Weakly Interacting Massive Particles (WIMPs) are regarded as the most natural dark matter candidate. They not only can form a background density in the universe, but they will also cluster gravitationally with ordinary stars in the galactic halos. In particular they would be present in our own galaxy, the Milky Way, raising the hope of detecting relic WIMPs directly, by performing experiments on the Earth through elastic scattering of WIMPs off target nuclei or indirectly, looking for by-products of WIMP-WIMP annihilation that occurs either in the Sun or galactic halos.

1.4.1 Indirect Search

The indirect detection technique consists in the observation of radiation produced by WIMP annihilation process. If the flux of decay products detected is higher than the expected value coming from conventional sources, this can be seen as a dark matter annihilation signature. Most of possible annihilation products are already produced by usual sources in large quantities making every kind of excess difficult to reveal. The radiation flux is proportional to the decay rate that depends on the dark matter density squared;

it means that natural interesting zones for searching significant fluxes are regions characterized by high dark matter density.

High density region of galactic halo such as the galactic center could be good amplifiers to detect WIMP annihilation products such as antimatter particles and photons. Astrophysical objects like Sun and Earth could be a good dark matter amplifier to observe neutrinos produced by DM particles scattering off nuclei on Sun and Earth. In this section I describe the role of these experimental programs in the strategy to reveal identity of dark matter.

1.4.1.1 Gamma Rays

Traveling essentially unimpeded from their production site, the photons generated in dark matter annihilation have an advantage over the other indirect detection channel. In particular, gamma rays are not deflected by magnetic fields, potentially providing useful angular information, retaining their spectral information: the spectrum observed on Earth is the same that was generated in the dark matter annihilation. The prospects for identifying dark matter annihilation radiation from the Galactic Center (GC) strongly depends on the WIMP nature, on the unknown dark matter density in the region around the GC and on our understanding of the astrophysical backgrounds.

The telescopes, potentially capable of detecting gamma ray radiation from WIMP annihilation include the satellite-based experiment GLAST [41], [42] and lots of ground based Atmospheric Cerenkov Telescopes such as HESS, MAGIC and VERITAS. GLAST will continuously observe a large fraction of the sky, but with an effective area far smaller than the one possessed by ground-based telescopes. In contrast, ground based telescopes study the emission from a small angular field but with far greater exposure. The gamma rays energy range is also different, while GLAST is able to directly study gamma rays with energies over the range of 100 MeV to 300 GeV, the ground based telescopes are only sensitive to gamma rays with energy greater than $\sim$100 GeV. As a result of this different energy ranges accessible by these experiments, searches for WIMPs lighter than a few hundred GeV are most promising with GLAST while ground based telescopes are better suited for heavier WIMPs.

1.4.1.2 Antimatter

WIMP annihilation in the galactic halo could generate charged anti-matter particles: positrons, anti-protons and anti-deuterons. Unlike gamma rays, charged particles move under the influence of galactic magnetic field, diffusing

and losing energy resulting in a diffuse spectrum on Earth. By studying the cosmic anti-matter spectra, satellite-based experiments such as PAMELA [43] and AMS-02 [44] may be able to identify signatures of dark matter. As compared to antiprotons and antideuterons, cosmic positrons are attractive probes of dark matter: the spectrum samples only the local dark matter distribution and is thus subject to considerable uncertainty than the other anti-matter species.

Unlike gamma ray measurements of the Galactic center or dwarf galaxies, observations of the cosmic positron spectrum (as well as the antiprotons and antideuterons spectra) could potentially provide a measurement of the dark matter annihilation rate over large volumes of space. Therefore, such a measurement could be used to determine the product of the WIMPs annihilation cross section and its density squared, averaged over the sampled volume.

1.4.1.3 Neutrinos

Although dark matter annihilations in the galactic halo produce too few neutrinos to be detected [45], annihilations which occur in the center of the Sun could potentially generate an observable flux of high energy neutrinos [46].

Dark matter particles scatter elastically with and become captured in the Sun. WIMPs can generate neutrinos through a wide range of annihilation channels. Annihilations to heavy quarks, tau leptons, gauge and Higgs bosons can generate neutrinos in the subsequent decay. Once produced, neutrinos can travel to the Earth where they can be detected: muon neutrinos produce muons in charged current interaction with ice or water nuclei inside or near the detector volume of high energy neutrino telescope.

Experiments like MACRO [37], AMANDA [47] and Super-Kamiokande [38] set upper limits on neutrino fluxes coming from the center of Earth and the Sun. Super-K upper limit on neutrino-induced muons above 1 GeV from WIMP annihilations in the Sun is approximately 1000 to 2000 $km^2 \cdot y$ for WIMPs heavier than 100 GeV, and approximately 2000 to 5000 $km^2 \cdot y$ for WIMPs in the 20 to hundred-GeV mass range. The precise value of these limits depends on the WIMP annihilation mode considered. The AMANDA-II [47] and MACRO [37] experiments have each placed limits on the flux of neutrino-induced muons from Sun that are only slightly weaker than Super-Kamiokande's. The neutrino telescopes ICE CUBE [48] will be more sensitive to WIMP annihilation in the Sun while ANTARES [49], with less than one tenth of ICE CUBE effective area, will have the advantage of a lower energy threshold and thus it should be more sensitive to low WIMPs mass.

1.4.2 Direct Search

What kind of assumptions we need to succeed in a direct dark matter search? All that we have to know for direct detection is that the Galaxy contains a halo of WIMPs normally assumed to be of spherical isothermal form with a local density 0.3 GeV·c^{-2}·cm^{-3}, an escape velocity of 650 km·s^{-1}, with rms velocity 279 km·s^{-1} and relative halo-Earth velocity of 235 km·s^{-1}[50].

The direct search principle repose on the elastic scattering of these neutral, non-relativistic particles (WIMPs), off target nuclei of a suitable detector, such that the energy transferred as the resulting nuclear recoil passes through the material can be observed, usually as either ionization, scintillation or heat (phonons). Kinematics and the likely mass range and velocity of the particle implies a nuclear recoil spectrum with energies below ∼100 keV, with an exponential form rising to low energies and with no spectral features. This characteristics, together with the expected low interactions rate of about 1-10^{-6} event kg^{-1}·d^{-1}, impose three essential requirements of WIMP detector technology: low energy threshold ($\leq$ 10 keV $_{recoil}$); large detector mass ($>$ 10 kg) and low particle background of any kind. The latter is carried out by passive and active gamma and neutron shielding, by using materials with greatly reduces radioactive U, Th and K content during the detector construction and preferring deep underground sites to reduce cosmic ray muon-induced neutrons that could otherwise produce nuclear recoils indistinguishable from WIMP.

The coupling of these non-relativistic WIMPs has two terms: a scalar Spin-Independent (SI) part and an axial Spin-Dependent (SD) part [51]. For most SUSY models, SI provides the dominant coupling and thus highest rate. This is because although neutralino-nucleon cross section are substantially much smaller for SI case [52], coherence across the nucleus results in constructive interference which greatly enhances the WIMPs-nucleus elastic cross section for high A targets. The opposite is right for SD where the axial coupling to nucleus which differs for spin interferes destructively: sensitivity to SD interactions requires a target isotope with an unpaired nucleon, either proton or neutron.

Knowing that, for instance, typical ambient environmental gamma fluxes can produce event rate $>10^5$ times higher than the expected WIMP signal rate in an unshielded detector, many efforts have been made from the low background point of view focusing the attention on technologies that can actively reject electron recoil events, while maintaining high sensitivity to nuclear recoils. This is possible in principle because nuclear recoils have typically a dE/dx (energy loss per unit pathlength) values ten times higher than the electron. Few technologies can make use of this physics: *low tem-*

perature ionization/phonon or scintillation/phonon detectors in which the ratio event-produced ionization or scintillation to phonons is measured in a suitable cryogenic materials such as Ge or Si (ionization) and $CaWO_4$ (scintillation); *noble liquid gases*, notably Xenon and Argon, in which ionization and scintillation are measured simultaneously. A moderate level of discrimination can be also achieved in specific scintillators such as NaI(Tl), Cs(Tl), liquid Ar and liquid Xe.

Since the recoil discrimination and the background reduction seems to be feasible in such technologies, the main issue that remains to deal with, given the lack of spectral features in the recoil spectrum, is how to determine in a clear way whether any remaining counts are due to WIMPs from the galaxy and not either nuclear recoils form an unaccounted background (neutrons and surface events) or a detector artifact. As WIMP interacts weakly with ordinary matter, no multiple interactions are expected, information that can be used in order to identify neutron, since these latter create as well as a WIMP nuclear recoil. It is also known that WIMP event rate is modulated with a maximum value in June and a minimum in December. Some experiments use this signature. In fact, at least for a standard halo model, the Earth's motion through Galaxy implies an expected seasonal modulation in the recoil spectrum (shape and flux) [53], [54]. This is because the component of the Earth's solar orbital velocity in the direction of our galactic motion (orbital plane inclined at 60^o) either adds to or subtracts from the galactic orbital velocity depending on the season. Unfortunately the annual modulation effect is very small, typically a few %, requiring already at least ton-scale detectors to obtain sufficient event statistic for a viable search [50]. Besides the annual modulation there is also a diurnal modulation proof of the galactic origin of the signal: thanks to our galactic orbital motion ($\sim$235 $km{\cdot}s^{-1}$), we would expect the direction of nuclear recoil induced by WIMPs interaction within a target to be dominantly opposite to our direction of motion (in galactic coordinates), [55], [56].

1.4.2.1 Detection Techniques

In this section knowing the basics and requirements needed for direct dark matter search, I will show how some of the main experiments are being run worldwide. Figure 1.10 provides a summary of results of recent key examples, given here as an exclusion plot of WIMP-nucleon cross section as a function of WIMP mass for the SI case, assuming the standard halo model as above. Referring to this the following sections outline the current status and possible future scenario.

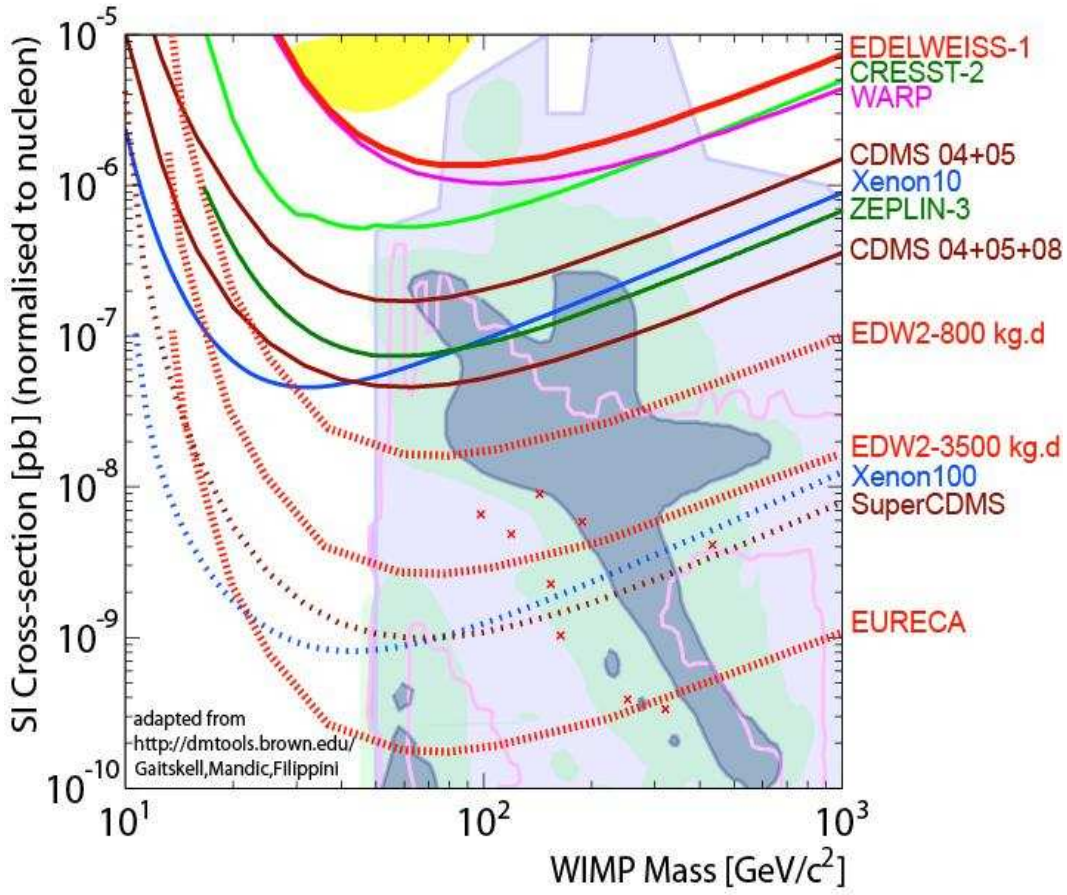

Figure 1.10: Summary of current spin-independent WIMP-nucleon cross section limits (full lines) and some experimental predictions (dashed lines) as a function of WIMP mass compared to a few theoretical predictions.

Semiconductors Ionization detectors, in the form of low background germanium (HPGe) and silicon diodes used for double beta decay searches, provided the first limits on WIMP interactions [57]. Such experiments were vital to ruling out early candidates for WIMPs but as a technology they suffer from the incapability to discriminate gamma background events from nuclear recoil events of interest.

Scintillators When a particle interacts with a scintillating crystal, light is being emitted with photon numbers that are proportional to the energy of the incoming particle. After, light signal is detected by photomultipliers that amplify the light and convert it in an electric signal. The DAMA experiment, located in the Gran Sasso Underground Laboratory, using nine low background 9.7 kg NaI(Tl) crystals found evidence for a modulation, reporting the discovery of the WIMP in 1997 [58]. This signal was confirmed by final DAMA results from a total of 107.73 kg·d [59] remaining the only claimed direct observation of WIMPs, corresponding to a WIMP mass of about 50 GeV and a cross section on proton of 7.2×10^{-6} pb. However, this result appears in contradiction with several other experiments, in fact this kind of WIMP mass and cross section have been excluded firstly by EDELWEISS [60] and then CDMS [61]. Non standard-WIMP models [62], such as light neutralinos, have been investigated in order to reconcile DAMA claims with the limits from the searches, but WIMPs with masses below current limits are excluded by the high-resolution germanium experiment CoGeNT [63]. In addition, assuming WIMPs with dominant spin-dependent cross section on protons contrast with the limits from COUPP [64] and KIMS [65] experiments.

More recently other inorganic scintillators like CsI(Tl) and $CaWO_4$ have been employed in the dark matter search. The KIMS experiment [66], in an underground laboratory in the South Korea uses a CsI scintillating target instead of a $CaWO_4$ crystal become an integral part of the CRESST bolometric experiment in which scintillation light is measured simultaneously with heat [67]. The event by event discrimination is ensured, in this case, by the fact that nuclear recoils have much smaller light yield than electronic one.

For these direct dark matter technology the main disadvantage is represented by the lack of a powerful recoil discrimination.

Directional detectors Definitive proof that a signal origin is galactic and not terrestrial, can only be achieved by correlating in some way events with our motion through the Galactic WIMP halo [55]. However, a much more powerful possibility is to correlate in 3D the physical direction of the nuclear recoils in a target with our motion. This is the motivation behind the

DRIFT [56], MIMAC [68] and other low pressure gas Time Project Chamber (TPC) R&D programs [69]. As currently the only known route to significant recoil direction sensitivity, TPC technology holds exceptional power for WIMP physics and possibly the only route to a definitive galactic signal. However there are several challenges to address, such as the need of low pressure gas implying large volume detectors and the desirability of achieving track head to tail discrimination.

Bolometers At low temperatures the heat capacity of a dielectric crystal goes as T^3. Thus at mK temperatures the small energy deposition from a nuclear recoil can yield a measurable proportional increase in crystal temperature [50]. This is starting idea for the earliest direct dark matter searching techniques, where energy released by particle interactions can be observed as phonons or quanta of lattice vibrations. However it was demonstrated, first in Si [70] and the in Ge [71] that phonon detection could be combined with simultaneous detection of ionization to provide also an event by event discrimination against electron recoils. In fact, because of the dependence of the proportion of energy observed in the two channels on the event dE/dx, a high dE/dx event, such as a recoiling nucleus produces proportionally more heat than ionization (the ionization is quenched). For instance, the ratio of ionization to recoil energy, called the ionization yield, for Ge recoils in Ge is $\sim$0.3 of the value for electron recoils above 20 keV [61].

While the simple phonons detection, that means bolometers without collection of ionization have proven quite useful for dark matter searches, this hybrid technique of simultaneous ionization and phonon measurements with its capability for background rejection has been pushed harder. Most notable is CDMS, [72],[73], (at Soudan mine) and EDELWEISS collaboration (at Frejus), [4], [60].

The EDELWEISS experiment will be completely described in Chapter. 2 being the object of this thesis work.

The CDMS experiment operates towers of Ge and Si crystals each 1cm thick and respectively of mass 250 g and 100 g. These are mounted in a dilution fridge and shielded mainly by 22.5 cm of external Pb and 50 cm of polyethylene. A 5 cm layer of plastic scintillator is used to veto any events coincidence with cosmic muons, necessary due to the relative shallowness of the Soudan site at 2080 m.w.e. Charge electrodes are used for the ionization collection and athermal phonons, the out-of- equilibrium phonons, are detected using superconducting transition edge sensor, applied by photolithography to the crystal surfaces. This design allows a potential depth position sensitivity via measurements of the phonon pulse risetime giving the possibility of re-

jecting surface electron events that otherwise contaminate the signal region. It counts 15 Ge detectors (3.75 kg) with an effective exposure of 121.3 kg·d, averaged over recoil energies of 10-100 keV. A blind analysis resulted in zero observed events, yielding a 90% C.L. spin-independent upper limits in Ge of 6.6×10^{-8} pb (6.6×10^{-44} cm^2) for a WIMP mass of 60 GeV/c^2 [74]. The background due to surface events with bad charge collection for that experiment was estimated to be 0.6 ± 0.3 events.

As an alternative, ROSEBUD [75] and CRESST [67] have developed detectors in which, instead of ionization signal, scintillation light is measured in coincidence with heat, in particular using $CaWO_4$ crystal [67]. Here a silicon wafer with tungsten thermometer is used to detect the photons and a superconducting evaporated film used as the heat sensor. Although only 1% or less of the energy deposited is detected as photons this is much higher than feasible at room temperature and is sufficient to produce energy resolution comparable to NaI(Tl) crystal. Results so far have been obtained with two 300 g crystals at the Gran Sasso Underground Laboratory with a total exposure of about 20 kg·d revealing 16 events in the energy range 12-40 keV consistent with the expected neutron background given that the experiment is not screened by a neutron shield.

All these cryogenic experiments are now progressing toward significant upgrades for instance CDMS is proposing 25 kg and a possible move to the deeper SNOLAB site and CRESST is upgrading to allow 33 $CaWO_4$ detectors totaling 10 kg. However, as outlined in following paragraphs, it is likely that even greater target mass will be needed, possibly at the ton-scale or larger.

Liquid noble gases Liquid noble gas technology for WIMP searches has had a recent rapid growth. Most notable has been liquid xenon (LXe), by DAMA/Xe [76] and [77], but also recently liquid neon [78] and, in particular, liquid argon.

LXe has good intrinsic proprieties for WIMP detection including: high mass (Z=54 and A=131) yielding a good kinematic match to likely WIMP candidates; high scintillation and ionization efficiency ($\sim$46 photons/keV at 178 nm) and high radiopurity enhanced further by the availability of liquid gas purification techniques. The recoil discrimination important stuff is possible firstly by simple Pulse Shape Analysis (PSA) of the scintillation light: this is the basis for the single phase LXe XMASS experiment in Japan [79] and of ZEPLIN I in England [80]. As for the bolometer, more powerful discrimination is feasible in LXe by recording also the ionization produced and thus the ionization/scintillation ratio. This arises because for nuclear recoils the ionization signal is quenched significantly more than the primary

scintillation relative to electron recoils of the same energy.

Exciting progress has been made recently with the two phase LXe technology with both ZEPLIN III [81] (Boulby, UK) and XENON 10 [82] (LNGS, Italy) announcing new leading limits. ZEPLIN-III consists in 12 kg of two phase xenon; an analysis of 847 kg·d of data has excluded a WIMP nucleon elastic scattering spin-independent cross section above 7.7×10^{-8} pb at 55 GeV/c^2 WIMP mass with a 90% C.L.. The great XENON10 advantage is a very low energy threshold allowing to discriminate signal from background down to 4.5 keV nuclear recoil energy. A blind analysis of 58.6 kg·d of data excludes previously unexplored parameter space, setting a 90% C.L.. upper limit for the WIMP-nucleon spind-independent cross section of 8.8×10^{-8} pb for a WIMP mass of 100 GeV/c^2 and 4.5×10^{-8} pb for a WIMP mass of 30 GeV/c^2.

Tonne-scale idea WIMP experiments with target masses of kg-scale are reaching sensitivities probe starting to well into SUSY favored parameter space.

It is pretty certain, that favored spin-independent coupled dark matter does not exist with cross sections $>\sim2\times10^{-7}$ pb. Meanwhile, theoretical predictions for a neutralino-like WIMP reach cross section value smaller than 10^{-11} pb [83], [84]. Hence, next generation experiments must not only achieve further background suppression but also be capable of ton/multi-ton masses, simply to ensure a statistically observable signal rate. Secondly, for such large detectors it can be argued that though active gamma discrimination remains important, greater emphasis is needed on material purification, passive and active shielding of radioactive background and on searches for additional features in the data showing that remaining events, in particular, are not neutrons. In fact, if we assume that the experiment is situated deep enough to screen muon-induced neutrons, gamma and neutrons from U/Th chains in the environment and detector will dominate the background. For the the relevant energy range, less than 200 keV, such contamination produces typically 10^5-10^6 more gammas than neutron induced nuclear recoils [50]. The levels of detector sensitivity required for ton-scale experiments imply that gamma background must be comparable with or lower than the neutron rates. Neutron induced recoils, which cannot be distinguished from WIMP interactions, naturally will be the dominant background. Detector position sensitivity may help to discriminate such a neutron by allowing a multi scatter events rejection knowing that WIMP can only have a single interaction weakly interacting. However, we need a good passive neutron shielding and material purification plus WIMP signal identification. In addition, using at least two

targets/technologies with different A (atomic mass) and different systematics since the different behavior of WIMP and neutron scattering cross section as a function the atomic number mass, and/or studying correlation of events with Galactic motion by observation of annual modulation or a directional signal allowing a direct identification of events as of extra-terrestrial origin, should allow a discrimination of WIMP from neutron signals.

Scale-up to ton-scale is planned for instance, for cryogenic technologies, making best use of the high discrimination power demonstrated notably by CDMS, EDELWEISS and CRESST. Two particular efforts are foreseen: SuperCDMS [85] and EURECA (European Underground Rare Event search with Calorimeter Array) [86]. The former will use Ge and Si ionization/heat technology like CDMS in a staged expansion from 27 kg to 145 kg and eventually to 1100 kg by 2015 either at the US DUSEL, if built, or SNOLAB in Canada. EURECA represents a fusion of EDELWEISS, CRESST collaborations with further new group to develop a 100-1000 kg array using various targets, possibly both ionization/heat and scintillation/heat discrimination ideas. Both projects will need to develop improved detectors, in particular to allow better rejection of surface events, for instance through event position reconstruction or improved analysis, and to reduce unit costs.

1.4.2.2 Theoretical recoil spectrum

Since no WIMP signal is detected in current stage of direct dark matter searches (facing the fact of an unknown background), this kind of experiment can establish an upper limit on the scattering cross section of WIMP on nucleon as a function of WIMP mass. To succeed in this we need to know how our detectors respond to a hypothetical WIMP signal. Thus, the first step is to simulate a theoretical recoil spectrum of target nuclei in the crystal used by the experiment (Germanium for EDELWEISS) induced by elastic scattering of WIMPs with given M_W WIMP mass and scattering cross section on nucleon σ_{W-nucl}. Later, we will degrade this theoretical spectrum with experimental threshold and resolution to ensure a quite realistic spectrum.

Here, I want only to stress that the elastic scattering cross section depends on the type of interaction considered: either spin-independent or spin-dependent coupling between WIMPs and nucleons. For spin-independent interactions, we can express the cross section on the target atom (σ_{W-N}) as a function of the cross section on protons (σ_{W-p}) as:

$$\sigma^{SI}_{W-N} = \left(\frac{M_W + M_P}{M_W + M_{target}}\right)^{-2} \cdot \sigma^{SI}_{W-p} \cdot A^2 \tag{1.17}$$

It 's quite clear that depending on the square of the atomic mass of target

(A^2) the event rate will be higher in heavier targets.

For spin-dependent interactions, the cross section can be written:

$$\sigma^{SD}_{W-N} = \frac{32}{\pi} G_F^2 m_r^2 \frac{J+1}{J} (a_p \langle S_p \rangle + a_n \langle S_n \rangle)^2 \cdot \sigma^{SD}_{W-p} \tag{1.18}$$

where J is the total angular momentum of the nucleus, $\langle S_p \rangle$ ($\langle S_n \rangle$) is the expectation value of the spin contribution of the proton (neutron) group in the nucleus and a_p (a_n) the coupling constants between WIMPs and protons (neutrons).

The starting theoretical spectrum depends on WIMP scattering cross section off nuclei (σ_{W-nucl}), on WIMP mass (M_W) on target crystal mass (M_A) and on galactic halo parameters: dark matter local density ρ_0 and WIMP speed distribution in the halo ($f(v)$) and allows us to determine a theoretical event rate in the detector. All the calculations for the recoil spectrum refer to the Lewin-Smith work [50]. Each event rate of whatever incoming particle scattering on a target material can be write as follow:

$$dR = \frac{N_0}{A} \sigma v dn, \tag{1.19}$$

where N_0 is the Avogadro number (=6.02×10^{23} mol^{-1}), A the atomic mass of target nuclei, σ the particle-target material scattering cross section and dn the differential density per m^3 of incoming particle moving at v velocity. If we consider this particle being a WIMP, its differential density assumes the following form:

$$dn = \frac{n_0}{k} f(\overrightarrow{v}, \overrightarrow{v_E}) d^3 \overrightarrow{v}, \tag{1.20}$$

where n_0 is the WIMP density in the galactic halo, k is a normalization constant (see below), $\overrightarrow{v}$ its velocity in the galaxy rest frame and $\overrightarrow{v_E}$ the Earth velocity relative to Galaxy. $f(\overrightarrow{v}, \overrightarrow{v_E})$ is the particle's speed distribution in the halo supposed to be a Maxwellian one, Eq. (1.21) broken off at a velocity v_{esc} that represents the Galaxy's escape velocity.

$$f(\overrightarrow{v}, \overrightarrow{v_E}) = \exp^{-(\overrightarrow{v}+\overrightarrow{v_E})^2/v_0^2}. \tag{1.21}$$

This v_{esc}, identifying the needed speed to equal the kinetic energy of an object to the magnitude of its gravitational potential energy, corresponds thus to the maximal WIMP's velocity value: a particle with a velocity higher than v_{esc} will escape from the halo. The k variable is a normalization constant chosen in order that $n_0 = \int_0^{v_{esc}} dn$.

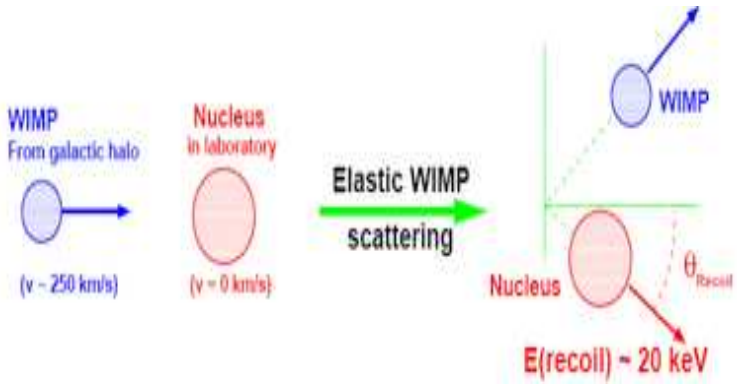

Figure 1.11: WIMP elastic scattering off nuclei scheme.

Since experiments measure a WIMP event energy spectrum, we need to express the differential event , Eq. (1.19), as a function of recoiling nuclei energy produced by WIMP scattering off as shown in Fig. 1.11

The WIMP kinetic energy is described by $E = \frac{1}{2}M_W v^2$ and the target nuclei recoil energy will be:

$$E_R = \frac{1}{2} rE(1 - \cos\theta) = rE\cos^2\theta_R; \tag{1.22}$$

where θ is WIMP scattering angle referring to the center of mass frame, θ_R is the recoiling nucleus angle, see Fig. 1.11 and r is four times the reduced mass divided by the sum of the masses defined as $\frac{M_W M_A}{(M_W+M_A)^2}$. The recoil energy for the WIMP will be maximal for target nuclei mass (M_A) equal to WIMP mass (M_W). Assuming an isotropic distribution of scattering angles in the center of mass frame, that it means that recoils are equally distributed as a function of recoil energy in a range $0<E_R<rE$, we can calculate the differential event rate in recoil energy as follow:

$$\begin{aligned} \frac{dR}{dE_R} &= \int_{E_{min}}^{E_{max}} \frac{1}{rE} dR(E) \\ &= \frac{1}{E_0 r} \int_{v_{min}}^{v_{max}} \frac{v_0^2}{v^2} dR(v) \end{aligned} \tag{1.23}$$

where $v_{max}=v_{esc} \pm v_E$. E_{min} bound is defined as the smallest WIMP energy able to give a recoil energy E_R, referred so to have a θ_R equal to one in the Eq. (1.22); E_0 is the WIMP kinetic energy relative to a velocity v_0 (see Eq. (1.21)) and so v_{min} bound represents velocity of a WIMP having E_{min} as energy.

Starting from the Eq. (1.23) and filling all the ingredients needed we obtain

$$\frac{dR(v_E, v_{esc})}{dE_R} = \frac{R_0}{E_0 r}\frac{k_0}{k}\frac{1}{2\pi v_0^2}\int_{v_{min}}^{v_{max}} \frac{1}{v} f(\overrightarrow{v}, \overrightarrow{v_E} d^3 v \tag{1.24}$$

where R_0 event rate expressed in evt/kg/d is here defined by
$R_0 = \frac{540}{AM_W}\frac{\sigma_{W-A}}{1pb}\frac{\rho_0}{0.4GeV/c^2/cm^3}\frac{v_0}{230km/s}$ [50]
that allows the event rate and scattering cross section normalization (see below).

This is the WIMP off nuclei scattering rate as a function of the recoil energy, which is normally called theoretical recoiling WIMP spectrum. The most important feature to point out is its exponential shape as shown in Fig. 1.12. But this is not the final theoretical spectrum to compare with the experimental one, in fact we have to apply three corrections due to Earth motion effect [51], nuclei size introducing a form factor ($F^2(E_R)$) which depends on the scattering cross section type (spin-independent or spin-dependent) [87] and a scale factor S that allows to express σ_{W-A} as a function of σ_{W-nucl} again depending on the scattering cross section type (spin-independent or spin-dependent) [88].

Taking into account these corrections we result in the final theoretical WIMP recoil spectrum which gives a relation between the WIMP scattering off an A atomic mass nucleus with a given non zero transferred momentum (A, q^2) and the interaction of a WIMP with a nucleon with a zero transferred momentum:

$$\frac{dR(v_E, v_{esc})}{dE_R}\,|_{(A,q^2)} = \frac{dR(v_E, v_{esc})}{dE_R}\,|_{(n,0)} \times F^2(E_R) \times S \tag{1.25}$$

Thus, we are able to draw this WIMP recoil spectrum for a Germanium nucleus, target nuclei used by EDELWEISS. First we have to set the value of some parameters. Some simplifying assumptions on the dark matter profile are essential: in particular an isothermal profile is often assumed, a local density of ρ_0=0.3 GeV/c^2/cm^3 and a Maxwell-Boltzmann velocity distribution with a characteristic velocity of v_0=270 km/s. The further constants are fixed at the usual value of v_{sun}=235 km/s and v_{esc}=650 km/s. Regarding to the corrections to apply, the form factor is the same in [87] and we just average the annual modulation, resulting in $v_E = v_{sun}$. The Fig. 1.12 shows the evolution of this peculiar exponential shape for three different WIMP mass for a reference scattering cross section value of 7×10^{-6} pb.

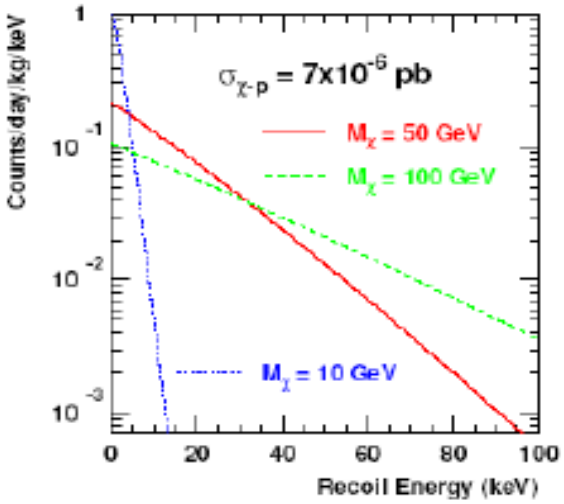

Figure 1.12: Theoretical WIMP spectrum: spin independent cross section on Ge target nuclei for three different WIMP mass to evaluate the evolution and for a reference value of cross section of about σ_{W-p}=7×10^{-6} pb.

1.4.2.3 Exclusion plot

So far, direct dark matter experiments are reporting upper limits on nucleon-WIMP cross sections since the signal they try to detect is nonexistent or below their sensitivity. The problems are that the backgrounds are poorly understood and the WIMP cross section is not known. However, there are less uncertainties concerning the predicted shape of the distribution in E_{recoil} for a given WIMP mass. The simplest way to dealing with such a situation is to select an interval in E_{recoil} and take as the upper limit the largest cross section, σ_{exp}, that would have a significant probability, for instance 10%, of giving as few events as were observed, assuming that they are all WIMP candidate signal. This approach is very sensitive to the choice of the energy range. It is important that the chosen recoil energy interval is selected independently from the observed data.

The limit σ_{exp} for a given WIMP mass is calculated the following way.

We integrate the theoretical spectrum calculated to obtain the WIMP event number expected (μ_σ) for a given WIMP mass and scattering cross section σ. The limit on σ_{exp} is given by:

$$\sigma_{exp} > \frac{\sigma \times \mu_{exp}}{\mu_\sigma} \tag{1.26}$$

where μ_{exp} is the upper limit on the number of events that the experiment should observe if the cross-section is σ_{exp}. According to Poisson distribution, if we observe no events in the experiment, we obtain μ_{exp}= 2.3 at a 90%C.L. and μ_{exp}=3 at a 95%C.L. [89].

The poorly known background is a particular concern as it cannot be subtracted reliably. We have two possibilities. The first is to use Poisson distribution, considering all events observed as WIMP candidates. The other is to use the methods, named "maximum gap" and "optimum interval", developed by S.Yellin within the CDMS collaboration [90].

As well as Poisson, all observed events are regarded as WIMP candidates. But, these methods give prescriptions on how to optimize the choice of recoil energy interval to obtain the most strict limit. This choice is based on comparison between WIMP theoretical recoil spectra and observed data. The predicted μ_{exp} takes into account the bias induced by using data to select energy interval. More details can be found in [90] and in [91].

The limits $\sigma_{exp}(\mathrm{M}_W)$ can be compared to some predictions which have been made on this two parameters (cross section and mass) depending on the dark matter candidate predicted by what kind of theoretical model has been chosen (for instance we consider as the most attractive candidate the Neutralino of supersymmetric models such as the minimal supersymmetric extension of Standard Model (MSSM)).

The WIMP mass is currently constrained between a lower limit given by the LEP accelerator results of about 40 GeV [92] and an upper one of $\sim$ TeV provided by SUSY predictions [33]. The cross section, must be of the same order of magnitude of weak interactions so we can put an upper limit of about 10^{-5} pb [93], already overtaken by current direct dark matter searches.

Chapter 2

The EDELWEISS Experiment

In this chapter I will start describing the possible background sources overwhelming the EDELWEISS experiment and the consequent experimental apparatus needed in order to screen detectors. Afterwards I will focus on the Ge-NTD type detectors, and on its measurement channels (ionization and heat signals).

The EDELWEISS experiment (Expérience pour Détecter les WIMPs en Site Souterrain), situated in the Modane Underground Laboratory (LSM) in the Fréjus highway tunnel, is dedicated to the direct detection of WIMPs. As already said, the direct detection principle consists in the measurement of the energy released by nuclear recoils produced in an ordinary matter target by the elastic collision of a WIMP from the Galactic halo.

The main challenge is the expected extremely low event rate ($<$1 evt/kg/year) due to the very small interaction cross section of WIMP with ordinary matter. An other constraint is the relatively small deposited energy ($<$100 keV).

In order to measure low energy recoils, EDELWEISS employs cryogenic detectors (high purity Ge crystal) working at temperature of about 20 mK, with simultaneous measurements of phonon and ionization signal. The ionization signal, corresponding to the collection on electrodes of electron-hole pairs created by the energy loss process, depends on the particle type whereas the heat signal reflects the total energy deposit.

This simultaneous measurements of two signals allows an event by event discrimination between the electronic recoils, tracers of background (induced by photons and electrons) and the nuclear one originated by neutrons and WIMPs.

2.1 Expected Background

In low background experiments of rare events, such as the EDELWEISS experiment, several factors in the experimental backgrounds can obscure the signal counts of interest. These experiment backgrounds are environmental radioactivity, intrinsic contamination of detectors and shielding material, airborne radioactivity (Radon) and cosmic rays induced particles.

EDELWEISS aims to reach a sensitivity in the WIMP-nucleus interaction detection better than 0.003 counts/kg·d for recoil energy above 10 keV. To reach this goal, background rejection and discrimination are necessary. EDELWEISS background includes gammas, betas and neutrons from cosmic rays and natural radioactivities. Thanks to simultaneous measurements of ionization and heat signals EDELWEISS detectors can discriminate gammas from WIMPs at high efficiency, because WIMPs interact with nuclei; gammas with electrons.

2.1.1 Interactions inside detectors

It has been said that we have to distinguish electronic recoils, tracers of background induced by photons and electrons from the nuclear recoil induced by WIMPs and neutrons. Afterwards, succeeding in the discrimination between a WIMP and a neutron signals will complete the device. Let's first describe where these particle could come from and how they interact with detectors.

Photons Gamma rays result from natural radioactivity, radioactive contaminants in the detector and shielding material and those arise from the cosmic ray muon flux observed at the experimental site. Radioactive nuclides from the ^{238}U and ^{232}Th chains and the presence of ^{40}K in the rock and the surrounding materials give rise to photons. Radioactive nuclides are also produced from the interactions of cosmic-ray muons with materials of the detectors and shielding, when they were outside the underground laboratory. Photons can also arise as a consequence of contaminants in detectors and shield.

Photons can interact with ordinary matter through these four processes:

The **photoelectric** interaction, where a gamma ray is absorbed by an electron bound to an atom. The electron is stripped from the atom, carrying with it the momentum of the gamma ray, and the energy of the gamma ray minus the electron's binding energy. This process has of between 0.6 cm and 5 cm on attenuation lengths in germanium

(depending on the photon energy, see Fig. 2.1). It is the dominant process for energy below 150 keV .

The **Compton** interaction, where a gamma ray scatters from an electron. The gamma ray transfers a fraction of its original energy and momentum to the electron (recoil electron). The scattered gamma ray has a lower energy and a different direction from the original gamma ray, in what is called Compton scattering . It represents the dominant process in a Germanium target (see Fig. 2.1) for energies between 150 keV and 8 MeV. Even these photons have between 0.6 and 5 cm attenuation lengths.

The **pair production** interaction, where a gamma ray's energy is converted into the creation of an electron-positron pair. A small fraction of the gamma ray momentum must be transferred to an atom to initiate the interaction. The remainder of the momentum is carried away by the electron-positron pair. The pair-production process requires a minimum gamma ray energy of 1.022 MeV before it can occur. The positron will eventually annihilate with another electron (10-100 ps time scale below 10 MeV), creating a pair of oppositely directed 0.511 MeV gamma rays. Given the energy range at which this process is significant (E>3 MeV for germanium, see Fig. 2.1) it can be neglected when assuming γ-rays from background radioactivity ending at 2.3 MeV.

Coherent scattering, where a gamma ray scatters from an electron bound to an atom imparting no significant energy. The gamma ray changes direction, leaving no detectable energy loss at the interaction site. Coherent scattering is generally significant at lower energies (below about 100 keV). It is most easily observed lower-Z materials such as silicon, where the competing photo-electric process has a lower cross section.

Moreover, the energy transport process is not over until the recoil electrons and/or atoms with electron vacancies loose their energy and return to the ground state. Recoil electrons may interact with matter producing bremsstrahlung radiation (more gamma rays), and atoms with atomic vacancies may emit an Auger electron or fluorescence X-ray.

Alphas and betas Alphas and betas arise from radio-contaminants on the surface of detectors, presence of radioactive nuclides, such as radon, in detec-

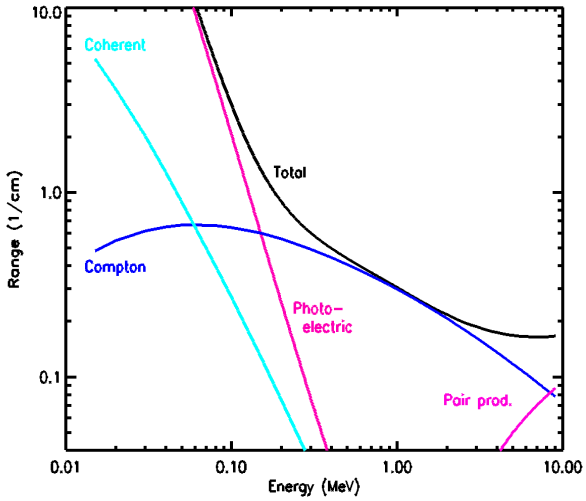

Figure 2.1: Gamma-ray cross-sections for interactions in germanium crystal.

tors and shielding materials before entering in the underground laboratory clean room.

Interactions of electrons and fast light ions such as an alpha particles, occur with electrons of atom's outer shells.

Since alpha particles are heavier than electrons, the alpha energy loss is very small and its path in the nucleus is nearby straight. By way of example in a germanium crystal an alpha particle with 5 MeV mass will be stopped after a length of about 20 μm. For an electron the attenuation length varies as a function of energy.

Of special interest is the electrons that scatter near the detectors surface, since the small attenuation length: the so called surface events.

Neutrons In the previous chapter it has been shown that neutrons are the most dangerous source of background because they can mimic a WIMP signal. The EDELWEISSS experiment is protected by a polyethylene shielding in order to stop low energy neutrons having energies between 1 and 10 MeV. Actually a neutron having 0.5 MeV energy and a WIMP of 100 GeV mass and an energy of 30 keV give recoil energies of the same order of magnitude (about 30 keV) [94].

Therefore we must to close attention to high energy neutrons (several GeV) that can cross the polyethylene shielding and produce lower energy neutrons in the lead shielding and other materials. In such a deep under-

ground laboratory the neutron background is induced by [95]:

natural radioactivity due to spontaneous fission of uranium and thorium. The isotope ^{238}U is the main source of fission in the rock producing neutrons having an average energy of about 2 MeV;

an equally important source of neutron are reactions of type **(α, n)** due to the alpha particles emitted by uranium, thorium and their daughters interacting with the rocks. This kind of neutrons have an averaged energy of about 3.5 MeV;

the **muons** interacting with materials around the experiment. By weak interactions a muon can couple to a proton in a nucleus following this process $\mu^- + p \rightarrow n + \nu_\mu$. The resulting neutron has an energy between 6 MeV and few dozens of MeV. Muons can also produce higher energy neutrons by inelastic scattering: $\mu^- + (Z, A) \rightarrow \mu^{'} + (Z.A^{'}) + xn + ...$ These fast neutrons produced with an energy much higher than 10 MeV cross large amount of shielding material and interact with detectors.

2.1.2 Starting point: EDELWEISS-I

The results from this work will be compared extensively with those of the first phase of EDELWEISS experiment, stopped in March 2004. It consisted of 1 kg total mass of Germanium in three detectors operating at 17 mK.

After a fiducial exposure of 62 kg·d with a threshold energy of 15 keV, 40 events have been recorded in the nuclear recoil band. Most of these were at low energy and only three have been observed above 30 keV. The shape of simulated spectra of WIMPs having masses between 20 and 100 GeV cannot explain the shape of recorded spectra in the nuclear recoil band by a single WIMP mass, suggesting therefore the presence of a background. It provided sensitivity of $1.5\times\ 10^{-6}$ pb for the scattering cross section of a WIMP with a mass of 80 GeV [4].

A more careful investigation of events outside the WIMPs search selection revealed the presence of backgrounds due to neutrons and surface events [96].

Surface events: In a Ge detector, when the interaction of a particle takes place near the electrode, the charge collection can be incomplete, resulting in ionization signals smaller than the expected ones [97]. The consequent event appearing in the nuclear recoil band can mimic a WIMP event. In the detectors covered by this work, this problem was partially controlled by depositing a 60 nm Ge or Si amorphous layer on the crystal surface which diminishes the number of events with deficient charge collection.

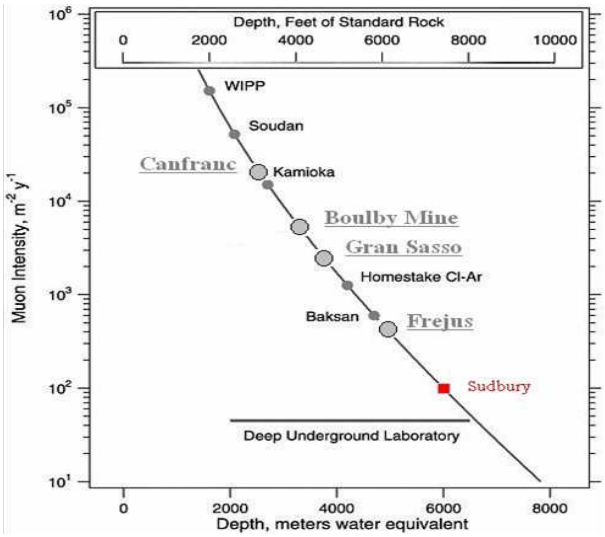

Figure 2.2: Muon intensity in $m^{-2} \cdot y^{-1}$ as a function of depth (meters equivalent equivalent).

An active rejection of surface events can be achieved by identification of these events using interdigitized electrodes. It is essentially a variation of the coplanar grid technique [98] in which interleaved strips are substituted for the classical disk-shaped collection electrodes. The depth of an event relative to the surfaces can be inferred from a comparison of the ionization signals on the different strips [99].

Neutrons: In data recorded during the first stage of EDELWEISS, a coincidence between two nuclear recoils in two separate detectors was observed. It was interpreted as a sign that the 30 cm paraffin shield of EDELWEISS-I experiment was not sufficient to suppress the entire neutron flux. Monte Carlo simulations, including the imperfections of the shield, tended to confirm this interpretation.

2.2 The EDELWESS-II setup

The first protection against background is provided by the choice of the location (LSM), with an overburden of about 1700 m of rock, equivalent to 4800 m of water, reducing the cosmic muon flux down to 4.5 μ/m^2/day, that is about 10^6 times less than at the surface, see Fig. 2.2.

To reduce environmental background, all materials used in the vicinity of the detectors have been tested for their radiopurity with a dedicated HPGe

detectors. The material were selected for giving an estimated counting rate of less than 0.001 counts/kg·d in the detectors. A class 10^4 clean room surrounds the upper level of the setup shown in Fig. 2.3. A class 100 laminar flow with deradonised air ($\leq$ 0.1Bq/m^3) is used when mounting the detectors in the cryostat in order to reduce the deposition of contamination on the surfaces.

The **gamma background** is screened by a 20 cm thick lead shielding around the cryostat.

In the experimental volume of the cryostat the **neutron background** is attenuated by three orders of magnitude thanks to a 50 cm thick polyethylene shielding. In addition, an active muon veto with a coverage of more that 98% tags the muons interacting in the lead shield and producing neutrons (muon induced internal neutrons) [94].

The residual neutron background comes from high energy neutrons produced by muons that are not tagged by the veto system and by neutrons from ^{238}U fission in the lead shielding. This muon-induced high energy neutrons will eventually set a limit for the EDELWEISS experiment. But this can be lowered significantly with signature of neutron, such as multiple nuclear recoil event rate (WIMPs only scatter off nuclei in one detector, but neutrons can scatter off nuclei in several detectors) as well as the energy spectrum of neutrons from Monte Carlo simulations.

By Monte Carlo simulations the nuclear recoil rate above 10 keV in the detectors is estimated to be $<10^{-3}$ evt/kg/d [100]. That corresponds to a WIMP-nucleon cross-section sensitivity of 10^{-8} pb for a WIMP mass of $\sim$100 GeV/c^2, improving the sensitivity of a factor 100 compared to EDELWEISS-I, and competitive with CDMS-II [74].

The dilution cryostat is of a reversed design, with the experimental chamber on the top of the structure. Its large volume (50 l) can host up to 40 kg of Ge detectors arranged in an hexagonal compact way, that will allow increasing the probability of neutron coincidences.

2.3 Detectors

Interacting with matter, a particle loses all or only a part of its energy in the target. The goal is to measure this energy deposit and, simultaneously, an ionization signal if the electrons are emitted by the atomic system or a scintillation signal corresponding to electrons de-excitation in light, depending on detector material . It must be pointed out that only a fraction of the energy deposit is converted in such kind of signals. In crystal most of the energy deposit will turn into heat by phonons, propagating from the interaction point of incoming particle in the target where they are generated. The

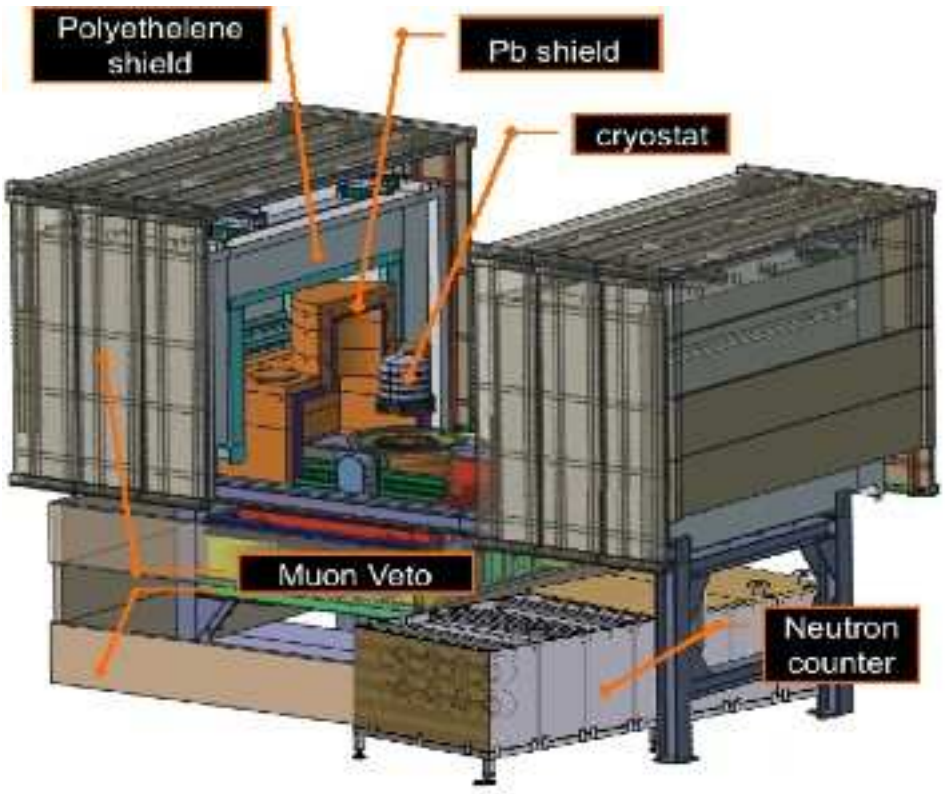

Figure 2.3: General scheme of the EDELWEISS-II experiment. From Outside to inside: The outer shell is the muon veto system, followed by the polyethylene shield and the inner lead shielding. The upper part can be open to have access to the cryostat which houses the bolometers.

ionization energy is also converted to heat when charges recombine or are collected.

The EDELWEISS detectors rely on the detection of ionization and heat. This simultaneous measurements enable the rejection of radioactivity background from gammas particles. The detectors are the so called "double detection bolometers". They combine bolometer technology for heat measurement and the semiconductor technique for ionization channel.

Heat Bolometers benefit from good baseline resolutions and very low energy thresholds. In addition it allows the full detection of low-energy ionizing particles as it is fully efficient even for surface interactions. On the other hand the slow time constants of heat signals and the cryogenic temperatures are constraints. These extreme temperatures are needed in order to maximize the temperature increase induced by the scattering particle, as the specific heat capacity of a crystal is proportional to the third power of the temperature.

A bolometer is made up of two elements: the absorber where the interaction takes place and a thermal sensor measuring the temperature increase. The role of absorber is to thermalize the energy deposit due to scattering of incoming particle on target material as soon as possible. As said before, its specific heat capacity must be kept to the minimum using cryogenic temperatures of order of mK. In addition the absorber is better to be a pure dielectric and diamagnetic crystal so that only the lattice crystal (atomic vibrations) contributes to the specific heat capacity. For instance metals are not good bolometer absorbers because in addition to the phonons contribution the nearly-free electron gas, characterizing conductors, supplies a not negligible share to the specific heat capacity at cryogenic temperature. Here, since we want to measure simultaneously heat and ionization signals the absorber is a semi-conductor (germanium).

The thermal sensor has to convert the absorber temperature increase in a measurable electric signal. The thermal measurement used by EDELWEISS is based on the variation of a resistance R of a small $\sim$ mm^3 germanium crystal with a high level of impurities resulting by an exposition to a controlled thermal neutron flux (Neutron Transmutation Doped germanium; NTD) as a function of temperature.

For low temperature, relation between R and T for these sensors can be written [101] as $R(T) = R_0 \exp \sqrt{\frac{T_0}{T}}$ where T_0 is sensor characteristic temperature. T_0 and R_0 values depend on thermometer type, typically few ohms for the resistance and few Kelvin for temperature. Here NTD are selcted to have resistance of the order of magnitude of 1MΩ at a working temperature of T=20 mK. A constant electric current i is circulated in the sensor. The

resistance variation as a function of temperature $R(T)$ induces a potential variation following $\Delta V(T) = i \cdot \Delta R(T)$, proportional to the incoming particle energy deposit. Typical values of of i are a few nA.

In order to be sensitive to the fully thermalized phonons the risetime of the sensor is slow ($\sim$ 1 to 10 ms). This ensure a very precise energy measurements independent of the location of the interaction. There is however no sensitivity to a thermal components, that used in the CDMS [72] and NbSi detectors [102].

Ionization The semiconductor principe is the same of an ionization chamber: the measurement of ionizing radiation corresponding to the collection on electrodes of electron-hole pairs created by the energy loss process. In a semiconductor energy levels are forming two bands separated by a gap. The lower, almost fully occupied band in an insulator or semiconductor, is called the valence band by analogy with the valence electrons of individual atoms. The upper, almost unoccupied band is called the conduction band because only when electrons are excited to the conduction band can flow current in these materials. Between the two bands the band gap is of the order of 1 eV (0.7 eV in germanium). At high temperature the thermal energy excites electrons in valence band to the conduction band leaving behind electron holes that can flow as current exactly like a physical positive charged particles. Two process are involved: carrier generation describes mechanism by which electrons gain energy and move from the valence band to the conduction band, producing two mobile carriers; while recombination describes processes by which a conduction band electron loses energy and re-occupies the energy state of an electron hole in the valence band.

At very low temperature, the conduction band is essentially empty, unless carriers are generated by the interaction of high-energy electrons. these carriers recombine locally, unless they are separated by an external electric field.

The ionization signal is obtained by the collection of these electron-holes pairs on electrodes on the surface of the detector, polarized to provide the electric field.

The charge collection is incomplete when their migration is interrupted. Three causes have been pointed out:

> **Crystal impurity**: charges flowing to the electrodes could be trapped by crystal impurity resulting in the formation of space charges (continuum of charge distributed over a region of space). In order to reduce this effect, data acquisition is stopped every day for about one hour

to perform detectors regeneration [103]. Electrodes are short-circuited and only the space-charge induced field survives.Two strong ^{60}Co γ-rays sources are used to generate a large flux of charge, which will neutralize the previously induced space-charge. During the data taking the applied difference of potential on electrodes V is chosen large enough so that losses due to trapping are too small to be observable.

Surface events: since electrons and alphas particles, for energy of about few tens keV, have an averaged attenuation length of some μm in germanium crystal, their interactions occur in the vicinity of detector surface. By diffusion the charges created in these interaction can be collected on the wrong electrodes producing an ionization signal about half smaller than the real deposited one. As mentioned in subsection 2.1.2, the detector are covered by a germanium or silicium amorphous layer deposited between electrode and crystal, in order to provide an energy barrier that prevents the random diffusion of charge into electrode.

Free germanium surfaces: there are some gaps between the electrodes and some electric field lines end on this area. The charges collected on these lines accumulate on the surface of the detector. The top electrode for the charge collection is divided into a central part and a guard ring; in addition beveled edges provide a more homogeneous electric field in the volume beneath central part of top electrode. The sensitive areas are between the guard and central electrodes and the guard and the reference electrodes, see Fig. 2.5. All events associated with charge deposited on the naked germanium surface will tend to deposit also some charge on the guard electrodes. Therefore, events with a charge signal on the guard electrode are systematically rejected.

2.3.1 Ge-NTD

The detectors used within the EDELWEISS experiment are made of germanium absorber (target for the incident particles) equipped with a thermal sensor and with metallic electrodes for charge collection [97] and [104]. Scheme and picture are shown in Fig. 2.4. The absorber is a $\sim$320 g high purity Ge cylindrical crystal ($\sim$70 mm diameter and 20 mm thickness). Their edges have been beveled at an angle of 45° in order to increase the volume where electric field lines end up on the central electrode.

The electrodes or ionization measurement are made of 100 nm Al layers sputtered on the surfaces after etching. The top electrodes is divided in a

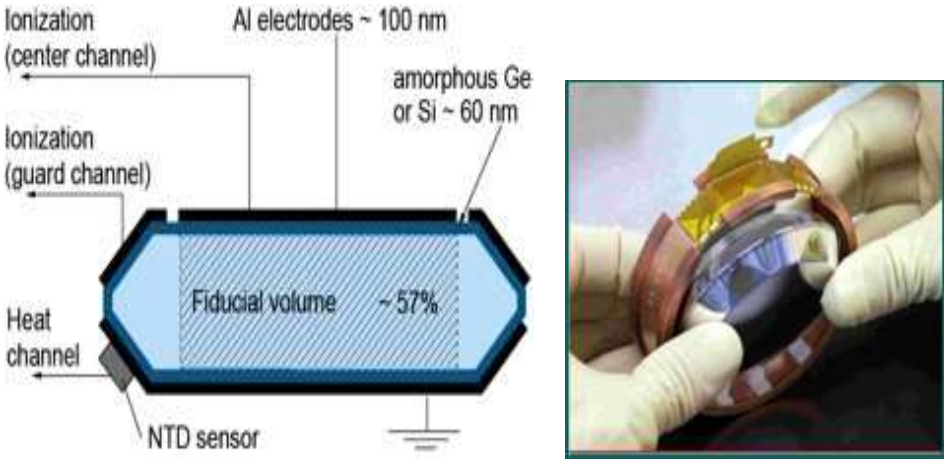

Figure 2.4: *Left side*: bolometer scheme. *Right side*: bolometer picture

central part and a guard ring electrically decoupled for radial localization of charge deposition; the bottom electrode is the common reference. The applied collection voltage V_{bias} is -7V. According to whether the 60 nm hydrogenated amorphous layer is made of germanium or silicon the detector is named GGA or GSA respectively.

The thermal NTD sensor is directly glued on a sputtered gold pad near the edge of the bottom Al electrode (Fig. 2.4).

2.3.1.1 Ionization measurement

The amplitude of ionization signal A_I is proportional to the number of electrons-holes pairs collected, N. For electron recoils

$$A_{I,\gamma} \propto N_\gamma = \frac{E_R}{\epsilon_\gamma} \tag{2.1}$$

where E_R is electron recoil energy and ϵ_γ is the average energy needed to create an electron-hole pair. At cryogenic working temperature ϵ_γ is about 3.0±0.1 eV in agreement with the measurement of [105]. It is the value used by the EDELWEISS and CDMS experiments. The amplitude A_I is calibrated using ^{133}Ba gamma-ray sources to provide E_I in energy in units of keV_{ee} (electron-equivalent), using the photoelectric peaks at 356 keV and 383.9 keV. This procedure permits to obtain the normalized ionization energy E_I for every incoming particle that it is written as $E_I \equiv \epsilon_\gamma \cdot N_I$: the energy necessary to produce N_I electron-hole pairs.

Figure 2.5: Cryostat pictures showing how bolometers are housed in tower.

For nuclear recoils ϵ_n is approximately 12 eV and varies as a function of energy. It means that for a given energy deposit a nuclear recoil generates 4 times less electron-hole pairs than an electron recoil does. This difference is identified by the so called quenching factor for the ionization signal of nuclear recoils defined as $Q_n = \epsilon_\gamma/\epsilon_n$

$$A_{I,n} \propto N_n = \frac{E_R}{\epsilon_n} = Q_n \frac{E_R}{\epsilon_\gamma} \tag{2.2}$$

By convention for electronic recoils we ask that the recoil energy is equal to ionization energy $E_R = E_I$ that it means that $N_I = E_R/\epsilon_\gamma$. Thus, rewriting Eq. (2.1) and Eq. (2.2) we are able to find out the ionization energy for electronic and nuclear recoil such as:

$$E_{I,\gamma} = Q_\gamma \cdot E_R; \tag{2.3}$$

$$E_{I,n} = Q_n \cdot E_R \tag{2.4}$$

with Q_γ=1, by construction.

2.3.1.2 Heat measurement

Due to the bias voltage needed for the ionization measurement we have to take into account the Joule heating due to the drift of the charge carriers (Neganov-Luke effect [106]). The energy generated by Neganov-Luke effect is proportional to the charges times the applied voltage
$E_{N-L} = N_I V = \frac{E_R}{\epsilon} e\, V$,
where e is the charge of proton and V is the absolute value of the applied potential (a low bias voltage is required to limit the Negavov-Luke effect). In analogy with the ionization channel, the heat energy, E_H for every incoming particle is normalized in units of keV$_{ee}$;

$$E_H \equiv \frac{E}{1 + \frac{V}{\epsilon_\gamma}} \tag{2.5}$$

with E the total measured energy: $E = E_\gamma + E_{N-L}$.

The total measured energy for the heat channel has thus two contributions: the recoil energy E_R (eventually lowered by a heat quenching factor Q'_n) and the Neganov-Luke effect E_{N-L} resulting in the following formulae:

$$E_\gamma = E_R + \frac{E_R}{\epsilon_\gamma}\, V = E_R(1 + \frac{V}{\epsilon_\gamma}) \tag{2.6}$$

for electronic recoils and:

$$E_n = Q'_n E_R + \frac{E_R}{\epsilon_n}\, V = E_R(Q'_n + \frac{Q_n V}{\epsilon_\gamma}) \tag{2.7}$$

for nuclear recoils. In conclusion, putting all these inputs together we obtain the heat energy for electron ($E_{H,\gamma}$) and nuclear ($E_{H,n}$) recoils as follow:

$$E_{H,\gamma} = E_R \qquad (as\ assumption); \tag{2.8}$$

$$E_{H,n} = E_R \frac{Q'_n + \frac{Q_n V}{\epsilon_\gamma}}{1 + \frac{V}{\epsilon_\gamma}}. \tag{2.9}$$

Physics need: (Q, E$_r$) plane

To sum up what we have done till now, here it is normalized ionization and heat energy

$$E_I = Q \cdot E_R \tag{2.10}$$

$$E_H = E_R \frac{Q' + \frac{QV}{\epsilon_\gamma}}{1 + \frac{V}{\epsilon_\gamma}} \tag{2.11}$$

where (Q, Q') are equal to (Q_n, Q'_n) and to (1,1) for nuclear and electronic recoils, respectively.

It is not possible to determine the three quantities E_R, Q and Q' from these two equations. Careful investigation reveals that Q' is close to one for germanium crystal [107], and we adopt the value Q'=1 as CDMS. With Q' fixed at one, the variable Q and E_R can be expressed as a function of (E_I, E_H):

$$E_R = (1 + \frac{V}{\epsilon_\gamma})E_H - \frac{V}{\epsilon_\gamma}E_I \tag{2.12}$$

$$Q = \frac{E_I}{E_R}. \tag{2.13}$$

With regard to the ionization quenching factor, noticing that it is a function of recoil energy and of target material, within the EDELWEISS collaboration a survey based on calibration of germanium nuclear recoils has been carried out [108] resulting in $Q_n = 0.16 \cdot E_R^{0.18}$. Nuclear events are thus identified by this experimental value of Q equal to Q_n and different from one, within uncertainties.

A problem arises for those events where the charge collection is incomplete such as surface events. If only half the charges are collected the experimental Q is 1/2. By construction E_R will still equal to the deposited energy but the heat signal will be affected because of the reduced contribution to Negavov-Luke effect. It means that these events leak from the electron recoils band down to the nuclear recoils band, as the fraction of collected charge decreases.

2.4 Electronics and data acquisition

The three physical quantities measured for each detector are: two ionization signal (*center* coming from charge collection on central top electrode and *guard* from charge collection on the guard ring) and heat signal (from the NTD thermal sensor).

The main signal specifications are related to their risetimes and decay times. For the heat signal the risetime is of the order of 1-10 ms and the decay time in the 50-500 ms range. The ionization is intrinsically faster: risetime and decay time are $\sim$100 ns.

The electronics have to be designed making a compromise between putting radioactive components as far as possible (in addition, some components do not work at cryogenics temperatures) and putting electronics components as close as possible to reduce noise due to stray capacitances and microphonics.

The main goal is to obtain a ∼keV FWHM baseline resolutions both for heat and ionization signals.

The acquisition system has to manage the data, digitizing them in a continuous flow for constant baseline monitoring. Synchronization and time information between channels are performed using a common clock and a common control of sampling frequency, in order to easily identify and subtract common noise patterns due to electronics.

The signals are amplified and digitized at a rate of 100 kHz as soon as they exit the cryostat in low radioactive electronic modules plugged directly to the cryostat.

The trigger is defined numerically by requesting that the absolute value of any channel exceeds a given threshold. The trigger can be based on ionization or heat channels, after applying numerical filters. For the 8^{th} cool down of EDELWEISS-II, the trigger is based on heat channel resulting in a better sensitivity at low energy in comparison to ionization trigger [109]. In fact, for low values of applied voltage, the ionization signal for electronic and nuclear recoils differs by about a factor three while the heat amplitude rests constant for the two recoils.

Phonon trigger configuration requires that one of heat channel exceeds a predefined level. When a trigger is found the relevant ionization information lies in the past since its rise-time about 1000 times faster than ionization one.

For this reason, the data stored on disk for each trigger are the heat channels in a ±256 ms window around the trigger time, and a (-30.72 ms, +10.24 ms) window for the ionization channel.

Some features have to be taken into account: the presence of a dead time of 250 ms which represents the time after each event during which the system is not able to record another event, and a signal saturation (about 2.5 MeV for ionization signal and 3 MeV for heat channel) that is must be taken into account in a high energy analysis.

Chapter 3

Data Analysis

In this chapter the different steps in the data analysis chain are detailed. I will start describing the offline re-processing of the data stored during the acquisition, stressing out the method to obtain stable (as reference to baseline resolution) and good (low energy threshold) data. The goals of this analysis are a better understanding of radioactive background permeating the EDELWEISS experiment and to obtain nuclear recoil events associable to WIMP candidates.

The energy range for these recoils is constrained by the results obtained during EDELWEISS-I and the commissioning runs conclusions in agreement with a remnant ^{210}Pb contamination. This produces a β contamination of the nuclear recoil band at low recoil energies (E_R <30 keV) due to a surface events as was recorded in the previous stage of EDELWEISS (see Subsection 2.1.2). For this reason, the lower recoil energy bound has been set at 30 keV.

Thus, the "WIMP-limit analysis" range starts at 30 keV recoil energy requesting also the efficiency at this energy to be close to 90% and excluding the region where the γ-ray rejection is worse than 99.9%. For this latter, we can take into account for analysis only detectors having the intersection of their γ band at 99.9% rejection and their neutron band at 90% efficiency, called *magic point*, lower than 30 keV.

The analysis steps are the following. The first step is to determine the amplitude of the different measured channels, continuing with their energy calibration. Afterwards, resolutions measurements are an essential task: we remove noisy periods by monitoring the baseline resolutions. In addition, this values are required to determine the gamma band (electronic recoils zone for 99.9% efficiency) and the neutron-WIMP band (nuclear recoils zone for 90% efficiency). Energy threshold calculations complete the definition of the recoil zones. With these prescriptions on hand, we can describe the WIMP candidate selection.

3.1 Signal Processing

Recorded events are re-processed offline. In the offline analysis the data are filtered with digital filters and then adjusted with templates of ionization and heat signals taking into account the simultaneity of center, guard and heat signals.

There is one template for each measurement channel and for each detector. Templates are built with a sample of selected 356 keV events from calibration runs with the ^{133}Ba source. It has been verified that templates are not time dependent. Figure 3.1 shows examples of filtered ionization and heat pulses (full lines) with reference template fits (dashed lines). The goodness of fit is defined by the value of a pseudo-χ^2 which does not depend on pulse amplitude. This is defined as $\chi^2 = \sum_{i=1}^{N}(data_i - fit_i)^2$, where N is the number of fitted samples. This pseudo-χ^2 is in units of (ADU)^2 [1] and is not normalized to the errors on the data, since the noise is not random. This χ^2 is useful to compare the data from events to events. A larger χ^2 indicates a poor model fit.

The piled-up pulses, practically negligible in low-background runs are more dangerous in calibration runs because of a higher event rate due to the source activity. The χ^2 values are used to reject pile-up events in calibration runs only.

In the phonon trigger data, some events are due to internal radioactivity of the NTD sensor. For these events the deposited energy in the sensor is accompanied by no ionization signal. These events are characterized by a faster heat pulse. They are identified by processing twice each heat sample: at the beginning with the normal reference and then with the NTD-event pulse template. The discriminating variables is the χ^2 between the two fits. The latter template is built using a small sample of such events with a large amplitude detected by absence of ionization signal and a large χ^2 value for the fit with reference template. In Fig. 3.2 an example of such NTD pulse is given.

3.2 Energy Calibration

The signals recorded (both ionization and heat) are first calibrated using ^{133}Ba gamma-ray sources, producing energetic electron recoils (up to 383.9 keV). This energy scale is called keV-equivalent-electron (keV$_{ee}$) since the energy

[1] Analog-to-digital unit. A number representing an ADC output (Analog-to-Digital Converter). The relationship between the ADUs and the voltage output of the amplifier depends on the ADC range and its number of bits.

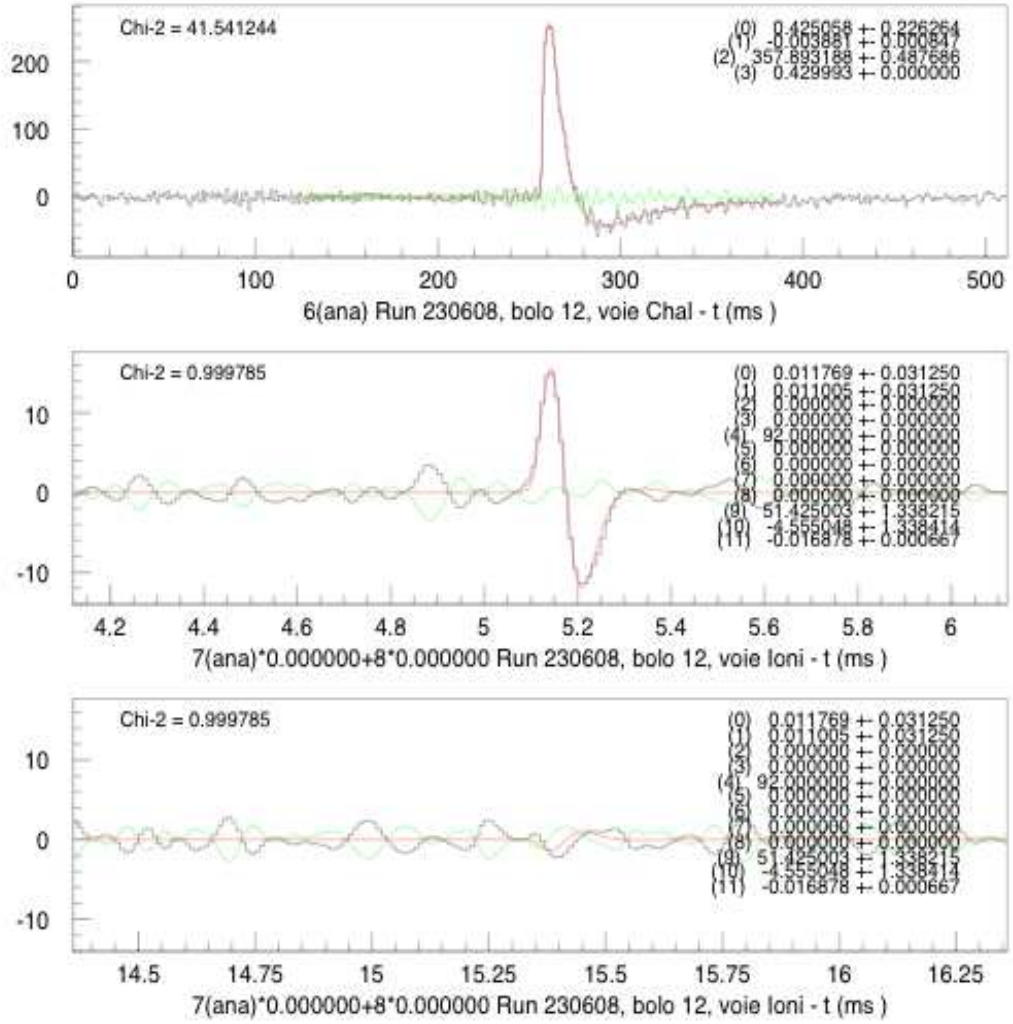

Figure 3.1: Exemple of filtered heat and ionization (center and guard) pulses.

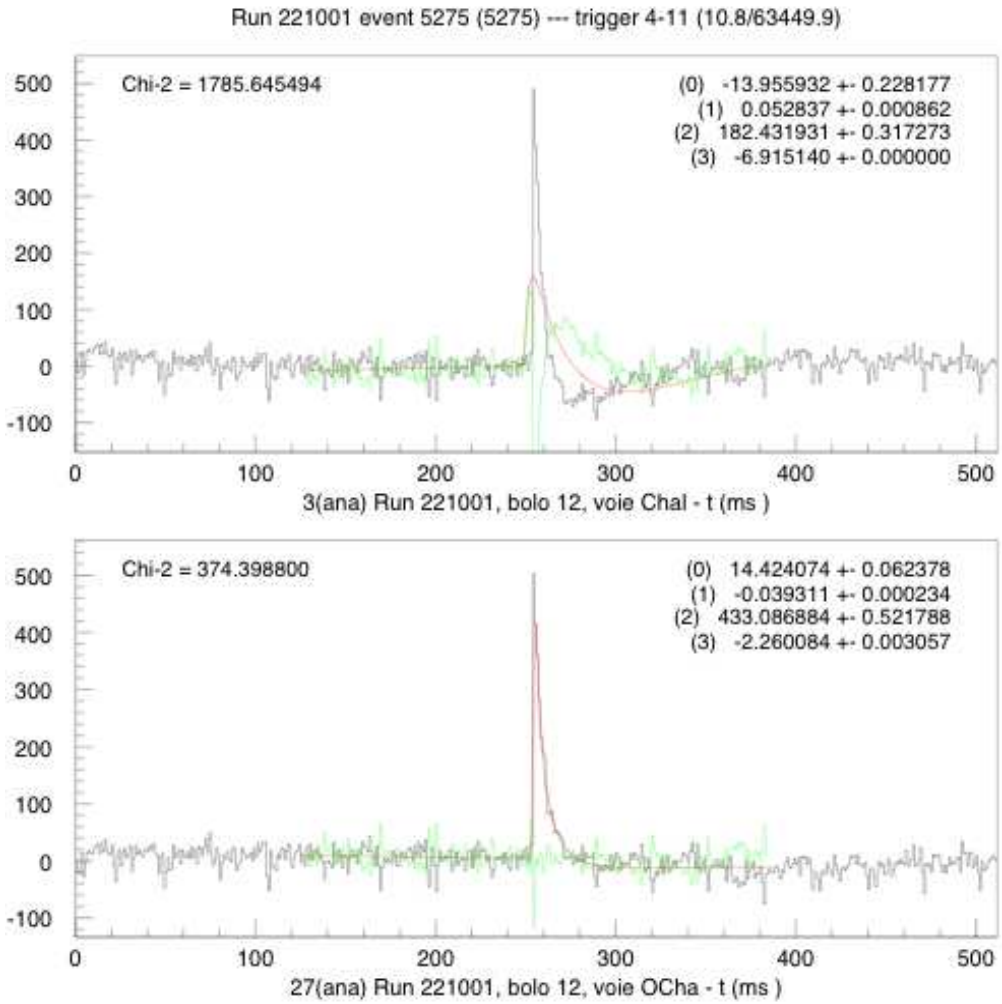

Figure 3.2: Exemple of filtered heat NTD pulses, in black, adjusted with the normal shape reference in red (top pannel) and with the NTD shape reference (bottom pannel).

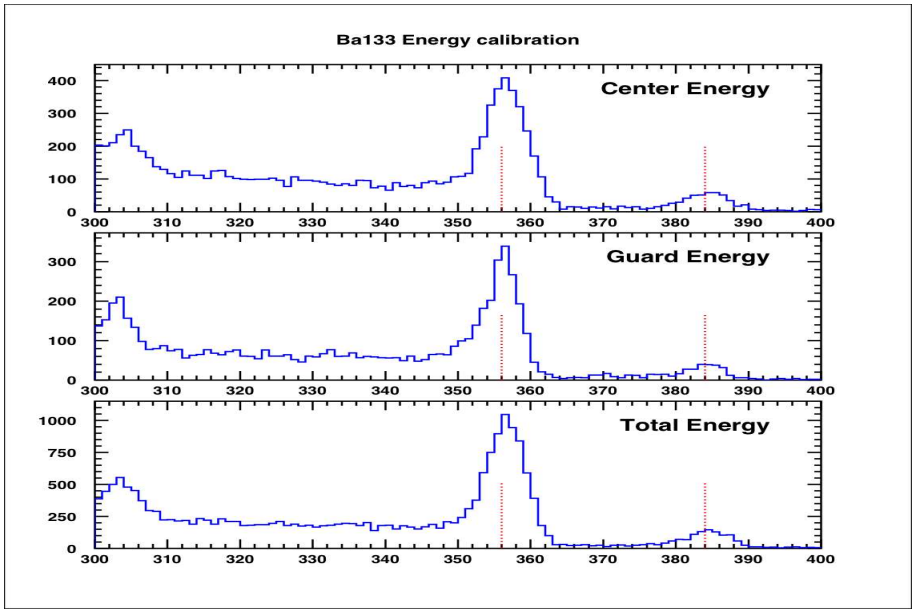

Figure 3.3: Center, guard and total ionization energy spectra. The gains are found by adjusting the peaks at 356 keV and 383.9 keV.

value corresponds to the actual energy deposit only for electron interactions.

In ^{133}Ba γ-ray calibration run the 356 keV and 383.9 keV peaks are clearly visible on the spectra, allowing a precise calibration of ionization signal, as shown in Fig. 3.3. Because of parasite capacitance between the centre and the guard electrodes, a charge fully collected on an electrode also induces a signal on the other. This cross-talk of a few percents is purely linear and remains constant in time for a given detector if no problems occur. As shown in Fig. 3.4 it can be easily corrected offline.

The ionization cross-talk η and gains δ are determined from the known energies E_I of the peaks from the Equation:.

$$E_{Ic,Ig} = \delta_{Ic,Ig}(A_{Ic,Ig} + \eta_{Ic,Ig} \times A_{Ig,Ic}) \tag{3.1}$$

where A_{Ic} and A_{Ig} are respectively center ionization amplitude and guard ionization amplitude in ADU. The total ionization signal is defined as the sum of central electrode and guard ring signal amplitude after correction of the cross-talk and calibration of the two channels.

The heat signal amplitude A_H is periodically calibrated using the same ^{133}Ba gamma-ray sources, Fig. 3.5. In contrast with ionization, heat appears to be sensitive to long term drifts of the NTD temperature: for instance

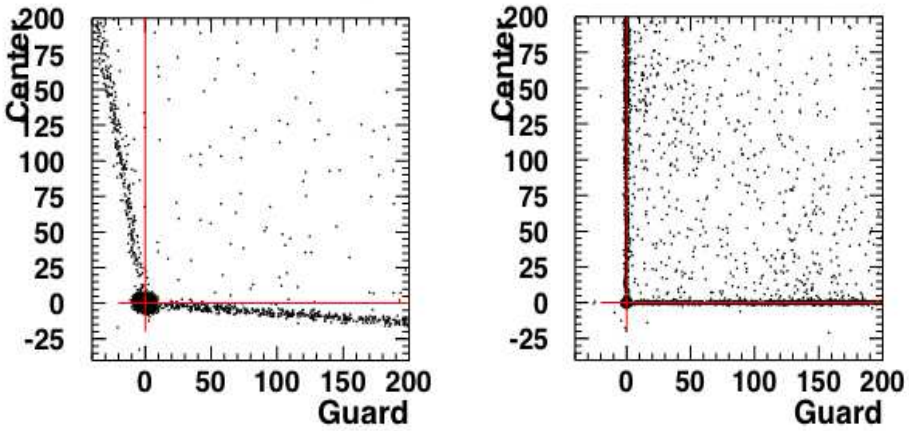

Figure 3.4: Center versus guard ionization signal for ^{133}Ba γ-ray calibration data acquisition of about 20 hours. *Left side*: without any crosstalk corrections. *Right side*: with cross talk correction.

it may vary of few percent several hours after cryogenic Helium transfers. Thus, between two γ-ray calibration runs we have to monitor the heat calibration using data from low-background runs themselves by setting average quenching factor value to 1 for electron recoils.

The heat channel has a non-linearity that is well reproduced by the following parametrization:

$$E_{H-L} = A_H \times \alpha \tag{3.2}$$

$$E_H = E_{H-L} \times (1 + \beta \log(E_{H-L}/356)) \tag{3.3}$$

where A_H is the amplitude (in ADU), E_{H-L} is the heat energy in keV calibrated using only the linear term α, and E_H is the heat channel in keV with the full calibration.

The parameters α and β are determined from the ratio of the amplitude A_H to the calibrated ionization energy. When possible, only pure center events are used. Typical values for β are of the order of ± 0.05.

For guard events, it has been observed that the heat pulse shape is not the same as for pure center events because of cross-talk effects between ionization and heat. For these events, the E_{H-L} value is calculated as:

$$E_{H-L} = A_H \times \alpha / r$$

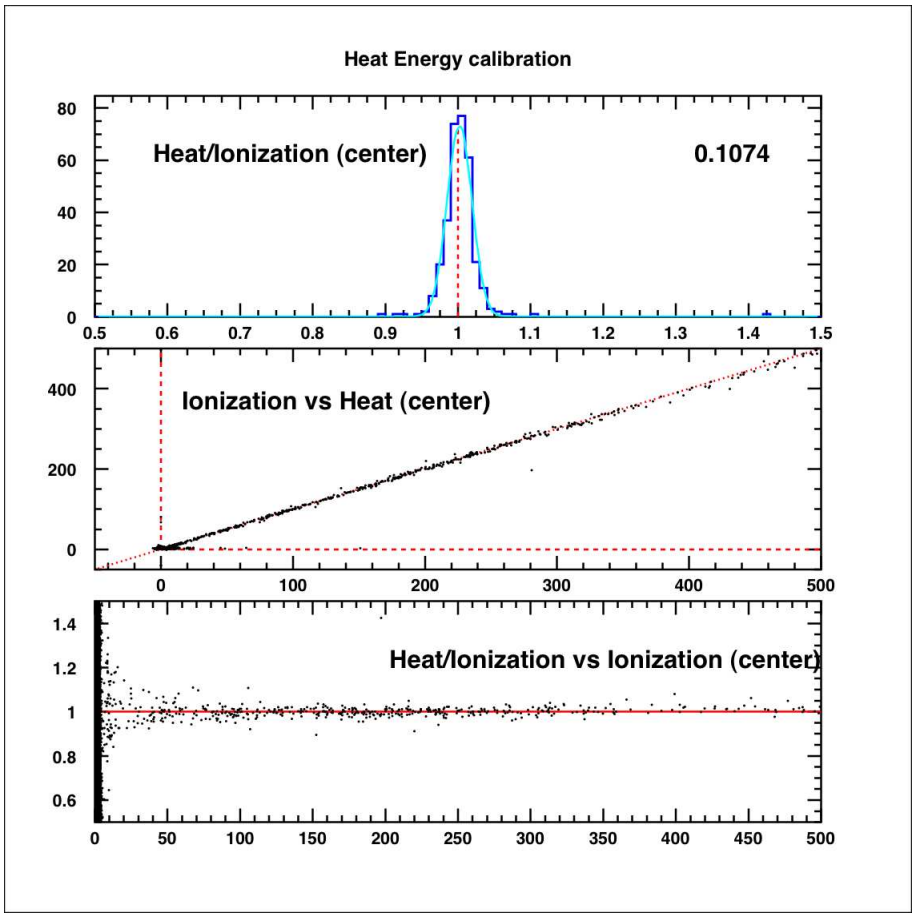

Figure 3.5: *Top pannel*: heat over ionization signals spectrum in the pure center volume. Noticing that for γ-ray the ionization signal has to be equal to the heat signal, the distribution has to be set at one. *Middle*: ionization signal as a function of heat signal. As above, γ-ray events will take place along the diagonal. This two first plot allow the linear calibration of heat channel (α coefficient). *Bottom pannel*: heat over ionization signals as a function of ionization signal for the center selection. This close-up allows a more precise determination of the β parameter.

where r is a ratio close to 1. For intermediate events (significant signal on both center and guard), the calibration is:

$$E_{H-L} = 2 \times A_H \times \alpha/(1+r)$$

3.3 Resolution of heat and ionization channels

Signal resolutions are needed in order to determine electronic and nuclear recoil zones but especially to determine if a detector can be used for WIMP searches. For each detector, the baseline resolutions of the heat and the two ionization channels are regularly controlled by inspecting the distribution of fitted amplitudes in events where the trigger occurred in another detector. In these fits, the pulse is fixed to the position given by the trigger detector. These data show that the noises of the three channels are not correlated. The ionization baseline resolution σ_I^0 can therefore be written as a function of the values for center and guard as:

$$(\sigma_I^0)^2 = (\sigma_{center}^0)^2 + (\sigma_{guard}^0)^2 \tag{3.4}$$

Average values obtained during the studied gamma and low background runs are given in Tab. A.1.

The ^{133}Ba calibrations give a measurement of the resolutions for the ionization and heat signals at 356 keV. Typical values obtained for detectors studied are given in Tab. A.2.

Heat and ionization signal resolutions have been parametrized as a function of the electron-equivalent energy as follow:

$$\sigma_{I,H}(E) = \sqrt{(\sigma_{I,H}^0)^2 + (a_{I,H}E)^2}, \tag{3.5}$$

where factors a_I and a_H are deduced from the resolutions at 0 and 356 keV.

$$a_{I,H} = \frac{\sqrt{\sigma_{I,H}^2(356) - \sigma_{I,H}^2(0)}}{356}. \tag{3.6}$$

3.4 Electron and nuclear recoil zones standard deviations

Now we can determine electron and nuclear recoil zones using the measured resolutions σ. Figure 3.6 shows a (Q, E_r) data distribution obtained with an

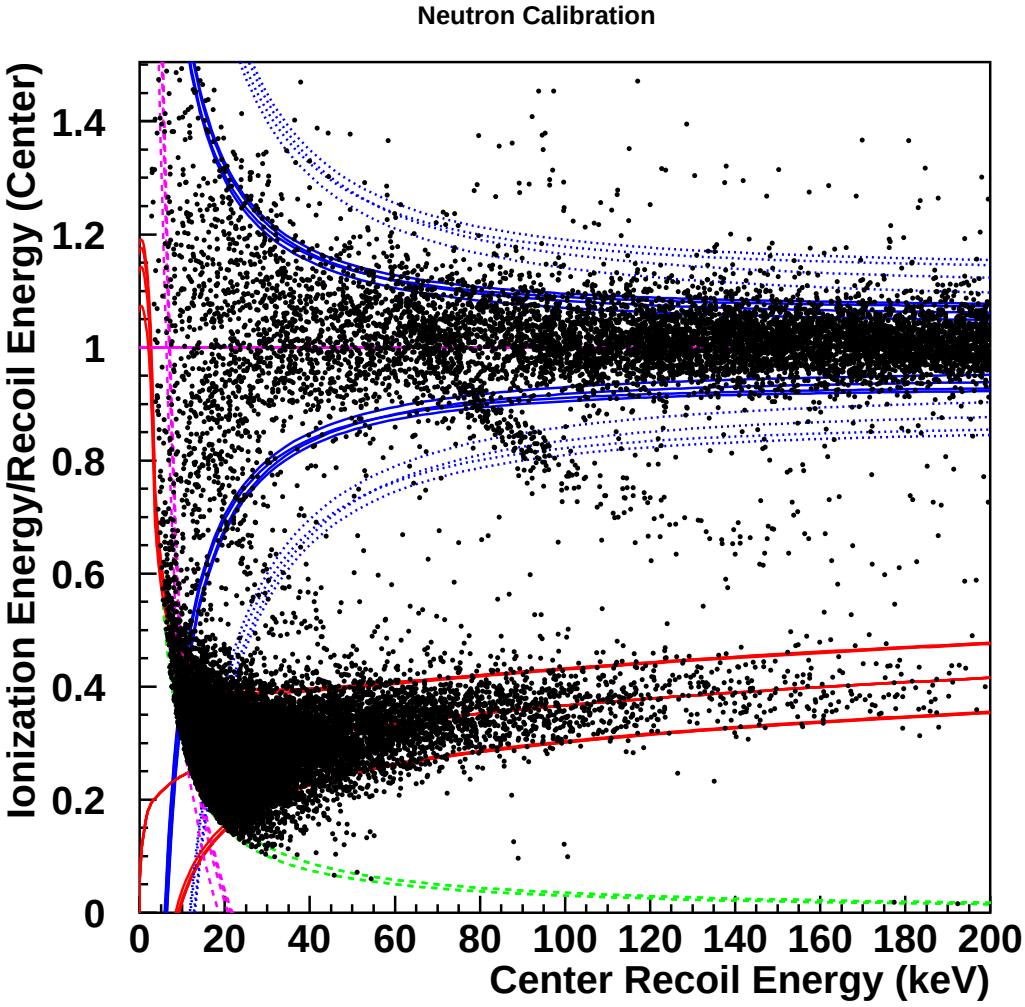

Figure 3.6: Projection in the (Q, E_r) plane of the events recorded during an Am-Be calibration. The thick lines represent the 90% nuclear (in red) and electronic (in blue) recoil zones ($\pm 1.645\sigma$ around $\langle Q_n \rangle$ and $\langle Q_\gamma \rangle$ respectively). Instead, blue dashed lines represent the 99.9% of electron recoil populations ($\pm 3.29\sigma$ around $\langle Q_\gamma \rangle$). Dotted green line represents ionization energy threshold (3.5 or 4 keV) and the pink one heat energy threshold.

Am-Be neutron source. Figure 3.7 shows that the measured Q values follow a gaussian distribution at the $\sim 2\sigma$ level for both nuclear and electronic recoils populations. In the case of a γ-ray calibrations, no events are seen for Q<0.6. This shows the excellent quality of the charge collection for the detector taken into account. This test is performed for every detector before a low-background physics run is started, to identify good detectors.

We therefore can parametrize the region of 90% acceptance for nuclear and electronic recoils by the following cut:

$$|Q - \langle Q_{\gamma,n}\rangle| \leq 1.645\sigma_{\gamma,n} \tag{3.7}$$

where $\langle Q_{\gamma,n}\rangle$ and $\sigma_{\gamma,n}$ are the average value and the standard deviation of Q distribution for nuclear (n) and electronic recoils (γ). Both variables are determined for each detector. In addition, for electronic recoil populations we define a region of 99.9% acceptance ($|Q - \langle Q_\gamma\rangle| \leq 3.29\sigma_\gamma$). This region is used to reject electronic recoils, even if the Q_γ distribution is not gaussian up to $3.29\sigma_\gamma$.

By construction, the ratio of the ionization energy to the recoil energy, Q, is equal to 1 for energy deposits coming from γ-rays. For neutrons, Q is a function of E_R; the average value of $Q(E_R)$ is well described by

$$\langle Q_n\rangle(E_R) = a(E_R)^b$$

with E_R in keV, where a and b parameters result from the fit of recorded neutron calibration data for each detector. The data is consistent with the values a=0.16 and b=0.18 quoted in [108], and we will use this value in this work.

From the dispersion of these data is deduced the nuclear recoil band, defined as the region in the (E_r, Q) plane where 90% of nuclear recoils are expected. The widths of electronic and nuclear recoil bands are given in units of standard deviations of electronic and nuclear distribution. They can be calculated with Eq. (2.12) and Eq. (2.13) by propagation of the experimental dispersions σ_I and σ_H:

$$\sigma_{Q_\gamma}(E_R) = \frac{(1+V/3)}{E_R}\sqrt{\sigma_I^2(E_R) + \sigma_H^2(E_R)} \tag{3.8}$$

$$\sigma_{Q_n}(E_R) = \frac{1}{E_R}\sqrt{\left[\left(1+\frac{V}{3}\langle Q_n\rangle\right)\cdot\sigma_I(E_R)\right]^2 + \left[\left(1+\frac{V}{3}\right)\langle Q_n\rangle\cdot\sigma_H(E_R)\right]^2} \tag{3.9}$$

A previous investigation [110] has measured a broader nuclear recoil Q distribution than the one expected from Eq. (3.9) at high energy for neutron

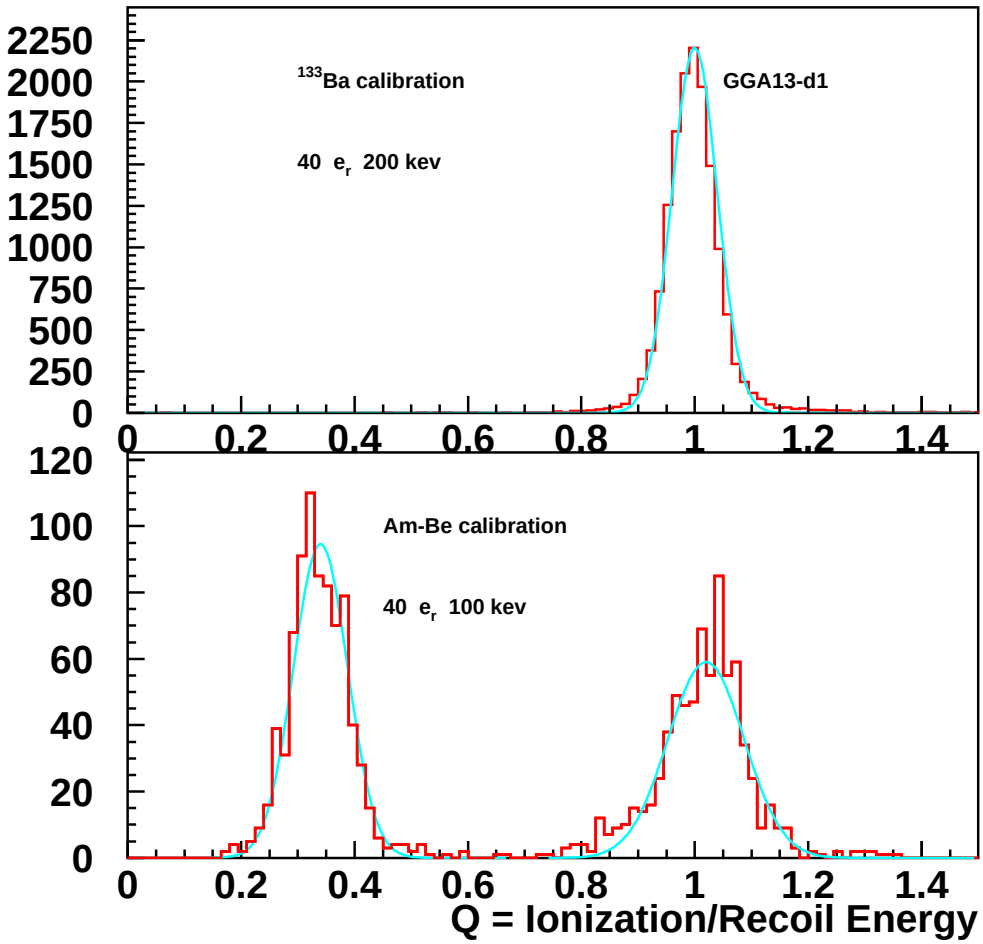

Figure 3.7: Top pannel: spectrum of the Q variable in the 40-200 keV recoil energy range for events recorded for detector GGA13 during a ^{133}Ba calibration (electron recoils). Bottom pannel: spectrum of the Q variable in the 40-100 keV recoil energy range for events recorded in the GGA13 detector during a Am-Be calibration (nuclear and electronic recoils).

calibration data (^{252}Cf source). So the width σ_{Q_n} of Eq. (3.9) has to be smeared by an additional spread C, as follows:

$$\sigma'_{Q_n}(E_R) = \sqrt{\sigma_{Q_n^2}(E_R) + C^2} \tag{3.10}$$

The constant C represents the effect of multiple neutron scattering and energy straggling in the stopping of Ge recoils. Experimental σ_{Q_n} in neutron calibration runs are well reproduced with C=0.035.

3.5 Thresholds

The issue of thresholds is greatly simplified by the a priori choice of using the recoil energy range above 30 keV in the WIMP search analysis. Instead of precisely measuring the experimental thresholds, one just need to verify that their upper limits are compatible with a full efficiency in the nuclear recoil band above 30 keV.

The threshold energy values are defined as the energy of the channel under study (in keV$_{ee}$) for which the trigger efficiency reaches 50%. It is the most important parameter governing the dependance of the efficiency on the recoil energy. Indeed, from Eq. (2.13), we can deduce that in the (E$_r$, Q) plane ionization threshold will cut as an hyperbole

$$Q = \frac{E^I_{th}}{E_R} \tag{3.11}$$

Using relations in Eq. (2.13) and Eq. (2.12), in the (E$_r$, Q) plane the heat threshold cut assumes the shape

$$Q = \frac{1 + \frac{\epsilon_\gamma}{V} \cdot E^H_{th}}{E_R} - \frac{\epsilon_\gamma}{V} \tag{3.12}$$

where ϵ_γ is defined in Sec. 2.3.1.1. Having a look at their shapes in Fig. 3.6, the heat energy threshold appears less dangerous than the ionization one. The efficiency for nuclear recoils is 90% as long as the lower limit of the nuclear recoil band is above these two threshold cuts at 30 keV. For low quenching factors below the nuclear recoil band, the ionization cut is more strict than the heat threshold cut. There is enough statistics in γ and neutron calibration runs to measure the values of E$^H_{th}$ and E$^I_{th}$.

The γ-ray calibration runs allow a measure of the highest of the two energy thresholds (ionization or heat). The measurements method is the following. A γ-ray spectrum is recorded using a ^{133}Ba source producing an important Compton plateau. It can be assumed that the plateau shape for

energies above 10 keV corresponds to a maximum efficiency. Fitting the energy spectrum by an integral of a gaussian, it yields to the experimental value of E^{γ}_{th}, which is defined as half of its rise to its constant value (Compton plateau). Since E_I=E_H for γ-rays, it is not possible here to determine which of the two channel is imposing the observed cut. This method is limited by the large data sample needed to obtain a significant number of events in the threshold region.

In contrast, the neutron calibration fills both the electron and recoil bands and permits a separate investigation of these two zones. In particular, for nuclear recoils, the threshold measured on the heat and ionization signal are not the same. Because of the quenching effect, $E^{I,n}_{th}$<$E^{H,n}_{th}$.

In the case of an online heat trigger, it is expected that $E^{H,n}_{th}$=E^{γ}_{th}, as long as the offline analysis can find the associated signal down to a threshold $E^{I,n}_{th}$<$E^{H,n}_{th}$. This set the upper bound on the ionization threshold, as the observed $E^{I,n}_{th}$ may be due to the constraint on $E^{H,n}_{th}$ and not to efficiency of the offline ionization reconstruction.

It is then left to verify that both the online E^{H}_{th} threshold value and the upperbound on E^{I}_{th} due to the offline algorithm to find the ionization signal associated to the heat pulses, are compatible with a recoil threshold below 30 keV.

In the other case where $E^{I,n}_{th}$=E^{γ}_{th}, we would have obtained an upper limit on E^{H}_{th} instead.

In practice, in the case of an online heat trigger, it is useful to set an analysis cut on ionization in order to remove heat-only signals from the plots. This cut can be set at the values obtained in the neutron calibration. However, noise conditions may vary as a function of time in the long physics run. We then use a value just above the noise peak, determined on a monthly basis, taking care that this cut does not affect the nuclear recoil band.

3.6 Fiducial volume

The role of the guard electrode is to tag interactions occurring in the outer perimeter of detectors. This zone is more exposed to external sources of radioactivity such as the NTD thermal sensor and the Cu support springs. It is also sensitive to charge collection problems; interactions in this region can also suffer from electric field inhomogeneities thus simulating ionization deficit expected for nuclear recoils. For these reasons, a fiducial volume cut is needed. In ref. [60] more than 75% of the total charge must be collected on the center electrode. Here, because of a bad resolutions on many guard ionization channels, we have focused adopted a “pure center” selection instead. This

cut redefines the fiducial volume selection requiring the absolute value of the guard energy to be lower than two times of the guard baseline resolution σ_g.

This stricter definition should reduce the fiducial volume fraction by a few percent from the value obtained in [110] with the 75% cut. However, this reduction is compensated by a reduction of the volume under the bevelled part relative to the old EDELWEISS detectors, compensating for this loss. We thus kept a fiducial volume value of 180 g.

3.7 Analysis strategy and quality cuts

We have defined a bolometer as a valid one for WIMP search if it responds to two tests: the γ-ray calibration test and the magic point test.

The first test concerns the study of the distribution of the quenching factor Q recorded with a γ-ray source, revealing any problems with the charge collection.

Second one is the magic point test. This point being the intersection of the γ band at 99.9% and the neutron band at 90%, it depends on baseline resolutions and 356 keV peak resolutions. Thus only bolometers with resolutions good enough to achieve a 30 keV magic point are taken into account in our analysis. Moreover, supposing that the ionization baseline resolutions and resolutions at 356 keV are stable during a run we are able to calculate a maximum heat baseline resolution that permits to obtain our a-priori chosen magic point at 30 keV. This calculation has been made by inverting Eq. (3.8) and Eq. (3.9).
The following table (Tab. 3.1) lists, as a function of ionization baseline resolution (IBR), the maximum acceptable heat baseline resolution (Max HBR) for obtaining a magic point of 30 keV.

For detectors whose average heat and ionization baseline resolutions pass the magic point test, we select hour by hour the time periods where the detector was operating in stable conditions. This procedure is called the good hour selection. It is carried out in three steps:

* Firstly, we perform a test to find out the real length of the run. For example, we do not consider time intervals that correspond to a null polarization voltage or a known electronic problems, etc.. But this interval may correspond to a non integer number of hours. We split the hours in 15 minute partitions due to the low event rate expected in physics runs. It is required that there should be at least one count with a positive heat signal in each 15 minute bin. The length of the run is the number of such bins.

IBR	Max HBR	IBR	Max HBR
1.0	3.446	1.1	3.408
1.2	3.375	1.3	3.339
1.4	3.296	1.5	3.250
1.6	3.196	1.7	3.145
1.8	3.085	1.9	3.023
2.0	2.958	2.1	2.885
2.2	2.802	2.3	2.721
2.4	2.634	2.5	2.537
2.6	2.417	2.7	2.316
2.8	2.182	2.9	2.038
3.0	1.884	3.1	1.707
3.2	1.474	3.3	1.170
3.4	0.720	3.5	0.336

Table 3.1: Maximum heat baseline resolution as a function of ionization baseline resolution.

* The second and third steps are to perform a hour selection by an ionization and heat baseline resolution cut. The idea is to reject hours with a baseline resolution higher than a chosen maximum acceptable value. These cuts remove effectively periods where noise changes rapidly and the baseline resolution (and therefore the width of nuclear and electronic bands) cannot be evaluate reliably. To have a reliable monitoring of the ionization baseline resolution hour by hour, despite the low statistics, we use a three-hour averaging window. To succeed in this, we measure the FWHM (keV) of the baseline distribution only for the good run hours found at the previous step which have at least 5 counts in these hours.

  We perform these baseline cuts over each acquisition month for all bolometers in order to select stable periods (i.e. to cut noisy period occurring soon after detector regeneration).

  The ionization cut accepts an hour as a good one only if its FWHM (keV) value is below a fixed threshold, chosen as a percentage ([%]) of the average value $\langle \text{FWHM} \rangle$ over whole acquisition month. It means that the FWHM_{max} is equal to $\langle \text{FWHM} \rangle$ + [%] $\langle \text{FWHM} \rangle$.

  The choice of the percentage for this cut will be discussed in chapter 4.

  The same test is also performed on the heat FWHM. There is however the additional constraint that the FWHM value also be compat-

ible with a magic point below 30 keV. As the heat FWHM fluctuates more than the ionization values, this cut is made stricter by requiring that the baseline FWHM should be lower than ⟨FWHM⟩ + [%] ⟨FWHM⟩+σ_{FWHM}, where σ_{FWHM} is the measurement error on the hourly FWHM baseline.

Fig. 3.8 shows, as an example, the baseline resolution of the detector GGA13 during december 2007 as a function of time in hours.

The *upper pannel* shows the ionization keV FWHM value as a function of time in hours for the first selection that we have made. The blue region represents hours not considered for physics (for example, it can be due to a problem, a regeneration or to a calibration run). The light green dotted line is the average of ionization baseline resolution and the pink one is the maximum acceptable ionization baseline corresponding to its average value plus 30%. The pink line is equal to one if we accept the hour and zero otherwise.

The *bottom pannel* presents the heat keV FWHM value as a function of time in hours, after ionization FWHM selection. The red dotted line is the maximum acceptable heat baseline resolution to have a 30 keV magic point for this detector. The light green line is the average of heat baseline resolution and the light green dotted one is the average value plus 30%. As before, the pink line is equal to one if we accept the hours and zero if we reject it: we accept one hour as a good one only if the heat baseline value for this hour plus its statistical error bar is below the smallest value between the heat baseline value that permits to achieve a 30 keV magic point and the 1.3 times the mean heat baseline value. Making this hard cut, points having large error bars are rejected. This reflects the fact that heat variations are more random than those of ionization, and any variation is a priori suspected.

Finally, we count how many hours are selected for each bolometer. The exposure, expressed in kg·days, is then calculated by multiplying these accepted hours by the fiducial detector mass, weighted by the number of 5-minute bins with at least one count within each hours.

The correction for the dead time is made by multiplying each hour by a weight factor equal to (1-τ_{dead}×R), where R is the hourly event rate in Hz and τ_{dead} is the 0.25 s dead time.

3.8 WIMP candidate selection

To summarize, the selection criteria that allow us to consider an event as a WIMP candidate are the followings:

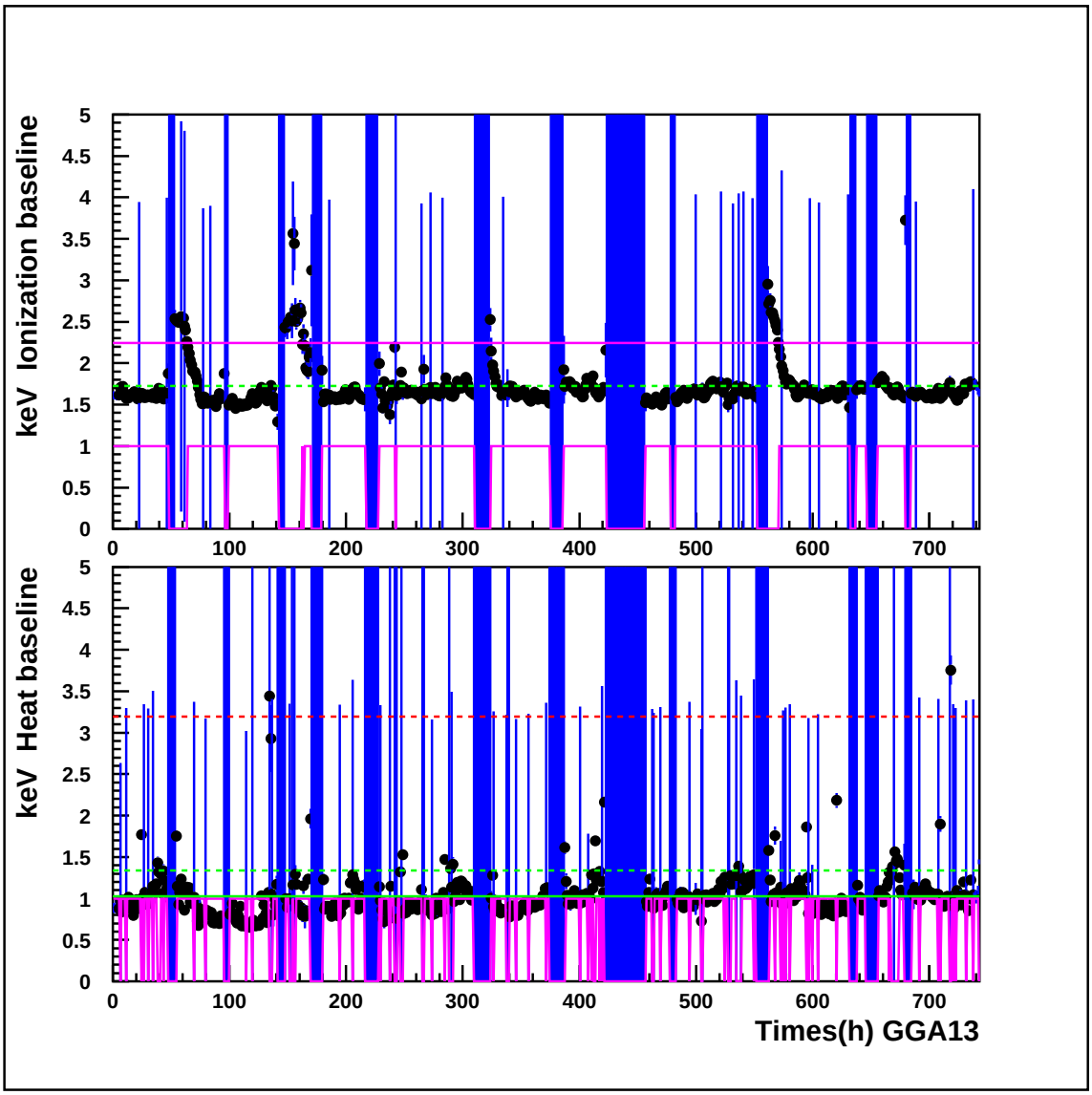

Figure 3.8: Example of quality cuts performed: keV FWHM as a function of time express in hours, for data recorded during December 2007 in GGA13 detector .

- The event has to take place in the fiducial detector part: it means that the guard energy must be smaller than 2 σ_{guard}. A corresponding 5% inefficiency is taken into account in the limit calculation.

- Ionization and heat signals have to be above their respective defined hourly threshold (this automatically reject events in the 99.9% electronic recoil region).

- The event, defined as a point in the (Q, E_R) plane has to be in the defined 90% nuclear-recoil region, and be above E_R=30 keV.

- It has to be a simple event (only one detector triggered).

- The χ^2 of the heat fit has to be lower than the χ^2 for the fit with the NTD event template.

Nuclear and electronic recoils band are defined for each bolometer and for each acquisition month by Eq. (3.10) and Eq. (3.8).

Chapter 4

Physics Run: 8^{th} cool down

The low background physics data I have studied has been collected during the 8^{th} cool down of EDELWEISS-II ("run 8"). It consists of all physics runs recorded over a period from November 2007 to March 2008. The previous cool-downs were devoted to commissioning runs. A ^{133}Ba γ-ray calibration run precedes the physics data taking to guarantee a reliable ionization and heat channel calibration. In addition to a constant monitoring of the data, the homogeneity of the running conditions was checked with quite regular weekly γ calibration and neutron calibration periods.

Nineteen detectors have been involved in this run. Among them we have the first ID detector [111] and one IAS detector [112] (heat and scintillation detector). The present analysis is focused on the remaining 17 standard Ge-NTD detectors similar to those employed in EDELWEISS-I [108]. Detectors were located in three-bolometer towers in the cryostat. Fig. 4.1 shows the cryostat geometry and Ge-NTD detector position and features.

Figures and tables of major importance are presented in this chapter, the others can be found in Appendix A.

4.1 Detector performance and selection

As mentioned in the previous chapter the goals of Ge-NTD detector analysis are a better understanding of the radioactive background of the experiment and an improvement of current EDELWEISS upper limits on the WIMP scattering cross section in case of an unsuccessful WIMP detection. In the following sections I will present results and discussions about these two issues. The first step in the physics data study is the calibration of all detectors (see Sec. 3.2) in order to find out the essential features such as baseline resolutions, 356 keV peak resolutions and energy thresholds, as explained in Sec. 3.2 and

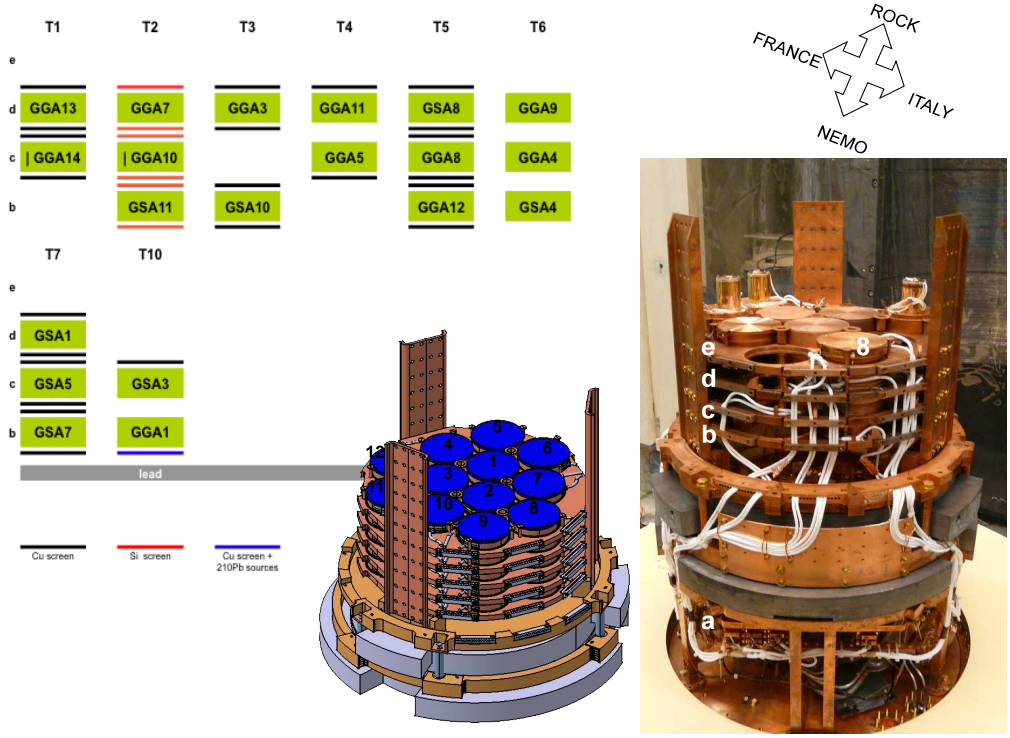

Figure 4.1: Bolometers position in cryostat during 8^{th} low background physics run, together with an actual picture of the setup (for the $10th$ cool down).

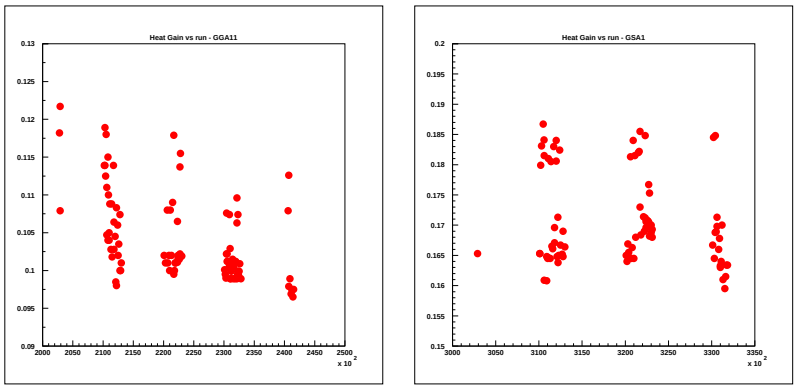

Figure 4.2: GGA11 and GSA1 heat gain jumps observed during calibration.

Sec. 3.5.

Bolometers in tower 10 cannot be used for WIMP limits: GGA1 have to be studied apart because it is equipped with a dedicated ^{210}Pb source (Section 4.3.2.1) and GSA3 has a large alpha background (Tab. A.16). Thus, fifteen Ge-NTD bolometer type are left for the WIMP search.

The calibration procedure already shown some problems with GGA11 and GSA1: the heat over ionization calibration gain exhibits unexpected jumps, as shown in Fig. 4.2. The ionization calibration is stable, resulting in a constant gain during all the data taking. The problem is most likely due to unexplained heat gain variations. These two bolometers have not been retained for the WIMP search. The search is thus performed with the 13 remaining detectors.

Tab. A.1 and Tab. A.2 present average baseline and 356 keV resolutions for heat, center and guard ionization channels during ^{133}Ba γ-ray calibration and low background physics run. These values allow a first bolometer selection based on the magic point as explained in Sec. 3.7. We are able to calculate the intersection between 99.9% gamma band and 90% neutron band depending on baseline and 356 keV peak resolutions: the results for each detector are listed in Tab. 4.1. The detector GGA8 does not pass this selection, and we are left with twelve detectors.

The next issue is the energy thresholds as evaluated by the γ-ray and neutron calibration runs, outlined in Sec. 3.5. Values are tabulated in Tab. 4.2 and in Tab. 4.3. For the γ-ray calibration runs we notice that for bolometers GSA11 and GSA7 the values found for heat and ionization are not compatible. The difference Δ_E between ionization and heat values will be taken as a systematic error ($\Delta_E(keV)$: GSA11 (2.5$\pm$0.1) and GSA7 (1.60$\pm$0.05)). This could be related to charge collection problems on GSA11 and to noisy period

Mac	No	Pos.	Name	MP (keV)	status
1	4	c1	GGA14	19.5	1
1	5	d1	GGA13	15.5	1
1	6	b2	GSA11	17.5	1
1	7	c2	GGA10	18.5	1
1	8	d2	GGA7	25.5	1
1	9	b3	GSA10	20.5	1
1	10	d3	GGA3	20.5	1
2	11	c4	GGA5	17.5	1
2	14	c5	GGA8	45.5	0
2	15	d5	GSA8	29.5	1
2	17	c6	GGA4	16.0	1
2	18	d6	GGA9	15.5	1
3	19	b7	GSA7	25.5	1
3	22	b10	GGA1	27.0	1
3	23	c10	GSA3	49.0	0

Table 4.1: Magic point values (MP) for each bolometer taking into account the experimental resolutions. The "status" is 1 for a good bolometer (our a priori choice: MP <30 keV), 0 otherwise.

No	Name	E^{γ}_{th} measurement (keV) by ionization	by heat
4	GGA14	6.2±0.4	6.3±0.4
5	GGA13	10.3±0.5	10.6±0.7
6	GSA11	7.2±0.6	9.7±0.5
7	GGA10	4.5±0.9	4.5±1.0
8	GGA7	17.8±1.2	17.2±0.4
9	GSA10	14.1±1.4	13.8±0.8
10	GGA3	6.4±0.3	6.1±0.2
11	GGA5	5.3±0.3	5.8±0.2
15	GSA8	10.7±0.4	11.8±0.2
17	GGA4	4.0±0.4	4.6±0.1
18	GGA9	4.3±0.3	4.9±0.2
19	GSA7	11.9±0.5	10.3±0.3

Table 4.2: E^{γ}_{th} thresholds (keV) from ^{133}Ba calibration runs measured by ionization and by heat. They should have the same values due to the fact that for gamma ionization energy is equal to heat energy. It is almost the case except for GSA11 and GSA7. Indicated statistical errors.

during the whole run (no baseline resolution quality cut has been performed for threshold studies during γ-ray calibration run).

Heat energy threshold values from the neutron calibration run are consistent with those found with the γ-ray calibration investigation, an expected outcome in the case of an online heat trigger combined with an efficient offline algorithm to find the associate ionization signal. The upper limits on the ionization threshold are between 3 and 4 keV, except for GGA7 at 5.4 keV. All these threshold values are compatible with the a priori choice of a 30 keV recoil energy lower bound.

For physics runs, Tab. 4.4 indicates the upper limits of the ionization noise peak for each acquisition month. Overall, these are consistent with the ionization energy threshold limit derived from the neutron calibration run. In the few exceptions where the noise fluctuates above the upperbound from the neutron measurements, this value does not exceed 6.0 keV, and therefore does not affect the nuclear recoil band above 30 keV.

For the twelve detectors having a magic point lower than 30 keV (Tab. 4.1) and with a reliable γ-ray calibration, we are able to predict the γ rejection power. Making a comparison between the number of events in neutron band (NB) or for a quenching factor lower than 0.5 ($Q < 0.5$) and the total events

No	Name	Threshold (keV) $E_{th}^{I,n}$	$E_{th}^{H,n}$	Recoil
4	GGA14	3.3±0.1	6.5±0.1	13.3±0.2
5	GGA13	3.5±0.1	8.9±0.3	19.0±0.3
6	GSA11	3.6±0.1	7.7±0.2	16.8±0.4
7	GGA10	3.3±0.1	6.3±0.1	12.8±0.1
8	GGA7	5.4±0.2	11.1±0.3	23.8±0.4
9	GSA10	3.7±0.3	8.6±0.2	17.2±0.2
10	GGA3	4.0±0.4	6.6±0.1	13.9±0.1
11	GGA5	3.0±0.7	5.6±0.1	12.0±0.2
15	GSA8	3.9±0.3	10.5±0.2	21.6±0.2
17	GGA4	3.0±0.3	5.5±0.1	10.7±0.2
18	GGA9	3.4±0.1	6.1±0.1	12.2±0.1
19	GSA7	4.0±0.1	11.1±0.3	21.8±0.3

Table 4.3: Ionization and heat energy thresholds (keV) from neutron calibration runs and relative recoil energy thresholds. Indicated statistical errors.

No	Name	Ionization noise cut (keV) Nov07	Dec07	Jan08	Feb08	Mar08
4	GGA14	3.5	3.5	3.7	3.7	4.0
5	GGA13	4.0	4.0	3.0	3.7	3.0
6	GSA11	3.0	4.0	3.0	3.7	3.0
7	GGA10	3.4	4.0	3.7	3.7	3.5
8	GGA7	3.0	4.0	3.0	3.5	3.5
9	GSA10	3.0	6.0	4.0	3.5	4.0
10	GGA3	3.7	4.0	4.0	3.5	3.0
11	GGA5	3.0	3.0	4.0	3.0	3.0
15	GSA8	5.5	3.5	2.5	4.0	5.0
17	GGA4	3.5	3.5	3.0	3.5	3.2
18	GGA9	3.0	4.0	4.0	4.0	4.0
19	GSA7	3.0	5.0	5.0	6.0	5.0

Table 4.4: Ionization threshold (keV) from low background physics runs.

No	Name	Number of events			Rejection	
		ALL	NB	Q < 0.5	NB	Q < 0.5
4	GGA14	4630	0	0	5.0E-04	5.0E-04
5	GGA13	23769	0	2	9.7E-05	2.2E-04
6	GSA11	3281	125	332	0.04	0.1
7	GGA10	8135	0	0	2.8E-04	2.8E-04
8	GGA7	671	0	0	3.4E-03	3.4E-03
9	GSA10	4008	0	0	5.7E-04	5.7E-04
10	GGA3	18362	0	0	1.3E-04	1.3E-04
11	GGA5	11667	1	1	3.3E-04	3.3E-04
15	GSA8	525	0	0	4.4E-03	4.4E-03
17	GGA4	2785	0	0	8.3E-04	8.3E-04
18	GGA9	9344	0	0	2.5E-04	2.5E-04
19	GSA7	3211	0	0	7.2E-04	7.2E-04

Table 4.5: γ rejection power obtained with analysis on ^{133}Ba gamma calibration runs. It is shown for two selected zones; neutron band (NB) and for a quenching factor less than 0.5 (Q < 0.5).

(ALL) recorded during γ calibration run we obtain the γ rejection values for a 90% C.L. given in Tab. 4.5.

The GSA11 detector exhibits an unexpected behavior. A large number of events were recorded in the neutron band and everywhere below the gamma band region (Fig. 4.3). This problem persist in all γ-ray calibrations. We conclude that GSA11 has a charge collection problem for a yet unknown reason and must be excluded from the WIMP search.

4.2 WIMP search

In this section data selection for the WIMP search and relative upper limit on the WIMP-nuclon elastic scattering cross section as a function of WIMP mass will be detailed.

4.2.1 Data selection

For the search of events as rare as WIMP interactions, we want our data to be as reliable as possible. To succeed in this we follow the data selection method described in Sec. 3.7 for the eleven selected detectors with magic point above 30 keV.

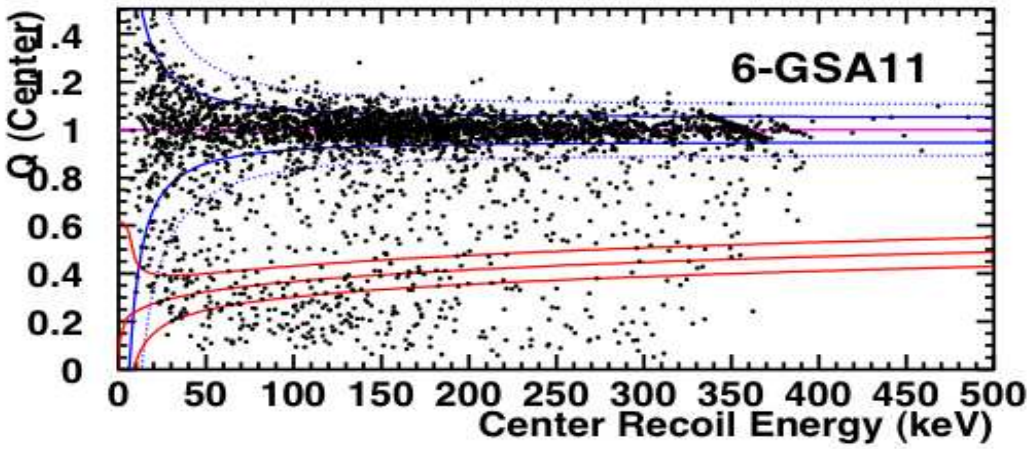

Figure 4.3: Data recorded during ^{133}Ba calibration runs in January 2008 for GSA11 detector.

The procedure to select the hours when the data quality of each detector is adequate for this search is described in Sec. 3.7. An important point is the choice of the percentage of the average baseline resolution that gives the maximum acceptable baseline resolution value. Just to recall, we have defined our maximum baseline resolution as

$$BL_{I,max} = \langle BL_I \rangle (1 + [\%]) \text{ for ionization}$$

$$BL_{H,max} = min(\langle BL_H \rangle (1 + [\%]), BL_H(30\ keVMP)) \text{ for heat}$$

where $\langle BL \rangle$ is the average baseline resolution value, $BL_H(30\ keVMP)$ is the heat baseline resolution calculated in order to achieve a 30 keV magic point (see Tab. 4.1) and the "[%]" is the chosen percentage.

Two different values of this percentage have been tested: 30 and 50%. For the 30% we obtain a fiducial exposure of 93.5 kg·d and 99.9 kg·d fiducial for the 50% cut (see Tab. 4.6). The difference between these two possible choices in terms of events recorded is shown in Fig. 4.4. The top pannel represents the 30% quality cut selection and the bottom one what would be added if the percentage was increased to 50%. The latter choice does not increase significantly the fiducial exposure, and even in terms of events there is not a very noticeable difference. I have chosen to be the most conservative as possible, selecting the 30% quality cut. This strict choice helps ensure the uniformity of the different resolutions that enter the calculation of the

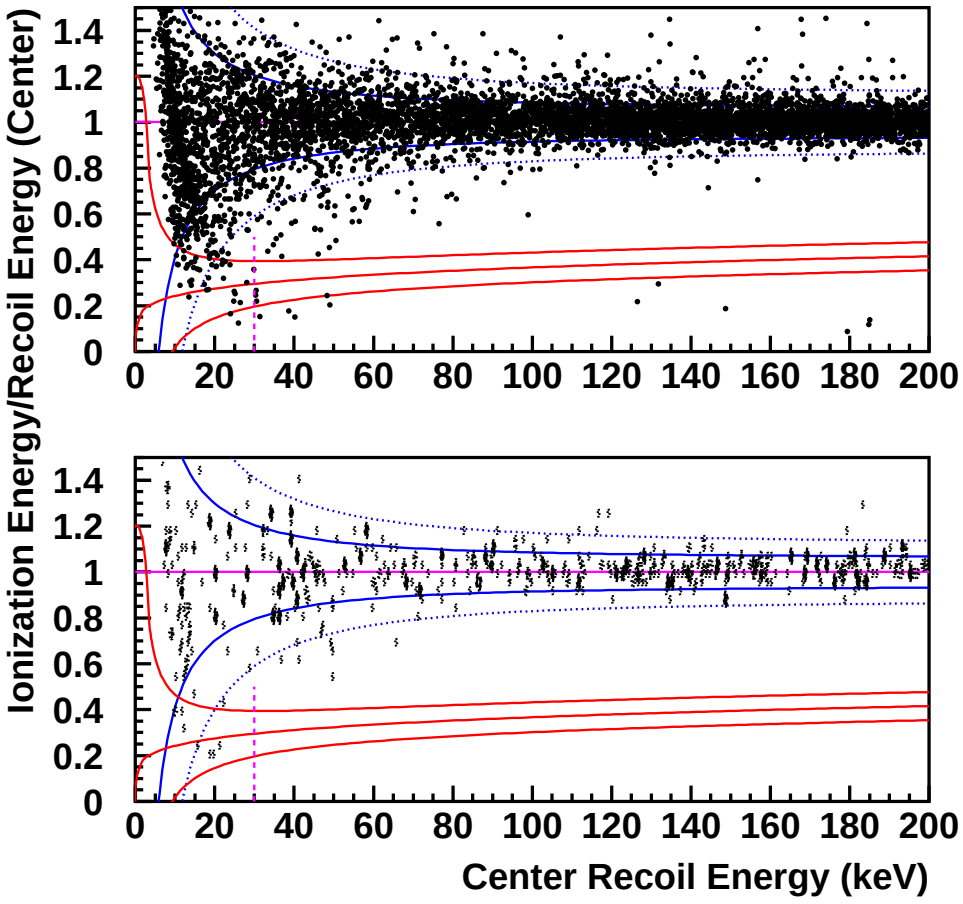

Figure 4.4: *Top*: all data recorded during low background physics run after 30% quality cut (fiducial exposure 93.5 kg·d). *Bottom*: data to add if we increase the quality cut percentage to 50%. Data added are within the 99.9% γ band. No events are observed in the 90% neutron band for recoil energy higher than the 30 keV low bound.

Mac	No	Name	All Stat kg·d (Fiducial)	
			30% cut	50% cut
1	4	GGA14	10.00	11.19
	5	GGA13	9.77	10.75
	7	GGA10	11.13	11.67
	8	GGA7	4.80	4.99
	9	GSA10	9.93	10.34
	10	GGA3	11.29	11.63
2	11	GGA5	11.15	11.80
	15	GSA8	0.77	0.77
	17	GGA4	9.27	10.49
	18	GGA9	9.91	10.76
3	19	GSA7	5.51	5.52
		Tot	93.53	99.91

Table 4.6: Number of kg·d exposure or fiducial volume after all quality cuts for the whole statistics.

electronic and nuclear recoil bands. The drawn bands should correspond rather closely to an efficiency of 90%. However, we see that relaxing this criterion does not add any WIMP candidates above 30 keV.

We can notice that the fiducial exposures obtained after the quality cuts are similar for all bolometers except for GGA7 and GSA8. An explanation is related to their magic point which is close to 30 keV (linked to large resolutions values).

The final Q-plot for the eleven detectors corresponding to a fiducial exposure of 93.5 kg·d are shown in Fig. 4.5 and in Fig. 4.6, where a zoom of the nuclear recoil band up to 100 keV recoil energy is presented. Taking into account the 30 keV threshold, 3 events are observed in the nuclear-recoil band, up to 200 keV.

As shown in Fig. 4.6 two events are very next to our imposed recoil threshold (respectively at 30.2 keV and 30.4 keV, see Tab. A) and the third one takes place at 41.8 keV. Simulated spectra of WIMPs having a scattering cross section on nucleons of 10^{-5} pb and masses of 20, 40, 100 and 500 GeV/c^2 are superimposed to the observed energy spectrum of these three events. They correspond to a rate in the recoil energy region between 30 and 200 keV of 0.03±0.02 evts/kg·d.

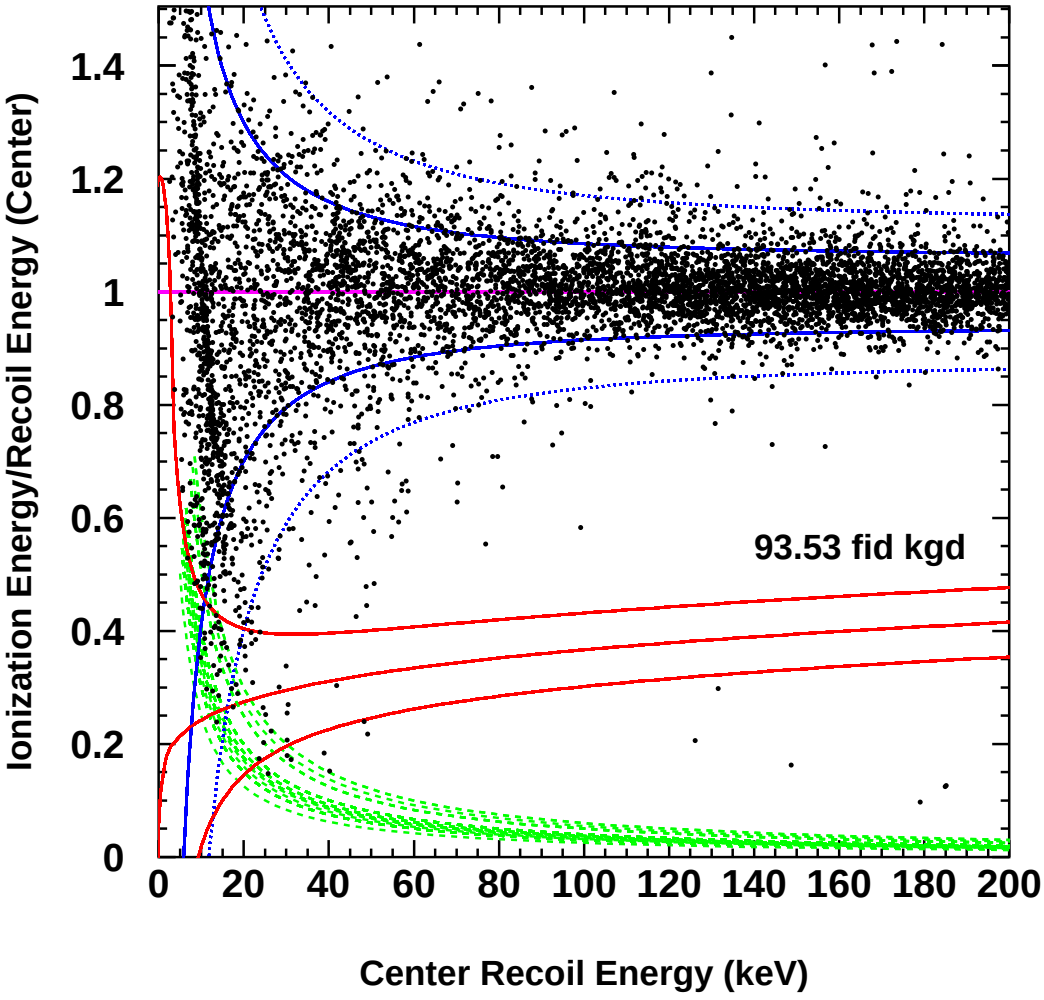

Figure 4.5: Distribution of the quenching factor (ratio of the ionization signal to the recoil energy) as a function of the recoil energy for the data collected in the (center) fiducial volume. The exposure of fiducial volume corresponds to 93.5 kg·d. Also plotted are the averaged $\pm 1.645\sigma$ band (90% efficiency) for photon recoils as blue full lines and for nuclear recoils as red dashed lines. The 99.9% efficiency region for photons is also shown (blue dotted line). Hyperbolic dashed curves correspond to ionization energy threshold for each detector and for each acquisition month.

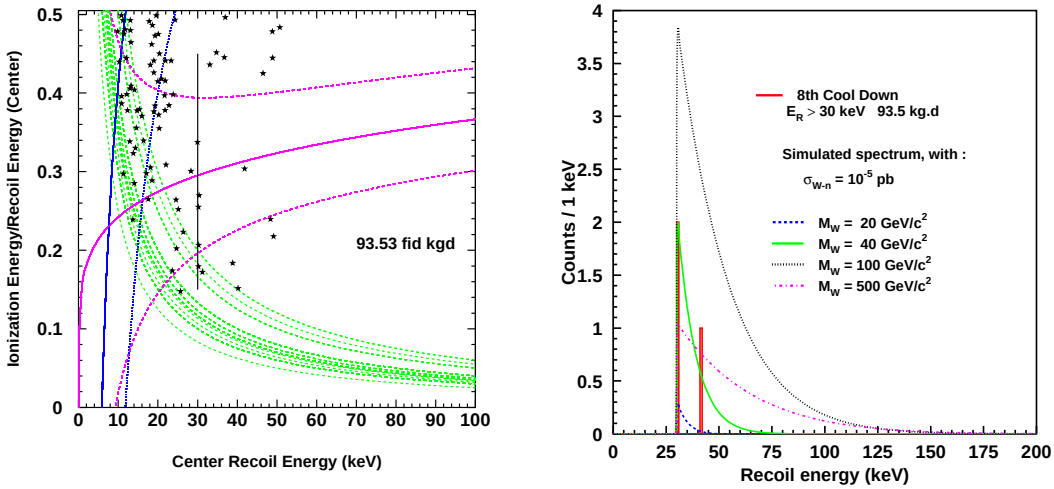

Figure 4.6: *Left side*: zoom at low energy and at low quenching factor of the quenching factor distribution as a function of recoil energy for 93.5 kg·d total fiducial exposure. *Right side*: recoil energy spectrum of events in nuclear recoil band (E_R>30 keV) observed for a total fiducial exposure of 93 kg·d, compared with simulated WIMP spectra using a WIMP-nucleon cross section $\sigma_{\chi-n}$=10^{-5} pb for 20, 40, 100 and 500 GeV/c^2 WIMP mass.

4.2.2 Limits on the cross section for spin-independent WIMP-nucleon interactions

The three observed events can be used to obtain an upper limit on the scattering cross section of a WIMP on a nucleon as a function of WIMP mass for spin-independent interactions.

To evaluate an upper limit on the WIMP rate with these three events using the Yellin method (Sec. 1.4.2.3) we simulated the response of the detectors given the known resolutions, thresholds and fraction of the total 93.5 kg·d fiducial exposure. Simulations for WIMP masses of 20, 40, 100 and 500 GeV/c^2 are shown in the right side of Fig. 4.6.

As this method determines the energy interval that constrains the most the signal, this information provides some assistance in the interpretation of the observed spectrum. Lower and upper bounds of selected energy intervals are shown in Fig. 4.7 together with the number of events in corresponding interval.

Since the two first events occur with energy very close to the 30 keV recoil energy cut (30.2 and 30.4 keV) the Yellin interval for WIMP mass

below 30 GeV/c^2 will start from 30.4 keV and extend up to the last recorded event in nuclear recoil band at 41.8 keV, with no events observed. For WIMP mass above 30 GeV/c^2, the chosen energy interval is from 30.4 to 200 keV. The event at 41.8 keV populates this interval. Thus, for WIMP mass higher than 30 GeV/c^2 the best limit is obtained from 1 event in the energy range from 30.4 to 200 keV. The corresponding limit is shown in Fig. 4.8. This limit corresponds to a sensitivity of 5×10^{-7} pb at 80 GeV/c^2 WIMP mass, which is an improvement of a factor three with respect to EDELWEISS-I (1.5×10^{-6} pb at 80 GeV/c^2) [4].

To verify the Yellin limit, we compare it to different Poisson analysis. In Fig. 4.8, we observe that the Yellin limit above 30 GeV/c^2, based on the 41.8 keV event, is very similar to the Poisson limit based on 1 event and an analysis threshold of 31 keV. The Yellin limit is slightly worse because it takes into account the bias induced by having chosen a 31 keV threshold on the basis of the observed events at 30.2 and 30.4 keV. If we perform a Poisson analysis with the unbiased 30 keV threshold, all three events must be considered. This worsen the 90% C.L. limit at 80 GeV/c^2 from 5×10^{-7} to 8×10^{-7} pb, which is still below the EDELWEISS-I Yellin limit.

If we investigate in the nuclear recoil band the events lying below the 30 keV threshold, we notice that seems to be there much less events than observed in EDELWEISS-I in 62 kg·d. This brings the question of what would have happened if the threshold would have been chosen at 20 keV instead of 30 keV. It would be of course too late to make such a choice, since it is biased by our observations on the present data. In addition, performing a consistent 20 keV analysis would require a more careful evaluation of the detector thresholds. Furthermore, the entire selection must be redone with the constraint of this new magic point value. Only 8 of the 11 detectors have a magic point below 20 keV. Keeping this in mind, we can perform a rough analysis to test the consistency of the EDELWEISS-I and II results.

Accordingly, we accept the detectors GSA8 and GSA7 whose magic points are slightly above 20 keV, knowing that the ionization and heat quality cuts will make them lose a considerable amounts of kg·d.

Performing a 20 keV analysis with the chosen 10 detectors we obtain a fiducial exposure of 61 kg·d (Tab. A.11).

Fig. 4.9 shows how the efficiency curve as a function of recoil energy, calculated using the experimental resolutions and quality cuts for a WIMP mass of 100 GeV, changes between the 20 keV and 30 keV analysis. In both cases, we see that the efficiency plateau is reached at the desired recoil energy. In addition, Fig. 4.9 shows that the analysis could be extended down to a recoil energy of 17 keV (12 keV) for the 30 keV (20 keV) magic point selection, but this would require a more thorough investigation of the thresholds, and

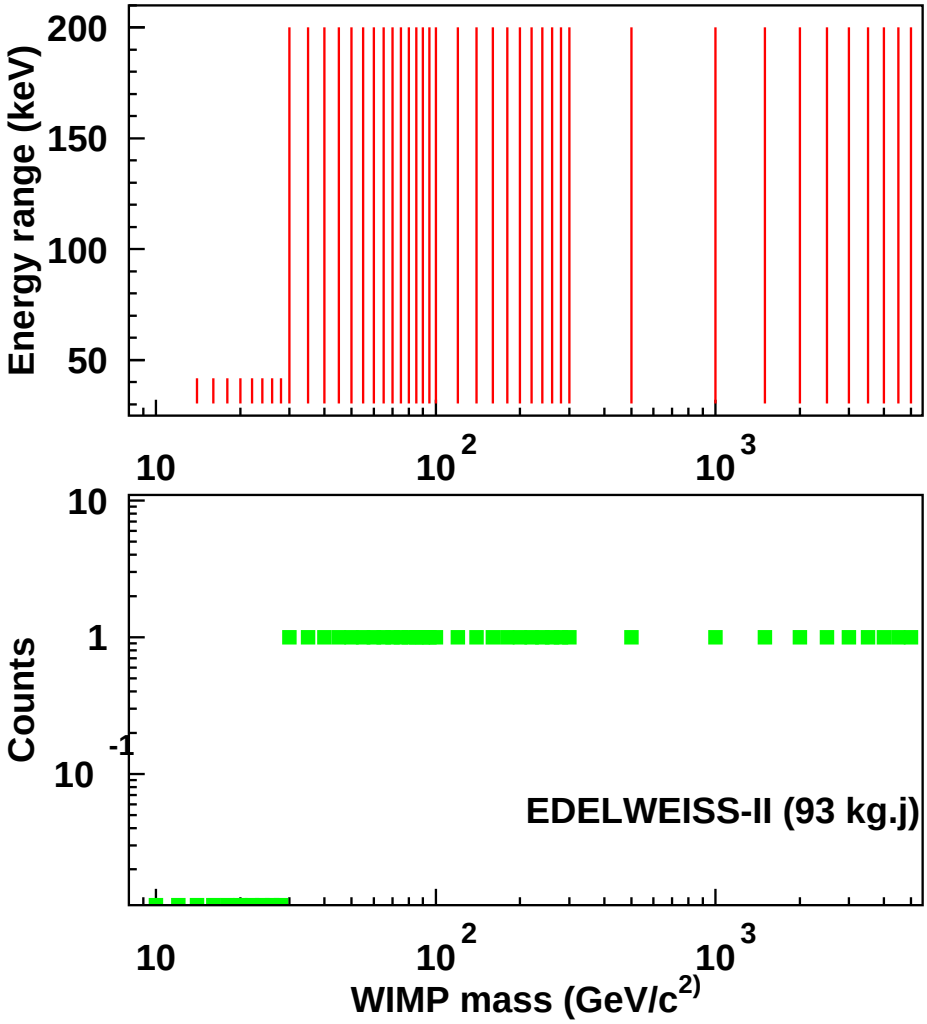

Figure 4.7: *Top*: recoil energy range selected by Yellin algorithm used to derive a 90% C.L. WIMP-nucleon cross-section upper limit as a function of WIMP mass. *Bottom*: number of events recorded in the corresponding recoil energy interval.

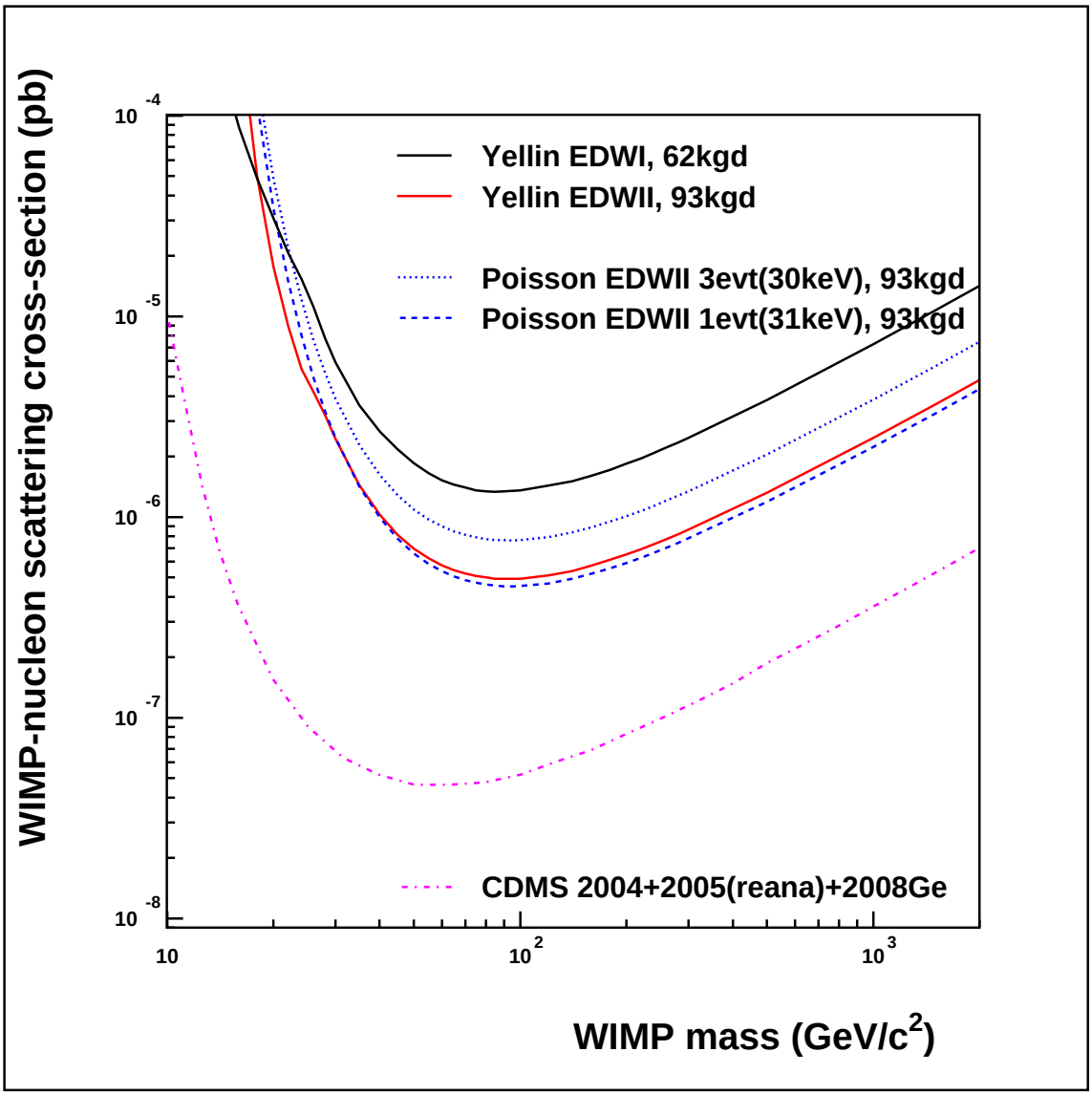

Figure 4.8: 90% C.L. spin-independent exclusion limits obtained for run 8 for a fiducial exposure of 93.5 kg·d using Yellin method (red solid curve) and using Poisson statistics (blue solid curve). Data set corresponds to 3 events recorded in the nuclear recoil band. EDELWEISS-I data [4] are also plotted (black solid curve) with CDMS current best sensitivity [74]. Dashed curve: run 8 data set with a 31 keV recoil threshold, with only one event recorded in the nuclear recoil band for Poisson statistics. This has been made to verify interval choice performed by Yellin method. In fact, it predicts a recoil energy range above 30.4 keV ith one event populating it.

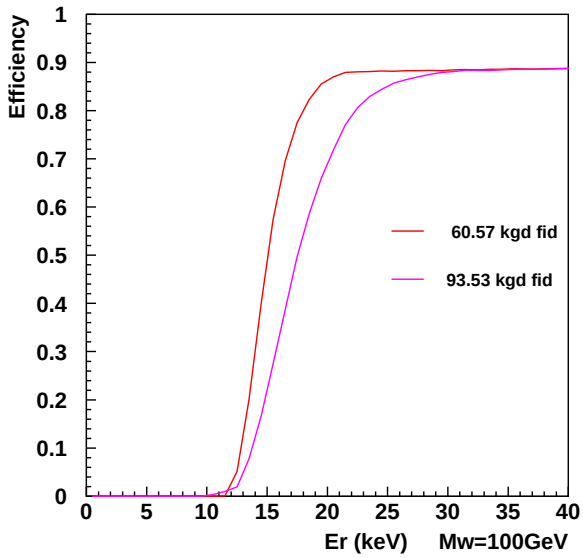

Figure 4.9: Simulated detection efficiency for run 8 for a 30 keV (93.5 kg·d) and a 20 keV (60.6 kg·d) magic point selection.

would probably not yield any improvements on the limits, because events are observed at energies as high as 31 keV.

Eight events are observed in the nuclear recoil band in the recoil energy range from 20 to 200 keV, meaning an event rate of 0.13±0.05 evts/kg·d, as shown in Fig. 4.10. The upper limits of this analysis are shown on the right side of Fig. 4.10.

This tighter selection cuts remove the candidates at 30.2 and 41.8 keV. However, the limit at high mass is not improved because of the reduction in exposure. This confirms that the 30 keV threshold was a reasonable choice.

The 20 keV analysis does not improve the 30 keV analysis limit for all WIMP masses above 20 GeV/c^2. It however improves on the EDELWEISS-I limit in the entire mass range, even at low masses where the result depends strongly on the population of events between 20 and 30 keV. This suggests that the backgrounds observed in EDELWEISS-I in this low energy range is reduced in EDELWEISS-II by a factor of the order of two.

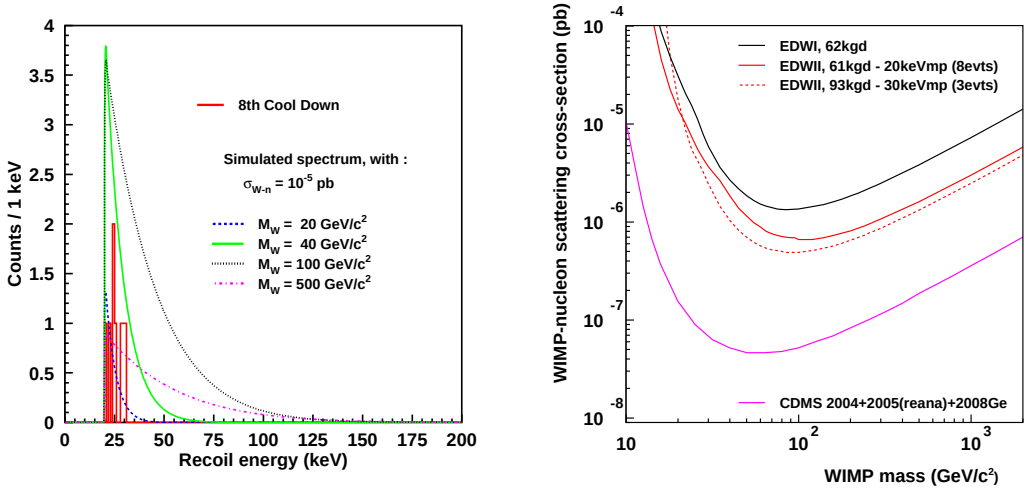

Figure 4.10: *Left Side*: Recoil energy spectrum of events in nuclear recoil band (E_R>20 keV) observed for a total fiducial exposure of 61 kg·d, compared with simulated WIMP spectra using a WIMP-nucleon cross section $\sigma_{\chi-n}$=10^{-5} pb for 20, 40, 100 and 500 GeV/c^2 WIMP mass. *Right Side*: Comparison between 90% C.L. spin-independent exclusion limits obtained for run 8 for a fiducial exposure of 93.5 kg·d with a 30 keV magic point selection (red solid curve) and for a fiducial exposure of 60.6 kg·d with a 20 keV magic point selection (red dashed curve). EDELWEISS-I data are also plotted (black solid curve) with CDMS current best sensitivity.

4.3 Background interpretation

In this section I will present our interpretation and understanding of different backgrounds in the EDELWEISS-II data set. These backgrounds are related to different origins: gamma rays radiation, alpha particle and other surface events. While the energy range of interest for WIMP search is limited below 200 keV, high energy gamma and alpha lines are very useful to understand background in the range relevant to WIMP interactions.

4.3.1 Gamma rays

More than 99.5% of the interaction rate in detectors is due to gamma events. The 20 cm thick lead shielding stops most of the gammas from outside the experimental setup, thus we expect that must of the observed gamma background should come from inside. First, the spectrum of high energy gamma

No	Name-Pos.	kg·d	counts	total γ rate
4	GGA14-c1	22.09	3790	171.6 ± 2.8
5	GGA13-d1	22.39	5293	236.4 ± 3.2
6	GSA11-b2	22.38	4035	180.3 ± 2.8
7	GGA10-c2	22.08	4279	193.8 ± 3.0
8	GGA7-d2	22.09	5113	231.5 ± 3.2
9	GSA10-b3	21.38	3976	186.0 ± 2.9
10	GGA3-d3	22.39	5670	253.2 ± 3.4
11	GGA5-c4	22.53	4105	182.2 ± 2.8
12	GGA11-d4	22.23	4643	208.9 ± 3.1
14	GGA8-c5	21.93	3652	166.5 ± 2.8
15	GSA8-d5	22.55	4387	194.5 ± 2.9
17	GGA4-c6	21.63	3632	167.9 ± 2.8
18	GGA9-d6	22.24	4679	210.4 ± 3.1
19	GSA7-b7	21.76	4742	217.9 ± 3.2

Table 4.7: Gamma background rates (total volume) in counts/kg·d.

rays with energy above 100 keV is studied in order to determine a global background. Afterwards, the low energy gamma spectrum is explored to give estimations of the expected event rate in the energy range of interest for WIMP detection.

4.3.1.1 High energy gamma rays

The total ionization spectrum for low background physics runs is shown in the left side of Fig. 4.11. We restrict our analysis to the ionization channel because of the non-linearity of the heat channel (β parameter in Eq. (3.3)), which is poorly calibrated above 500 keV. It will be shown later that the ionization channel is linear up to ∼2.6 MeV.

We observe a rate reduction of about a factor three relative to EDELWEISS-I [96]. Gamma background rates per detector for ionization energies above 100 keV without any quality baseline cut occurring in total volume are listed in Tab. 4.7. The baseline quality cuts are relaxed here because they are not relevant for γ-rays at energy higher than 100 keV. The right side of Fig. 4.11 shows the rates per detector as a function of the level occupied in the tower in the cryostat. We observe a little higher event rate for detectors placed in the top level of the towers, but the overall variations do not exceed ±20%.

We have verified that performing the 30 keV magic point and quality cut selections does not alter significantly these rates (Tab. A.14 to Tab. A.13).

These tables also show that the γ rates are constant in time.

The gamma background reduction relative to EDELWEISS-I appears global and uniform. The average integrated gamma count rate (100 keV - 3 MeV) is 200±3 counts/kg·d, for the detectors listed in Tab. 4.7 for a total exposure of about 310 kg·d (total volume, no quality cuts). The error is calculated from the maximum statistical error for each detector rate ($\Delta\epsilon$=1.7%)

Noticeable features in the gamma background spectrum are the Compton backscattering bump around 200 keV, the 2614 keV line from ^{208}Tl decay, originating from Th series, and the peaks coming from ^{40}K (1461 keV) and ^{60}Co (1173 keV and 1332 keV). Tab. 4.8 shows that the measured peak positions correspond to expectations, showing that non-linearity and saturation effects are small. We remind that this channel is calibrated using the 356 keV line only.

These well shaped high energy peaks allow us a verification of our assumed energy dependance of the resolutions. The σ resolution value found by fitting them is compatible with what we should obtain with the formula, see Eq. (3.5). The latter, considering average resolutions value, become: $\sigma_I^2 = (1.21) + \frac{5.04}{356^2} \cdot E^2$ and, for instance it gives for the ^{40}K line a prediction of about 9.2 keV compared to a measured value of 8.2±1.3 keV. Fitted values are shown in Fig. 4.12 with also a fit of σ^2 as a function of E_I^2.

Monte Carlo simulations with GEANT4 [113] have been carried out in order to better understand experimental gamma background spectrum. Several sources of gamma background were successively studied and compared with the observed spectrum. The most massive materials in the vicinity of detectors are detector holders, cryostat structure and thermal shields. This "nearby copper" amount tof about 500 kg of copper. The upper limit on their U/Th content has been estimated to an activity of 1.2 mBq/kg [1]. Copper holders have been brought in the underground site only few months before experiment starting. It means that the cosmogenic activity of ^{60}Co at the surface has to be considered. The experimental limit on ^{60}Co is compatible with a concentration $<$ 1 mBq/kg. U/Th and ^{60}Co contributions for each copper structure used as source of gamma background and assuming activities equal to their upper limit, are compared to the observed spectrum in Fig. 4.13.

Since we have used upper limits, it is expected that the simulated ionization spectrum, due to the sum of ^{60}Co and U/Th contaminations, should be higher than the observed one.

[1] Measurements carried out within the EDELWEISS collaboration with the GENTIANE low background HPGe γ spectrometer in the underground laboratory site (LSM)

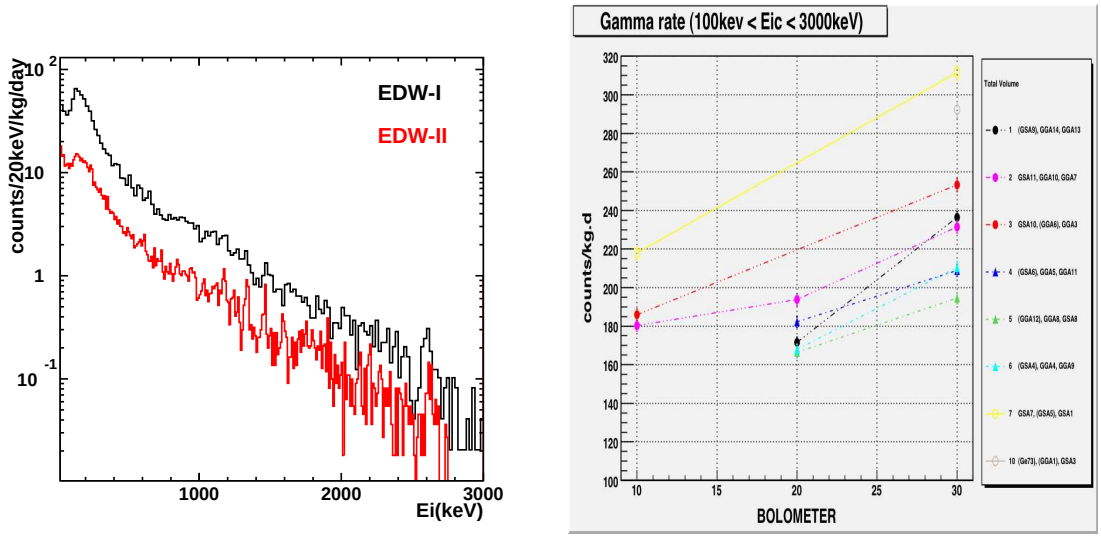

Figure 4.11: *Left side*: gamma background energy spectrum (total ionization channel). *Right side*: gamma background rate per detector as a function of position occupied in the tower in the cryostat. "10" means bottom level, "20" middle level and "30" top level.

In order to give a more reliable estimation of the ^{60}Co activity, we use the counting rate measured in the ^{60}Co peaks as predicted by the present simulation of the nearby copper. Normalizing simulated ^{60}Co peaks to the number of counts experimentally found we derive the activity of 0.2 mBq/kg for the nearby copper (counting rates in Tab. 4.8 in agreement with a normalization factor of about 0.23) with a systematic error of the order of 10%. Thus, all the contributions of the simulated ^{60}Co contamination on Fig. 4.13 should decrease of a factor 0.23, showing that most of the gamma background is likely to come from U/Th chain, as shown in Fig. 4.14.

Focusing, this time, on the red spectrum of Fig. 4.14 due to U/Th pollution, we have to notice two unexpected features: a first one linked to simulated peaks higher than the observed one, see for instance ^{208}Tl(2615 keV) peak, and the second one a bigger Compton backscattering than the expected one. Assuming, in first approximation, that U and Th chains have the same activities (same measured upper limits), we can try to perform the same counting rate normalization carried out for ^{60}Co peaks. Hence, studying Tl peak at 2615 keV for experimental data and simulation gives a normalization factor leading to a decreasing of about a factor 3 (counting rates reported in Tab. 4.8) , that means U/Th contamination of about 0.4 mBq/kg (always considering that U and Th contaminations are equal.)

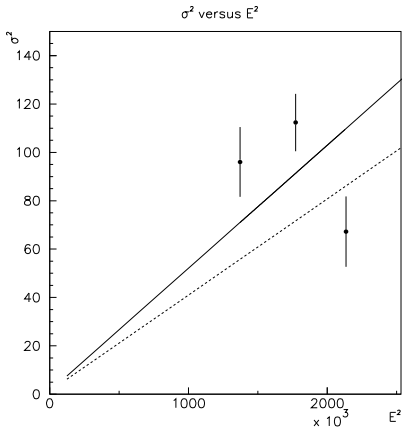

Figure 4.12: Experimental values of σ^2 (got studying the "couts/3keV" spectrum) as a function of E^2 for ^{40}K and ^{60}Co peaks respectively corresponding to the coordinates (E,σ): (1461.3±1.4, 8.2±1.3), (1171.31±1.1, 9.8±1.6), (1331.2±1.3, 10.6±1.1). The fitting function is a first oder polynomial one: $y = a + bx$. The a parameter has been set equal to the squared σ experimental baseline value. It is compatible with our extrapolation using a 356 keV calibration (dashed line).

Therefore, the final comparison between data and Monte Carlo simulation is shown in Fig. 4.15. We explain the observed peaks due to ^{60}Co activation and U/Th contamination with activities of about 0.2 mBq/kg for ^{60}Co and about 0.4 mBq/kg related to U/Th decay chain in the nearby copper mass. Thus, we can hypothesize that the spectrum we have to add to obtain a good agreement between data (dark line in Fig. 4.15) and simulation (pink line in Fig. 4.15) is due to contaminant in of other materials. The absence of peaks suggest that it originates from material far from the detectors. Indeed, the missing spectrum seems to have the same shape of the U/Th chain pollution.

We can also estimate the contribution of ^{40}K. The experimental rate of the ^{40}K peak at 1460 keV is 1.8±0.2 counts/3keV/kg·d, comparable to the ^{60}Co peaks. The contribution of the Compton plateau associated to the ^{40}K peak should have a shape similar to the ^{60}Co one. In particular, its Compton edge at ∼1.2 MeV should fill the difference in shape observed in Fig. 4.15 between the experimental data and summed simulations.

An investigation has been carried out about the experimental ^{40}K peak, checking if this contamination comes from a peculiar place. We have divided detectors into three categories according to where they are located in the tower into the cryostat. The ^{40}K peak count rates for detectors on the

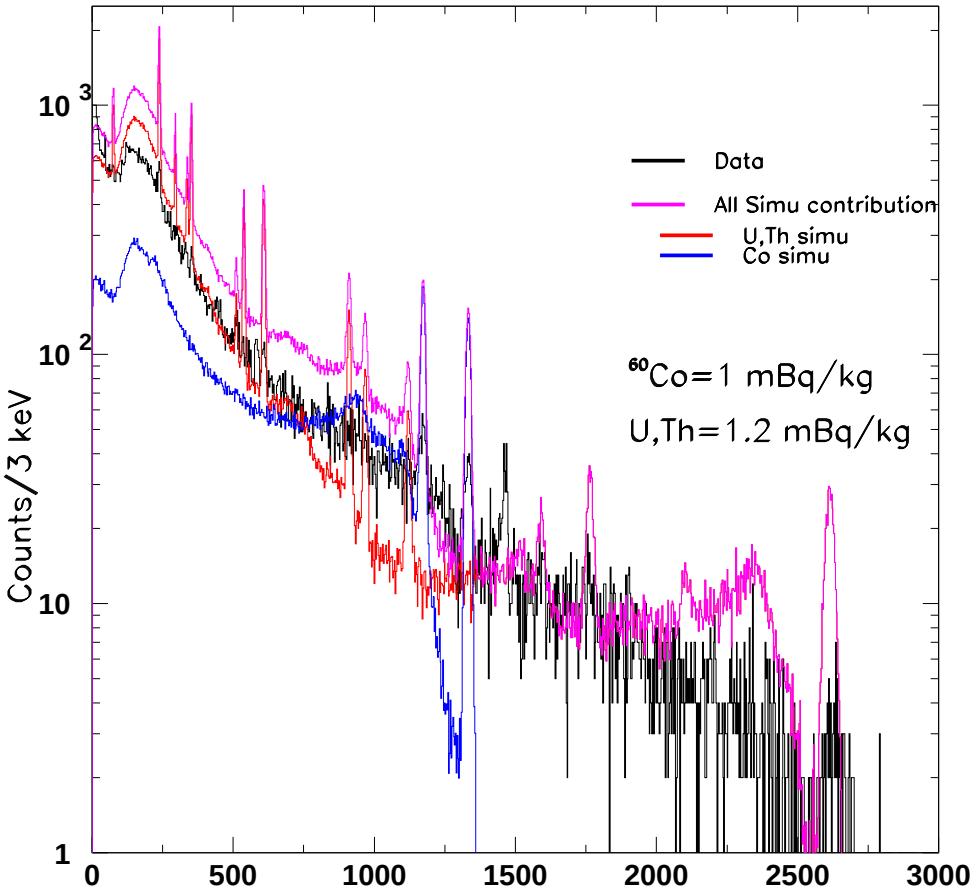

Figure 4.13: Gamma background energy spectrum (total ionization channel) without any quality cut corresponding to a total exposure of about 310 kg·d compared to Monte Carlo simulations of possible U/Th and ^{60}Co contaminations in the copper of detector holders, cryostat structure and thermal shields. Blue line represents ^{60}Co contribution to gamma background and red line U/Th one. Sum of run 8 data set is dark line and the pink one is the sum of all simulation of U/Th and ^{60}Co.

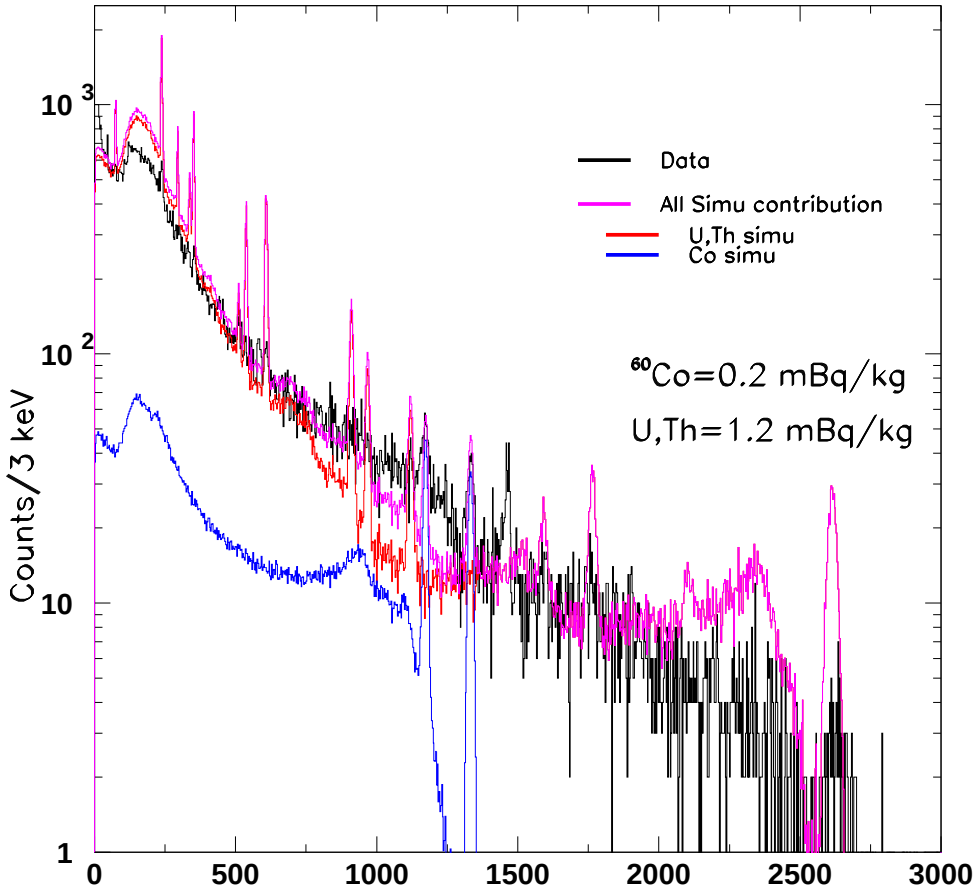

Figure 4.14: Gamma background energy spectrum (total ionization channel) without any quality cut corresponding to a total exposure of about 310 kg·d compared to Monte Carlo simulations of possible U/Th and ^{60}Co contaminations. Blue line represents ^{60}Co contribution to gamma background normalized on experimental peaks counting rate: it means considering a 0.2 mBq/kg ^{60}Co contamination. The red line U/Th contamination linked to upper limit of 1.2 mBq/kg activity. ^{60}Co contributions are normalized on experimental peak counting rates. Sum of run 8 data set is dark line and the pink one is the sum of all simulation of U/Th and ^{60}Co.

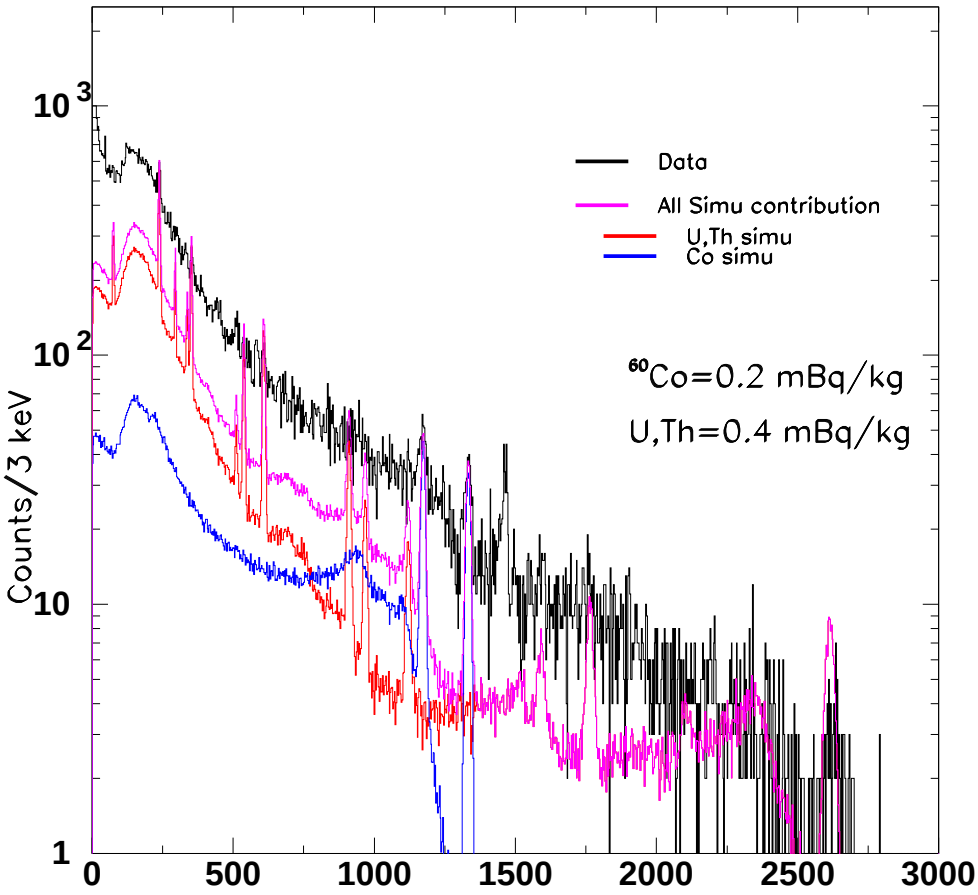

Figure 4.15: Gamma background energy spectrum (total ionization channel) without any quality cut corresponding to a total exposure of about 310 kg·d compared to Monte Carlo simulations of possible U/Th and ^{60}Co contamination. Blue line represents ^{60}Co contribution to gamma background and red line U/Th one. Both contributions are normalized on experimental peak counting rates. For U/Th contamination, the normalization is done using the 2615 keV gamma line from ^{208}Tl. Sum of run 8 data set is dark line and the pink one is the sum of all simulation of U/Th and ^{60}Co.

	E_{theo} (keV)	E_{exp} (keV)	counts/3keV (310kg·d)	
			data	simulation
^{60}Co	1173	1171.7±1.1	612±69	2979±15
	1332	1331.2±1.3	720±86	2896±11
^{298}Tl	2615	2627.9±10.8	331±60	1135±11

Table 4.8: Theoretical and experimental peak positions for the ^{60}Co and ^{208}Tl. Peak counting rate from low background physics data and simulation for the ^{60}Co and ^{208}Tl for an activity of 1 mBq/kg and 1.2 mBq/kg respectively. The total exposure is of about 310 kg·d.

bottom, middle and top plates are equal to 1.4± 0.3, 2.0± 0.3 and 1.7± 0.2 counts/3keV/kg·d respectively. Thus, no specific origin seems to be preferred. In the measurements performed while screening all the material entering the nearest elements in the cryostat, the highest ^{40}K activity was measured in the connecting cables in the detector, but since the involved mass is very low the simulated rate does not explain the experimental ^{40}K rate.

Simulations are under study to help locate the main source of this contaminant. Up to now, the first results are that the observed peak intensity correspond to a total activity of 5.7 Bq outside the thermal shields of the cryostat, or 0.3 Bq for a contamination lying closer to the detectors (10 mK shield).

4.3.1.2 Low energy gamma rays

In the energy range of interest for WIMP search, (typically the energy range from 15 to 65 keV), we want to estimate how many events recorded in the gamma band could leak into the nuclear recoil band. Thus, we have to focus on fiducial volume, since an event is seen as a WIMP candidate if it takes place in the fiducial volume.

Cosmogenics The present resolutions of the detectors do not allow to separate the contribution of the lines of cosmogenic isotopes ^{68}Ge and ^{65}Zn. As shown in Fig. 4.16, we observe a peak centered at about 10 keV. This peak is due to the contributions of ^{68}Ge (10.4 keV) and ^{65}Zn (9.0 keV) isotopes resulting from bombardment of the Ge detector by cosmic rays when it was above ground. These isotopes have an half-life decay of 244 d and 271 d respectively.

No	Name	rate (counts/kg·d) fit 1	fit 2
4	GGA14	4.11±0.86	4.97±0.87
5	GGA13	3.37±0.73	3.27±0.67
7	GGA10	5.44±0.84	5.48±0.84
9	GSA10	4.38±1.14	4.54±0.86
10	GGA13	10.70±1.21	11.23±1.00
11	GGA5	3.78±0.92	8.2±1.74
17	GGA4	2.91±0.77	7.20±1.14
18	GGA9	3.22±0.73	3.44±0.74

Table 4.9: Counting rate values obtained for the cosmogenic 10 keV peak. Two fits are performed: "fit 1" it means E_{max}=20 keV with number of channel equal to 80 and "fit 2" is related to a E_{max}=50 keV with 100 channel.

The energy spectrum in Fig. 4.16 is a combination of ionization and heat energy weighted on their baseline resolutions. Fiducial volume has been selected and baseline quality cuts performed. Detectors showing problems such as charge collection (GSA11) and unexplainable heat gain jumps (GGA11 and GSA1) are not retained for this analysis. In addition GSA8, loosing most of its exposure by quality cuts, shows a too poor statistics for the 10 keV peak. Since statistics are low, two fits have been carried out in order to estimate the peak intensity. They differ in terms of upper energy bound and number of channels. Values obtained are listed in Tab. 4.9. Two detectors, GGA5 and GGA4, have inconsistent fit values and are therefore excluded. In addition, GGA3 shows a significantly larger 10 keV counting rate. A likely explanation is that it has been remained outside the underground laboratory, at the sea level, longer than the others. The full history of all detectors is being investigated. For the other detectors we obtain an average counting rate of 3.6±0.4 counts/kg·d for the fiducial volume performing quality cuts and 3.4±0.3 counts/kg·d adding coincidence cuts (single events required). These two results are consistent. Measurements carried out in 2003 (detectors in underground laboratory LSM for two years) show a rate of 14±3 counts/kg·d. Compared to current results a reduction of about a factor 4±1 is obtained. As expected, the long-term storage of detectors in underground sites reduces the 10 keV peak due to cosmogenics.

Leakage of gammas in nuclear recoil band In energy range between 15 and 65 keV the fiducial integrated count rate is about 0.376±0.008 counts/keV/kg·d with quality cuts performed, and if we add coincidence cut (considering only

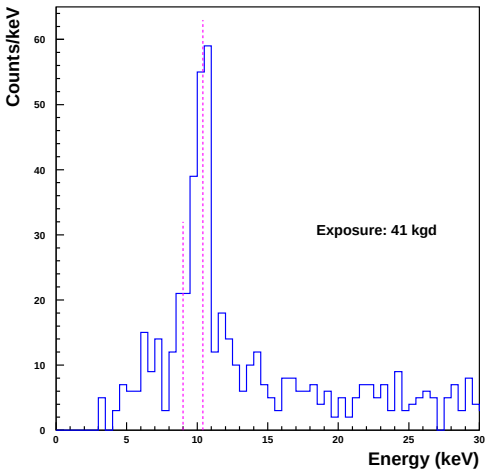

Figure 4.16: Energy spectrum for four of the detectors (GGA14, GGA13, GGA10 and GSA10) used in the 10 keV analysis.

single events) the result is 0.328±0.008 counts/keV/kg·d. This rate is a factor three less than the EDELWEISS-I rate of 0.98±0.03 counts/keV/kg·d [4].

We can estimate the probability that these low energy γ, normally collected with a quenching factor of one, fall in the nuclear recoil band. We used a simple model assuming gaussian distribution of events in the electronic recoil band to calculate the rate inside the 90% acceptance nuclear recoil band at a given recoil energy E, for 5 keV recoil energy intervals, from 10 to 30 keV. The recoil energy intervals are considered as perpendicular strips in the (E_R, Q) plane. Thus, tabulating for each E value at how many sigmas the electronic recoil band overlaps the nuclear one, it is possible to know the percentage of leakage to consider, always assuming gaussian data distribution. Only downward leakage will be taken into account to find how many counts per keV and per kg·d are expected in the nuclear recoil band.

For recoil energy from 10 keV up to 30 keV we expect to observe in the nuclear recoil band about 0.2 counts/kg·d coming from a low energy continuum gamma background plus about 0.3 counts/kg·d due to cosmogenics. For a recoil energy in the 20-30 keV range the expected rate is about 0.008/0.01 counts/kg·d, that means less than 1 event in the nuclear recoil band for an exposure of 100 kg·d. Thus, with the lower recoil energy bound at 30 keV used here, no γ for electronic recoil band is expected to settle nuclear recoil band.

Thus our WIMP search results based on 93.5 kg·d with a 30 keV analysis

threshold should not be affected by the leakage of photons into the nuclear recoil band. In the future, with the goal of using analysis threshold below 20 keV, it will be necessary to reduce this leakage effect. This should be achieved with an improvement of the energy resoultions relative to the present values achieved here (on average FWHM, 1.7 keV for ionization and 1.8 keV for heat).

CONTINUUM

E_R	N_σ	downward leakage (%) (assuming gaussian)	counts/kg·d ($\times 10^{-2}$)	
			all	cut
10	1.45	8	15.0	13.1
15	2.4	0.8	1.5	1.3
20	3.29	0.5	0.9	0.8
25	4.1	$2.05 \cdot 10^{-3}$	$3.9 \cdot 10^{-3}$	$3.4 \cdot 10^{-3}$
30	4.9	$3.7 \cdot 10^{-5}$	$7.0 \cdot 10^{-5}$	$6.1 \cdot 10^{-5}$
Tot			17.5	15.3

10 keV peak

E_R	N_σ	downward leakage (%) (assuming gaussian)	counts/kg·d	
			all	cut
10	1.45	8	0.29	0.27

Table 4.10: Gamma leakage in energy strip with central value E_R and dispersion ± 5 keV, for a continuum low gamma background and for the cosmogenic 10 keV peak.

4.3.2 Alpha and beta backgrounds

In EDELWEISS-I we identified beta and alpha from ^{210}Pb surface contamination as a source of background [96]. It is due to an exposition of germanium crystals to air with ^{222}Rn and to implantation of its long-lived (22 years) ^{210}Pb daughter on the Cu and Ge surfaces, despite the care taken in the storage of detectors and using a flux of deradonized air at their installation in the cryostat.

This isotope decay to ^{210}Bi, emitting X-rays conversion electrons with energies below 60 keV falling precisely within the energy range of interest for WIMP searches. ^{210}Bi decays to ^{210}Po with emission of a beta with an end-point at $\sim$1.1 MeV. Finally, ^{210}Po decays to ^{210}Pb via a 5.3 MeV alpha

with a range of 20 μm, accompanied back-to-back by the recoil of the ^{210}Pb nucleus ($\sim$40 nm) with a kinetic energy of 103 keV. The penetration length of such a heavy particle at such low energy is very small ($\sim$40 nm). All the ionization signal is lost: charges are absorbed either in the Al electrode or in the amorphous sub-layer if the lead nucleus hits a surface not covered by an electrode. Of all the decays in the complete chain, the alpha observation is the clearest tag.

When the equilibrium of the ^{210}Pb decay chain is reached, the rates for alphas, ^{206}Pb nuclear recoil, high energy betas and low energy electrons are expected to be equal.

4.3.2.1 Response of EDELWEISS detector to a ^{210}Po source

In EDELWEISS-II , we wanted to study the response of our detectors to this background by equipping the detector GGA1 with a ^{210}Pb source.

The source was made by our CEA collaborators, with the main concern that it should not contaminate the rest of the experiment. It was done by exposing a Cu plate to ^{222}Rn gas coming out of a ^{238}U sample. The three alpha decays between ^{222}Rn and ^{210}Pb make the nuclear recoils to be implanted deeper and deeper in the copper surface. After exposition, the plate is heated to get rid of the remaining ^{222}Rn and shallowly implanted ions, and cleaned thoroughly to make sure than radioactive atoms that could easily get out of the Cu are removed. The implanted Cu plate is a 5 cm disk, glued on the center of the Cu cover in front of the reference-electrode side of GGA1. Most of the alpha flux should be detected in the centre region.

The present study corresponds to the analysis of data recorded at $\pm$7 V. We use data collected in the fiducial volume after quality cut on baseline resolutions. The recorded spectra for the +7V data is shown in Fig. 4.17: we observe the alpha peak at 5.3 MeV and Q=0.4. It unambiguously confirms the interpretation [96] that the observed quenched peak at high recoil energy in EDELWEISS-I comes from a surface alpha contamination.

However, it was observed that the quenching value of alphas is not constant: it depends on the polarity of the detector and it evolves with time. Figure 4.18 shows the average quenching factor of the alpha population (Q_{alpha}) as a function of time. The top panel is the data recorded at -7 V and the bottom panel is at +7 V bias voltage. These variations was not seen in EDELWEISS-I. In ref. [103], it is shown that Q_{alpha} depends on the amount of trapped charge accumulated on the surface of Ge. Here the evolution of Q_{alpha} at -7V could be due to the large flux of alpha (compared to the flux in low-background runs in EDELWEISS-I). The fact that it does not evolve in data taken with +7V polarization is an indication that electrons and holes do

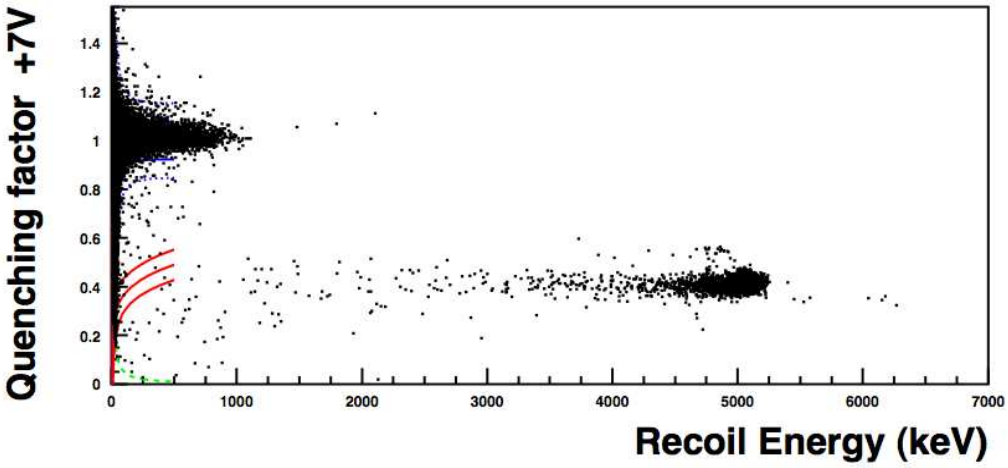

Figure 4.17: Distribution of the quenching factor as a function of the recoil energy up to 8 MeV from the data collected in the fiducial volume at +7 V in GGA1 detector.

not have the same trapping probability by the defects created by the intense alpha source.

To measure the alpha rate, we count what is in a wide box defined by a quenching factor in the range 0.01-0.6 and a recoil energy lying from 3 to 7 MeV. This box is wide to make sure we do not depend on the charge state of the detectors. In addition, the fiducial volume selection is a loose cut (75% of the total charge must be collected on the center electrode) because cross-talks and energy resolutions are not calibrated very precisely for these very high energies.

The alpha rate in GGA1 in the fiducial volume is 9085±27 counts/kg·d for the whole statistics.

Voltage condition	counts		
	α	β	$\beta_{nuclearband}$
-7V	15471	3507	442
+7V	5005	835	89

Table 4.11: Number of alphas, betas and betas restricted to the nuclear recoil band, for data recorded at ± 7 V in GGA1 detector after baseline quality cut.

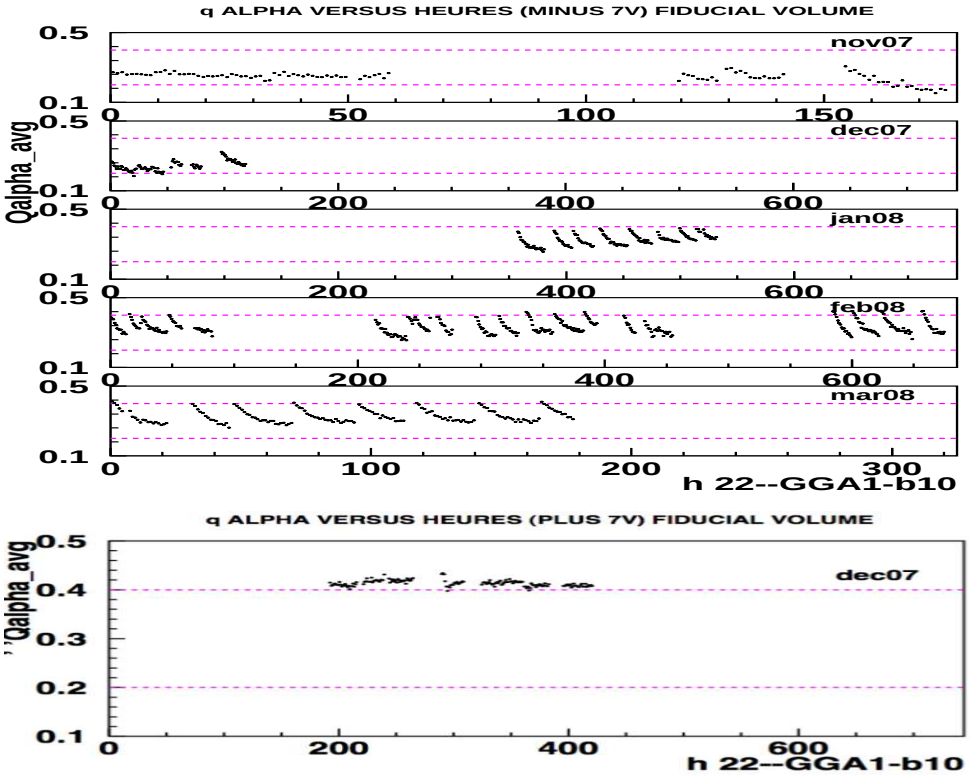

Figure 4.18: Alpha quenching factor as a function of time for data recorded in GGA1 detector. *Top*: data recorded at -7 V. *Bottom*: data recorded at +7 V.

Finally, in Fig. 4.19 we see the betas at lower energy. We notice that for the high-energy betas coming from ^{210}Bi (above 60 keV), the ionization quenching factor is affected by the change of polarity. The charge collection is the poorest for the -7V data, as for the alphas. Instead, the low-energy betas, for energies below 60 keV, leak into the nuclear recoil band for both $\pm$7V data. Therefore, it represents a very important feature for WIMP searches.

In order to evaluate low energy beta population we define a β selection box: 30 keV$<$E$_R$ $<$80 keV and 0.2$<$Q$<$0.7. This box does not contain all beta's, but it has been chosen to have as little gamma contamination as possible. Afterwards, we define also a $\beta_{nuclearband}$ box (β box restricted to nuclear recoil band) to evaluate the beta fraction that leaks in the nuclear recoil band.

Table 4.11 shows beta counts recorded in β and $\beta_{nuclearband}$ boxes. An

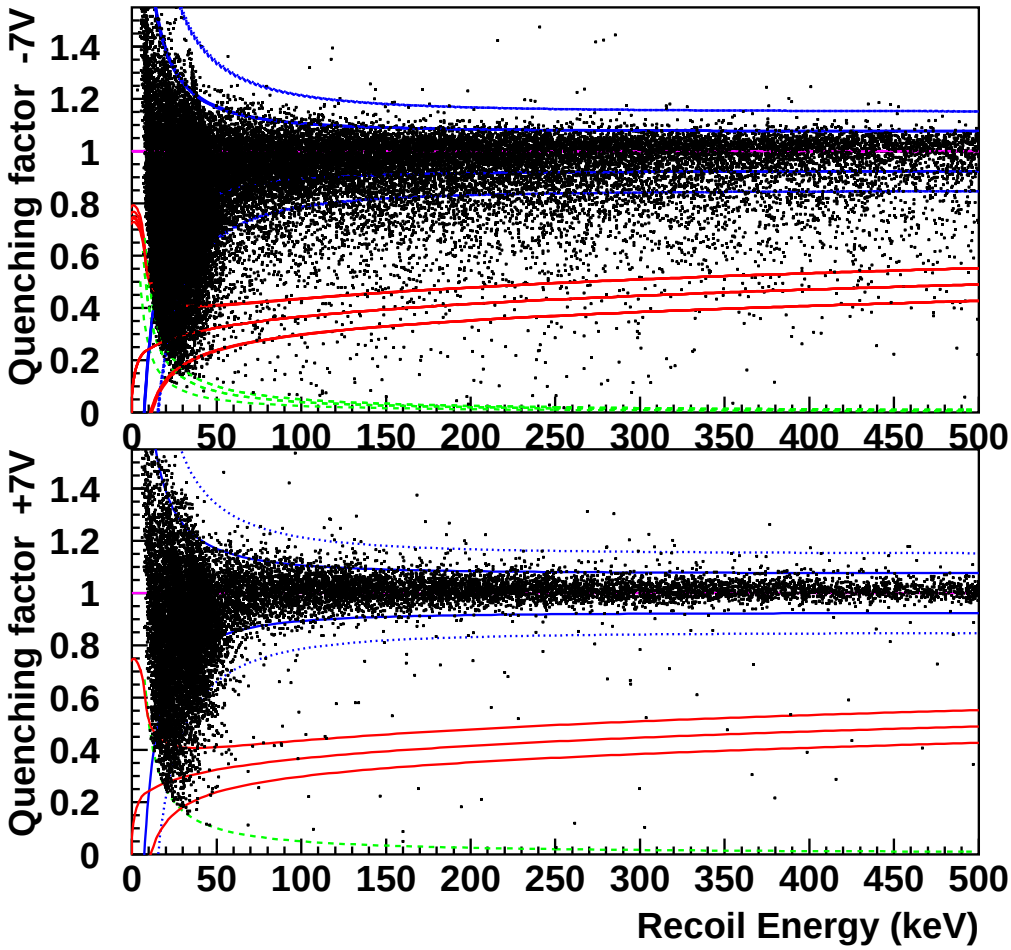

Figure 4.19: Distribution of the quenching factor as a function of the recoil energy for the data collected in the center fiducial volume. Data collected at -7 V (top) and data collected at +7 V (bottom).

interesting ratio is represented by β/α and $\beta_{nuclearband}/\alpha$. It should be corrected for the fact that the alpha emitter ^{210}Po is not yet in equilibrium with ^{210}Pb. For a ^{210}Pb source in equilibrium, these ratios should be decreased by a factor $\sim$30%. Table 4.12 shows these ratios (number of betas recorded in the two β boxes normalized to number of alphas) for the entire data set.

For the whole beta box, ratios of 0.167$\pm$0.007 and 0.227$\pm$0.005 are obtained respectively for +7 V and -7 V. In the β box restricted to nuclear

Ratio	Voltage		$<Q_\alpha>$
	-7V	+7V	(0.35 - 0.45)
β/α	0.227±0.005	0.167±0.007	0.20± 0.05
$\beta_{nuclearband}/\alpha$	0.029±0.002	0.018±0.002	0.024± 0.009

Table 4.12: Normalization factor of the beta population to the alpha one for GGA1 detector.

recoil band we get smaller ratios (0.029±0.002 and 0.018±0.002 for +7 V and -7 V). The values at +7 and -7V are not consistent, because of the effect of the accumulated charge on the surface of the detectors.

We need to estimate how the β/α and $\beta_{nuclearband}/\alpha$ ratios are affected by the accumulated charge on the surface, because the ^{210}Pb contamination in real experiments is very small, and not deposit as much charge as in the calibration data.

The idea is to investigate these two ratios as a function of measured alpha quenching factor (Q_{alpha}). Results are shown in Fig. 4.20. The number of betas in the box normalized to the number of alphas increases as Q_{alpha} is reduced due to accumulated charges. Beta over alpha ratios for -7V data at large Q_{alpha} (it means small accumulated charge) are consistent with ratios +7V.

At large Q_{alpha}, the number of beta normalized to the number of alpha in the β box tends toward 0.15. We have less statistics for the number of beta normalized to the number of alpha in the β box restricted to the nuclear recoil band ($\beta_{nuclearband}$), but we observe a consistent trend. The last column of Tab. 4.11 shows the ratio β/α, for the whole β box and for the one restricted to the nuclear recoil band, coming from extrapolation of plot in Fig. 4.20 at the alpha Q value observed in low background physics run (0.40±0.05). This number and its uncertainty is in agreement with both the measurements carried out at ±7V.

These fractions could allow to predict the number of low energy betas, as a function of the observed rate of the alpha from ^{210}Po decay, in detectors used for WIMP search. This prediction strongly depends on the knowledge of the quality of charge collection for surface events. Since it is difficult to assess, we will use the ratios obtained for the measured average Q_{alpha} value in low background physics.

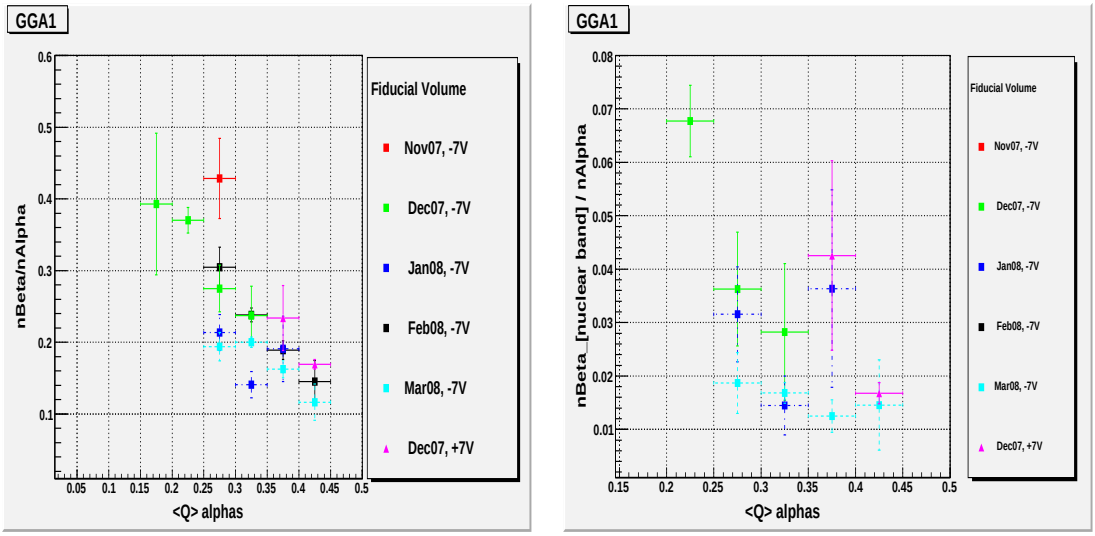

Figure 4.20: *Left side*: ratio of the number of betas recorded in the β selection box (30 keV<E_R <80 keV) to the number of alpha recorded in the selection α box (3 MeV<E_R<7 MeV) as a function of alpha quenching factor. *Right side*: ratio of the number of betas recorded in the β selection box (30 keV<E_R <80 keV) restricted to nuclear recoil band to the number of alpha recorded in the selection α box (3 MeV<E_R<7 MeV) as a function of alpha quenching factor. Data recorded at ±7 V for GGA1 detector.

4.3.2.2 Measured alpha background

Fig. 4.21 show the data recorded by 10 detectors and about 114 kg·d with the same fiducial cut as for GGA1 without any quality cuts. We observe the alpha population set at around 5 MeV. Their average quenching factor value is 0.40+-0.05. The absence of one sharp peak in quenching factor and and recoil energy distributions is due to uncertainties in high-energy calibration and saturation effects.

The same wide alpha box defined for GGA1 should work here for integrating the alpha rate (3 MeV<E_R <7 MeV and 0.01<Q<0.6). In Appendix Tab. A.17 lists the alpha rates counted in the fiducial volume without any quality cuts. The average rate is 2.0±0.1 alpha/kg·d, observed in fiducial volume. This is a reduction of a factor 2 with regard to EDELWEISS-I [96].

We can also study the dependence of this rate on the type of surfaces surrounding the detector. Four possibilities are available: 2 Cu covers, 2 Si covers, no cover (the Ge surface is exposed to the Ge surface of the neighbouring detector) or one Cu cover, the other Ge surface being exposed to

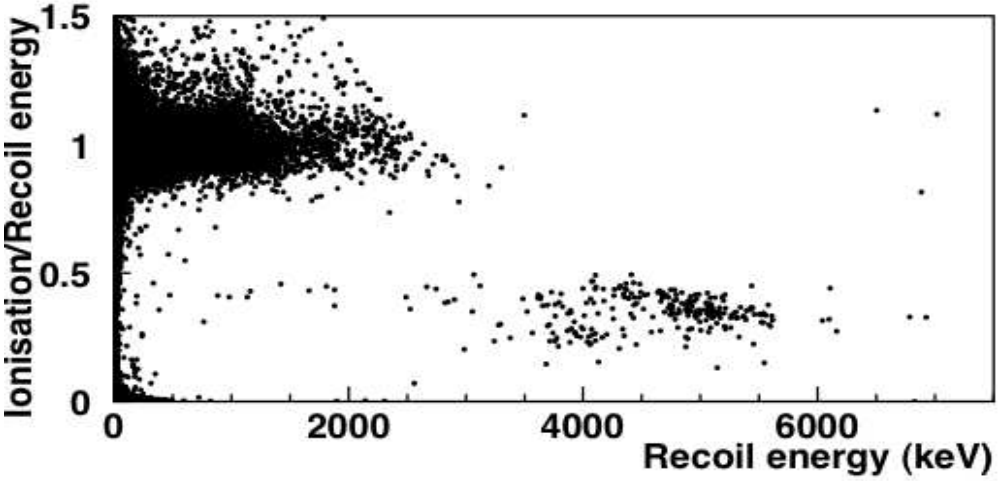

Figure 4.21: Distribution of the quenching factor as a function of the recoil energy up to 8 MeV from the data collected in the fiducial volume during low background physics runs.

the neighbouring detector. Fig. 4.22 shows the alpha rate as a function of cover type: no dependence within statistical accuracy is observed. Thus, this suggests that all type of surfaces have a comparable radon contamination.

In order to evaluate the contamination of the Ge surface themselves, we look at ^{206}Pb nuclear recoil in coincidence with an alpha event between two neighboring detectors without covers (GGA11 and GGA5).

We take all alpha events recorded in GGA11 and GGA5 detectors (top panel in Fig. 4.23). Then, for each detector we look for a 103 keV ionization-less ^{206}Pb nuclear recoil recorded in coincidence in the other detector (bottom panel in Fig. 4.23).

We observe 5 ionization-less events with recoil energy of about 103 keV, corresponding to a rate of 0.19+-0.09 coinc/kg·d. This is small (6%) compared to the total alpha rate of 3.2+-0.4 alpha/kg·d recorded in the sum of the fiducial area of the two detectors. This suggest that most of the alpha rate is due to Cu surfaces, but that is not consistent with the previous observation that the rate does not depend on the material of the surfaces (Cu/Si/Ge). An other explanation is related to the implantation depth of ^{210}Po emitters. If most of them are deeply implanted in Ge, they cannot escape. But this is not consistent with the observation of no recoils with energies below 65 keV as the energy of the ^{206}Pb recoils should degrade with implantation depth. Random fluctuations of the pollution levels from one

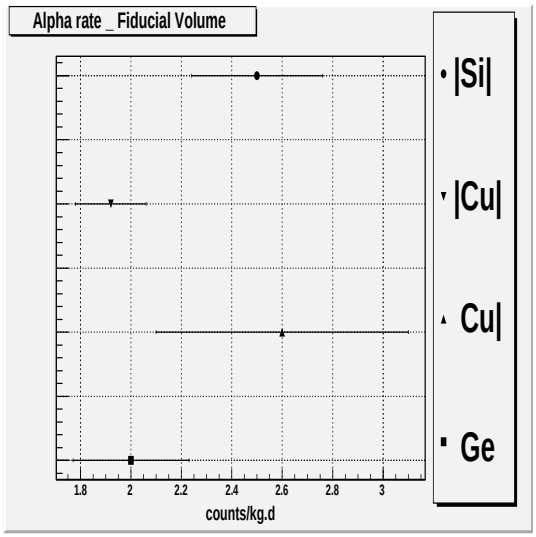

Figure 4.22: Average rate of alphas based on cover categories for low background runs (fiducial volume). |Si|: two silicium covers; |Cu|: two copper covers; Cu|: one copper cover and one free germanium surface; Ge: two free germanium surfaces.

surface to the other could explain these inconsistencies. However, the observation of these coincidences can only be explained if there is some level of ^{210}Pb contamination on the Ge detector surfaces themselves.

4.3.2.3 Prediction of beta leakage in the nuclear recoil band

The GGA1 data can be used to predict a rate of beta leakage in the nuclear recoil band associated with the observed alpha rate in detectors used for the WIMP search, if we assume that the background sources are in equilibrium.

To check the validity of the prediction for beta recorded in the β box restricted to the nuclear recoil band, we will also compare the predictions and the data in the larger β box.

We use the measured alpha rate (2.0±0.1 alpha/kg·d) and the observed quenching value (0.40±0.05) in the low background physics runs. Then, we use the number of betas normalized to the number of alphas in the β and $\beta_{nuclearband}$ boxes measured for a quenching factor in the range of 0.40±0.05 (from Tab. 4.12 in the last column we get 0.20±0.05 and 0.024±0.09 for β and $\beta_{nuclearband}$ boxes, respectively).

As shown in Tab. 4.13 we predict 0.048±0.018 beta/kg·d in the nuclear recoil band. Considering our experimental exposure of 93.5kg·d, it corre-

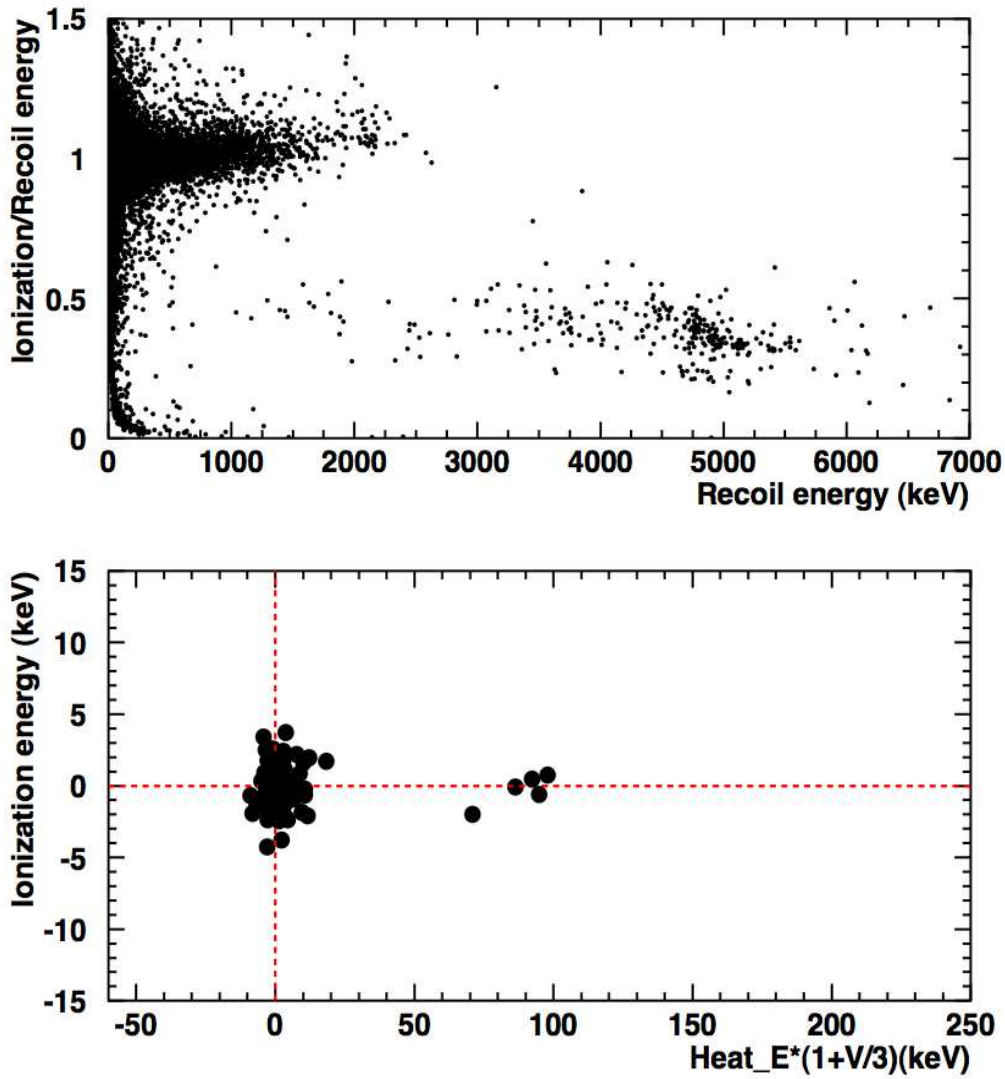

Figure 4.23: *Top pannel*: Distribution of the quenching factor (ratio of the ionization signal to the recoil energy) as a function of the recoil energy from the data collected in the fiducial volume during low background physics run, for data recorded in GGA5 and GGA11 detectors. These detectors are the only ones without any cover, allowing a coincidence study. *Bottom pannel*: Recorded ^{210}Pb recoils in coincidences with an alpha particle, in GGA5 and GGA11 detectors.

Zone	Data	Predicted
β	0.60±0.08	0.4±0.1
$\beta_{nuclearband}$	0.03±0.02	0.048±0.018

Table 4.13: Predicted (at ± 7 V) and observed counting rate in two different control zones: β box and β box restricted to nuclear recoil band for GGA1.

sponds to an expected background of 5±2 events in the nuclear recoil band between 30 and 80 keV. We observed 3 events in the same region.

In order to check reliability of this calculation we widen the investigation zone to the whole β box. We obtain the number of betas predicted equal to 0.40±0.10 beta/kg·d to be compared to the measured value of 0.60±0.08 beta/kg·d. It shows an agreement at 1.5 sigma level.

A correction needs to be taken into account: the distribution of quenching factor for a given recoil energy might not be gaussian as far away from Q=1. To test this assumption, we measure the data counting rate in a box above Q=1, symmetrical to the β box: 1.3<Q<1.8 and 30 keV<E_R<80 keV.

In this region we find out 0.23±0.05 events/kg·d. This represents the 1.4% of total gamma rate in 30-80 keV recoil energy range. It is larger than that we expected, since this region is outside the 99.9% electron recoil band. We can conclude that non-gaussian tails are important, and must be taken into account.

If we subtract this evaluation of the contribution of the non-gaussian tails from the observed number of betas (assuming thus that the non-gaussian contributions are are symmetrical around Q=1), we obtain 0.37±0.08 beta/kg·d. This rate is then compared with the predicted values of 0.4±0.1 beta/kg·d.

The fact that a perfect agreement is found indicates that the events in the nuclear recoil band between 30 and 80 keV can be explained by the beta background associated with the observed alpha rate. But this analysis revealed that the factors entering this prediction have large uncertainties:

* the charge state of the detector;

* the difference between hole and electron trapping;

* the non-gaussian distribution of the quenching factor.

Thus, in order to obtain an exclusion plot on the scattering cross section of WIMP on nucleon as a function of WIMP mass, we prefer to perform no subtraction and use the Yellin method. Furthermore, the number of events recorded in the nuclear recoil band in the present experiment is so small that

a subtraction would not improve the numerical result a lot, and introduce large systematical uncertainties.

Conclusions

I have studied the low background physics data collected during the 8^{th} cool down of EDELWEISS-II ("run 8"). This cool down allows a first real look at the EDELWEISS-II environment and it represents a first real test of Ge-NTD type detectors at large scale. Two goals are envisaged: a better understanding of radiative background of the experiment and an improvement of current upper limit on the WIMP scattering cross section.

The recoil energy range is constrained by a beta population at low recoil energies linked to a ^{210}Pb contamination observed in EDELWEISS-I. The lower bound in the recoil energy range has been set at 30 keV for the WIMP search.

After quality cuts we obtain a total fiducial exposure of 93.5 kg·d

Three events have been observed in the nuclear recoil band. Under standard assumption of an isothermal dark matter distribution with a density 0.3 GeV/c^2 cm^{-3} and typical values for Earth and characteristic velocities, the calculated WIMP exclusion limit for spin-independent WIMP-nucleus interaction correspond to a best sensitivity of 5×10^{-7}pb for a 80GeV/c^2 WIMP mass. It represents an improvement of about a factor 3 relative to EDELWEISS-I [4], but not yet competitive with current limits provided by CDMS [74] and XENON [82].

The limitation for Ge-NTD type detectors arises from the incapability of an active surface events rejection. The present work also showed that the three events recorded in the nuclear recoil band are compatible with a ^{210}Pb pollution. With this type of background, the standard Ge-NTD detectors are not competitive for WIMP searches. As a consequence of this work, in the current runs of EDELWEISS they have been replaced by ID detectors: Ge-NTD detectors with a special interdigitized electrode scheme allowing an active surface event discrimination.

In low background experiments of rare events, such as the EDELWEISS experiment, several factors in the experimental backgrounds can obscure the signal counts of interest. These experiment backgrounds are environmental radioactivity, intrinsic contamination of detectors and shielding material,

airborne radioactivity (Radon) and cosmic rays induced particles.

Two investigations have been carried out in order to achieve a better background understanding. One study is related to γ-ray background overwhelming the detectors and a second one is linked to the confirmation of the ^{210}Pb contamination interpretation as resulting in the first stage of the experiment [96].

Gamma background has been investigated both at high (>100 keV) and low energy (<100 keV), this latter being the energy range of interest in the WIMP search.

We observe a global and uniform reduction of γ background of about a factor 2 compared to EDELWEISS-I for energy higher than hundred keV.

Monte Carlo simulations have been developed in order to better understand the observations. With a simulation of the closest material to the detector (Cu), we evaluate their radioactive contamination to about 0.2 mBq/kg of ^{60}Co and 0.4 mBq/kg from the U/Th decay chain. These measurements are lower than the available upper limits on activity of the copper.

At low energy (<100 keV) the γ background has been studied in order to give an estimation of how dangerous a likely γ-leakage in the nuclear recoil band could be. With a fixed 30 keV low energy limit for the WIMP search analysis, this leakage appears not to be a problem. Extrapolating the obtained results for the future, both for EDELWEISS and next-generation tonne-scale direct dark matter detection experiment, we have to pay attention to the energy range around 10 keV. In fact, in addition to a γ continuum contribution we have the 10 keV cosmogenic peak to take into account: the leakage in this region is mainly due to this peak.

The alpha population at about 5 MeV recoil energy, related to the ^{210}Pb has been reduced by about a factor two compared to EDELWEISS-I. Furthermore, with a calibration using a ^{210}Pb source and the current data we have succeeded in the confirmation of the ^{210}Pb chain as a source of background events in the WIMP search.

Even if predicted number of low energy betas is consistent with the observed rates, this is not enough to deserve a background subtraction. In fact, large uncertainties linked to charge collection profile, Pb implantation profile threaten these predictions.

Appendix A

1

		^{133}Ba			low background		
No	Name	center	guard	heat	center	guard	heat
4	GGA14	1.4	1.6	1.9	1.5	1.7	2.2
5	GGA13	1.6	1.6	1.2	1.7	1.7	1.5
6	GSA11	1.3	2.4	2.5	1.5	2.5	1.9
7	GGA10	1.6	1.7	1.6	1.7	1.8	1.8
8	GGA7	1.7	1.5	3.6	1.8	1.6	3.3
9	GSA10	1.9	1.7	1.7	2.1	1.8	1.4
10	GGA3	1.4	1.5	2.4	1.5	1.6	2.4
11	GGA5	1.4	1.5	1.9	1.4	1.6	1.9
14	GGA8	3.8	2.1	2.8	4.2	2.4	2.7
15	GSA8	2.0	1.5	3.1	2.0	1.5	3.2
17	GGA4	1.8	2.1	1.2	1.7	2.1	1.3
18	GGA9	1.7	1.7	1.3	1.7	1.7	1.4
19	GSA7	2.2	3.1	2.9	2.3	3.2	3.0
22	GGA1	2.0	8.6	3.5	2.2	8.9	3.4
23	GSA3	3.6	4.0	5.5	3.5	3.9	7.4

Table A.1: Mean values of baseline resolutions over the data taking period (for ^{133}Ba calibration run in January 2008 and for low background physics run from November 2007 to March 2008)

		^{133}Ba -7V		
No	Name	center	guard	heat
4	GGA14	4.2±0.3	5.4±0.5	10.3±0.8
5	GGA13	4.3±0.1	4.1±0.2	7.0±0.2
6	GSA11	4.0±0.2	7.8±0.7	7.4±0.4
7	GGA10	5.2±0.2	4.4±0.1	9.1±0.5
8	GGA7	5.1±0.1	4.7±0.2	12.7±0.6
9	GSA10	5.1±0.5	3.8±0.5	5.2±0.6
10	GGA3	4.4±0.2	4.4±0.2	7.3±0.4
11	GGA5	3.9±0.1	5.0±0.3	5.1±0.1
12	GGA11	5.9±0.2	4.3±0.2	6.6±0.3
15	GSA8	5.6±0.1	5.1±0.1	17.4±0.4
17	GGA4	4.3±0.4	5.1±0.5	10.7±1.0
18	GGA9	4.3±0.1	5.3±0.3	6.4±0.3
19	GSA7	4.9±0.4	–	4.8±1.1
22	GGA1	4.8±0.4	11.6±0.7	10.9±0.5

Table A.2: FWHM resolution in keV at 356 keV (mean value for all ^{133}Ba run in January 2008).

Mac	No	Name	low-bkg			
			Nov07		Dec07	
			kg·d B	kg·d A	kg·d B	kg·d A
1	4	GGA14	0.830	0.84	4.289	4.15
	5	GGA13	0.830	0.84	4.289	4.15
	6	GSA11	0.830	0.84	4.289	4.15
	7	GGA10	0.830	0.84	4.289	4.15
	8	GGA7	0.830	0.84	4.289	4.15
	9	GSA10	0.830	0.43	4.289	4.15
	10	GGA3	0.830	0.84	4.289	4.15
2	11	GGA5	0.809	0.80	4.346	4.15
	12	GGA11	0.809	0.80	4.346	4.15
	14	GGA8	0.809	0.80	4.346	4.15
	15	GSA8	0.809	0.80	4.346	4.16
	17	GGA4	0.809	0.80	4.346	4.15
	18	GGA9	0.809	0.80	4.346	4.15
3	19	GSA7	0.778	0.79	4.009	3.94
	21	GSA1	0.778	0.79	4.009	3.88
	22	GGA1	0.778	0.79	4.009	3.88
	23	GSA3	0.778	0.79	4.009	3.94
		Tot	13.78	13.43	72.14	69.6

Table A.3: Number of kg·d exposure before binning cuts (kg·d B) and number of kg·d exposure calculated with a 15 minute bin for low background physics run (kg·d A) and for fiducial volume.

Mac	No	Name	low-bkg					
			Jan08		Fev08		Mar08	
			kg·d B	kg·d A	kg·d B	kg·d A	kg·d B	kg·d A
1	4	GGA14	3.484	3.22	2.472	2.44	1.888	1.94
	5	GGA13	3.484	3.39	2.472	2.44	1.888	1.94
	6	GSA11	3.484	3.39	2.472	2.44	1.888	1.94
	7	GGA10	3.484	3.22	2.472	2.44	1.888	1.94
	8	GGA7	3.484	3.22	2.472	2.44	1.888	1.94
	9	GSA10	3.484	3.22	2.472	2.44	1.888	1.94
	10	GGA3	3.484	3.39	2.472	2.44	1.888	1.94
2	11	GGA5	3.575	3.41	2.481	2.5	1.913	1.97
	12	GGA11	3.575	3.24	2.481	2.5	1.913	1.97
	14	GGA8	3.575	3.06	2.481	2.5	1.913	1.98
	15	GSA8	3.575	3.41	2.481	2.5	1.913	1.98
	17	GGA4	3.575	2.89	2.481	2.5	1.913	1.98
	18	GGA9	3.575	3.24	2.481	2.5	1.913	1.98
3	19	GSA7	3.657	3.39	2.477	2.4	1.875	1.88
	21	GSA1	3.657	3.50	2.477	2.4	1.875	1.88
	22	GGA1	3.657	3.21	2.477	2.4	1.875	1.88
	23	GSA3	3.657	3.21	2.477	1.81	–	–
		Tot	60.47	59.02	42.10	41.09	30.32	31.08

Table A.4: Number of kg·d exposure before all cuts (kg·d B) and number of kg·d calculated with a 15 minute bin for low background physics run (kg·d A) and for fiducial volume.

Month	kg·d		%
	kg·d B	kg·d A	[1-(A/B)]
Nov07	13.78	13.43	2.5
Dec07	72.14	69.6	3.5
Jan08	60.47	59.02	2.4
Fev08	42.10	41.09	2.4
Mar08	30.32	31.08	2.5
Tot	218.81	214.22	2.1

Table A.5: Number of kg·d exposure before binning cuts (kg·d B) and number of kg·d calculated with a 15 minute bin for low background physics run (kg·d A) and for fiducial volume as a function of acquisition month and the relative error (%) made recovering hours bins.

		Nov07		Dec07		Jan08		Feb08		Mar08	
No	Name	Ic	$Heat_{max}$	Ic	$Heat_{max}$	Ic	$Heat_{max}$	Ic	$Heat_{max}$	Ic	$Heat_{m}$
4	GGA14	1.5	3.250	1.5	3.250	1.5	3.250	1.4	3.296	1.4	3.29
5	GGA13	1.7	3.145	1.6	3.196	1.6	3.196	1.6	3.196	1.5	3.25
6	GSA11	1.6	3.196	1.4	3.296	1.5	3.250	1.4	3.296	1.2	3.37
7	GGA10	1.7	3.145	1.7	3.145	1.7	3.145	1.6	3.196	1.6	3.19
8	GGA7	1.7	3.145	1.7	3.145	1.7	3.145	1.7	3.145	1.7	3.14
9	GSA10	2.3	2.721	2.3	2.721	2.2	2.802	1.9	3.023	1.8	3.08
10	GGA3	1.6	3.196	1.5	3.250	1.5	3.250	1.5	3.250	1.4	3.29
11	GGA5	1.4	3.296	1.4	3.296	1.5	3.250	1.4	3.296	1.3	3.33
12	GGA11	2.0	2.958	2.2	2.802	2.2	2.802	2.0	2.958	1.8	3.08
14	GGA8	4.5	–	4.4	–	4.2	–	3.8	–	3.7	–
15	GSA8	2.0	2.958	2.0	2.958	2.1	2.885	2.0	2.958	1.9	3.02
17	GGA4	1.7	3.145	1.7	3.145	1.7	3.145	1.6	3.196	1.5	3.25
18	GGA9	1.6	3.196	1.6	3.196	1.6	3.196	1.7	3.145	1.6	3.19
19	GSA7	2.3	2.721	2.2	2.802	2.1	2.885	2.2	2.802	2.1	2.88
21	GSA1	1.7	3.145	1.6	3.196	1.7	3.145	1.5	3.250	1.4	3.29
22	GGA1	2.4	2.634	2.1	2.885	2.2	2.802	2.0	2.958	2.0	2.95
23	GSA3	3.6	–	3.5	0.336	3.7	–	3.0	1.884	0.0	–

Table A.6: Heat maximum baseline resolution for each acquisition month, as a function of ionization baseline resolution, imposing the 30 keV magic point, using Tab. 3.1.

Mac	No	Name	low-bkg			
			Nov07		Dec07	
			Total	Fiducial	Total	Fiducial
1	4	GGA14	1.09	0.62	5.59	3.18
	5	GGA13	1.01	0.57	5.99	3.42
	6	GSA11	1.04	0.6	6.34	3.61
	7	GGA10	1.03	0.59	6.49	3.7
	8	GGA7	0.43	0.24	2.77	1.58
	9	GSA10	0.63	0.36	5.89	3.36
	10	GGA3	1.14	0.65	6.13	3.5
2	11	GGA5	1.32	0.75	5.97	3.4
	12	GGA11	0.45	0.26	5.1	2.91
	15	GSA8	0.2	0.11	0.17	0.1
	17	GGA4	1.12	0.64	5.73	3.26
	18	GGA9	0.89	0.5	5.74	3.27
3	19	GSA7	0.09	0.05	3.15	1.79
	22	GGA1	0.04	0.02	1.88	1.07
		Tot	10.48	5.96	66.94	38.15

Table A.7: Number of kg·d exposure for total and fiducial volume after all quality cuts.

Mac	No	Name	low-bkg					
			Jan08		Fev08		Mar08	
			Total	Fiducial	Total	Fiducial	Total	Fiducial
1	4	GGA14	4.63	2.64	3.53	2.01	2.72	1.55
	5	GGA13	4.67	2.66	2.87	1.63	2.61	1.49
	6	GSA11	4.82	2.75	2.72	1.55	2.89	1.64
	7	GGA10	5.2	2.97	3.82	2.18	2.96	1.69
	8	GGA7	0.82	0.47	1.42	0.81	2.98	1.7
	9	GSA10	4.73	2.69	3.28	1.87	2.9	1.65
	10	GGA3	5.3	3.02	3.98	2.27	3.25	1.85
2	11	GGA5	5.09	2.9	3.94	2.25	3.25	1.85
	12	GGA11	4.05	2.31	2.75	1.56	2.73	1.56
	15	GSA8	0.03	0.02	0.12	0.07	0.83	0.47
	17	GGA4	4.11	2.34	2.78	1.59	2.53	1.44
	18	GGA9	4.66	2.65	3.18	1.81	2.95	1.68
3	19	GSA7	3.17	1.81	1.64	0.93	1.64	0.93
	22	GGA1	0.27	0.15	0.91	0.52	2.1	1.2
		Tot	51.55	29.38	36.94	21.05	36.34	20.7

Table A.8: Number of kg·d exposure for total and fiducial volume after all quality cuts.

Month	Fid kg·d	Qc<0.5	NB	up NB	down NB
Nov07	5.08	2	0	0	2
Dec07	30.56	5	0	3	2
Jan08	24.17	8	2	2	4
Fev08	17.42	5	1	1	3
Mar08	16.30	8	1	2	5
Tot	93.53	28	4	8	16

Table A.9: Number of events recorded in the Qc<0.5 zone, in the neutron band (NB), in the region between Q_c <0.5 and the neutron band: NB< Q_c <0.5 (up NB) and in the region between neutron band and ionization threshold : NB< Q_c <Ion-Thr (down NB) after all cuts for 30<Er_c <500 keV.

Run	Evt No.	Erc (keV)	Bolo
121905	1899	41.8	4-GGA14
321802	8138	30.2	19-GSA7
131303	788	30.4	7-GGA10
141201	7553	335.5	4-GGA14

Table A.10: Tagging of events recorded in the neutron band (NB) after all cuts for 30<Er_c <500 keV.

		kg·d	
No	Name	Total	Fiducial
4	GGA14	13.27	7.57
5	GGA13	16.81	9.59
7	GGA10	16.57	9.45
9	GSA10	4.52	2.57
10	GGA3	4.77	2.72
11	GGA5	16.72	9.54
17	GGA4	16.27	9.27
18	GGA9	17.33	9.86
Total stat		106.26	60.57

Table A.11: Number of kg·d exposure for total and fiducial volume for bolometers having a 20 keV magic point selection after quality cuts.

No	Name-Pos.	Month	kg·d	counts	total γ rate
4	GGA14-c1	Nov	1.47	277	188.4 ± 11.3
		Dec	7.28	1271	174.6 ± 4.9
		Jan	5.65	972	172.0 ± 5.5
		Feb	4.28	701	163.8 ± 6.2
		Mar	3.41	568	166.6 ± 7.0
5	GGA13-d1	Nov	1.47	443	301.4 ± 14.3
		Dec	7.29	1711	234.7 ± 5.7
		Jan	5.94	1377	231.8 ± 6.2
		Feb	4.28	1228	286.9 ± 8.2
		Mar	3.41	877	257.2 ± 8.7
6	GSA11-b2	Nov	1.47	244	166.0 ± 10.6
		Dec	7.28	1369	188.0 ± 5.1
		Jan	5.94	1087	183.0 ± 5.6
		Feb	4.28	970	226.6 ± 7.3
		Mar	3.41	645	189.2 ± 7.4
7	GGA10-c2	Nov	1.47	295	200.7 ± 11.7
		Dec	7.28	1431	196.6 ± 5.2
		Jan	5.65	1150	203.5 ± 6.0
		Feb	4.28	1012	236.4 ± 7.4
		Mar	3.41	696	204.1 ± 7.7
8	GGA7-d2	Nov	1.47	375	255.1 ± 13.2
		Dec	7.28	1695	232.8 ± 5.7
		Jan	5.65	1366	241.8 ± 6.5
		Feb	4.28	1211	282.9 ± 8.1
		Mar	3.41	825	241.9 ± 8.4
9	GSA10-b3	Nov	0.76	149	196.1 ± 16.1
		Dec	7.28	1400	192.3 ± 5.1
		Jan	5.65	1105	195.6 ± 5.9
		Feb	4.28	989	231.1 ± 7.3
		Mar	3.41	672	197.1 ± 7.6
10	GGA3-d3	Nov	1.47	446	303.4 ± 14.4
		Dec	7.28	1898	260.7 ± 6.0
		Jan	5.95	1531	257.3 ± 6.6
		Feb	4.28	1362	318.2 ± 8.6
		Mar	3.41	906	265.7 ± 8.8
11	GGA5-c4	Nov	1.41	276	195.7 ± 11.8
		Dec	7.29	1332	182.7 ± 5.0
		Jan	5.98	1103	184.4 ± 5.6
		Feb	4.39	792	180.4 ± 6.4
		Mar	3.46	673	194.5 ± 7.5

Table A.12: Gamma background rates (total volume) in counts/kg·d.

No	Name-Pos.	Month	kg·d	counts	total γ rate
12	GGA11-d4	Nov	1.41	331	234.8 ± 12.9
		Dec	7.29	1542	211.5 ± 5.4
		Jan	5.68	1245	219.2 ± 6.2
		Feb	4.39	853	194.3 ± 6.7
		Mar	3.46	720	208.1 ± 7.8
15	GSA8-d5	Nov	1.41	295	209.2 ± 12.2
		Dec	7.29	1459	200.1 ± 5.2
		Jan	5.99	1183	197.5 ± 5.7
		Feb	4.39	788	179.5 ± 6.4
		Mar	3.47	662	190.8 ± 7.4
17	GGA4-c6	Nov	1.41	251	178.0 ± 11.2
		Dec	7.29	1235	169.4 ± 4.8
		Jan	5.07	850	167.7 ± 5.8
		Feb	4.39	715	162.9 ± 6.1
		Mar	3.47	581	167.4 ± 6.9
18	GGA9-d6	Nov	1.41	326	231.2 ± 12.8
		Dec	7.29	1534	210.4 ± 5.4
		Jan	5.68	1206	212.3 ± 6.1
		Feb	4.39	917	208.9 ± 6.9
		Mar	3.47	696	200.6 ± 7.6
19	GSA7-b7	Nov	1.41	288	204.3 ± 12.0
		Dec	6.91	1568	226.9 ± 5.7
		Jan	5.94	1328	223.6 ± 6.1
		Feb	4.21	829	196.9 ± 6.8
		Mar	3.31	729	220.2 ± 8.2

Table A.13: Gamma background rates (total volume in counts/kg·d.)

No	Name-Pos.	Month	kg·d	counts	total γ rate
4	GGA14-c1	Nov07	1.09	208	190.8 ± 13.2
		Dec07	5.59	964	172.5 ± 5.6
		Jan08	4.63	787	170.0 ± 6.1
		Feb08	3.53	591	167.4 ± 6.9
		Mar08	2.72	466	171.3 ± 7.9
5	GGA13-d1	Nov07	1.01	302	299.0 ± 17.2
		Dec07	5.99	1416	236.4 ± 6.3
		Jan08	4.67	1111	237.9 ± 7.1
		Feb08	2.87	627	218.5 ± 8.7
		Mar08	2.61	607	232.6 ± 9.4
6	GSA11-b2	Nov07	1.04	170	163.5 ± 12.5
		Dec07	6.24	1184	189.7 ± 5.5
		Jan08	4.82	840	174.3 ± 6.0
		Feb08	2.72	483	177.6 ± 8.1
		Mar08	2.89	536	185.5 ± 8.0
7	GGA10-c2	Nov07	1.03	199	193.2 ± 13.7
		Dec07	6.49	1278	196.9 ± 5.5
		Jan08	5.2	981	188.7 ± 6.0
		Feb08	3.82	768	201.0 ± 7.3
		Mar08	2.96	554	187.2 ± 8.0
8	GGA7-d2	Nov07	0.43	104	241.9 ± 23.7
		Dec07	2.77	667	240.8 ± 9.3
		Jan08	0.82	192	234.1 ± 16.9
		Feb08	1.42	307	216.2 ± 12.3
		Mar08	2.98	690	231.5 ± 8.8
9	GSA10-b3	Nov07	0.63	122	193.7 ± 17.5
		Dec07	5.89	1112	188.8 ± 5.7
		Jan08	4.73	941	198.9 ± 6.5
		Feb08	3.28	566	172.6 ± 7.3
		Mar08	2.9	498	171.7 ± 7.7
10	GGA3-d3	Nov07	1.14	348	305.3 ± 16.4
		Dec07	6.13	1634	266.6 ± 6.6
		Jan08	5.3	1408	265.7 ± 7.1
		Feb08	3.98	930	233.7 ± 7.7
		Mar08	3.25	740	227.7 ± 8.4
11	GGA5-c4	Nov07	1.32	260	197.0 ± 12.2
		Dec07	5.97	1106	185.3 ± 5.6
		Jan08	5.09	910	178.8 ± 5.9
		Feb08	3.94	720	182.7 ± 6.8
		Mar08	3.25	591	181.8 ± 7.5

Table A.14: Gamma background rates (total volume quality cut) in counts/kg·d.

No	Name-Pos.	Month	kg·d	counts	total γ rate
12	GGA11-d4	Nov07	0.45	103	228.9 ± 22.6
		Dec07	5.1	1088	213.3 ± 6.5
		Jan08	4.05	798	197.0 ± 7.0
		Feb08	2.75	545	198.2 ± 8.5
		Mar08	2.73	593	217.2 ± 8.9
15	GSA8-d5	Nov07	0.2	29	145.0 ± 26.9
		Dec07	0.17	32	188.2 ± 33.3
		Jan08	0.03	5	166.7 ± 74.5
		Feb08	0.12	15	125.0 ± 32.3
		Mar08	0.83	157	189.2 ± 15.1
17	GGA4-c6	Nov07	1.12	199	177.7 ± 12.6
		Dec07	5.73	973	169.8 ± 5.4
		Jan08	4.11	705	171.5 ± 6.5
		Feb08	2.78	451	162.2 ± 7.6
		Mar08	2.53	435	171.9 ± 8.2
18	GGA9-d6	Nov07	0.89	218	244.9 ± 16.6
		Dec07	5.74	1191	207.5 ± 6.0
		Jan08	4.66	988	212.0 ± 6.7
		Feb08	3.18	666	209.4 ± 8.1
		Mar08	2.95	616	208.8 ± 8.4
19	GSA7-b7	Nov07	0.09	19	211.1 ± 48.4
		Dec07	3.15	705	223.8 ± 8.4
		Jan08	3.17	760	239.7 ± 8.7
		Feb08	1.64	323	197.0 ± 11.0
		Mar08	1.64	368	224.4 ± 11.7

Table A.15: Gamma background rates (total volume quality cut) in counts/kg·d.

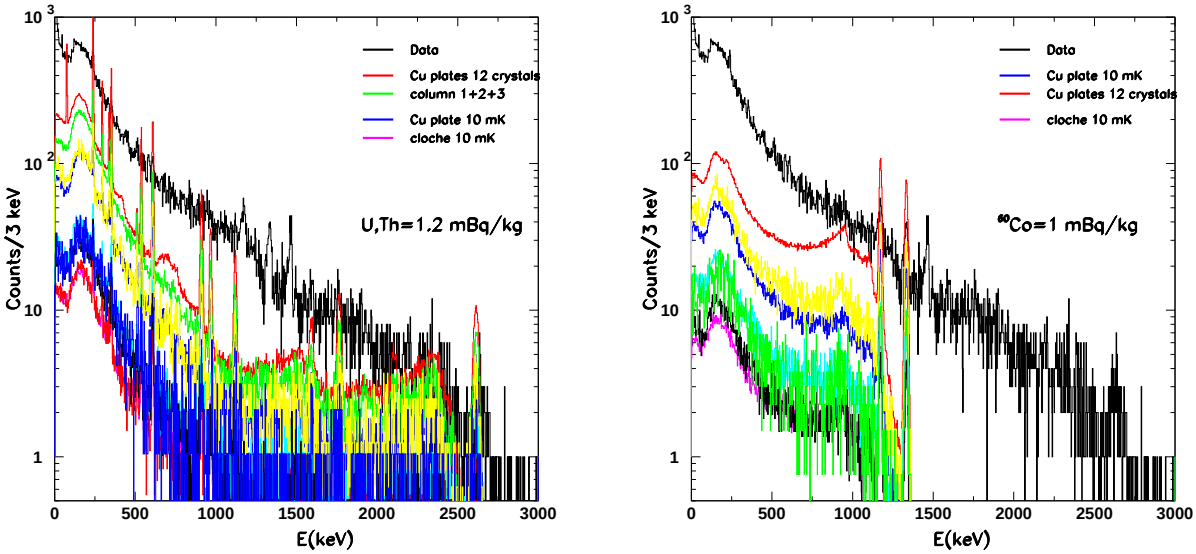

Figure A.1: Gamma background energy spectrum (total ionization channel) without any quality cut corresponding to a total exposure of about 310 kg·d compared to Monte Carlo simulations of various sources of radioactive contamination. *Left side*: simulation of U/Th contamination everywhere in the setup. *Right side*: simulation of ^{60}Co activity of copper materials close to detectors (detector holders, cryostat).

No	Name	Pos	low bck		
			kg·d	counts	α rate
4	GGA14	c1	12.590	20	1.6 ± 0.4
5	GGA13	d1	12.760	21	1.6 ± 0.4
6	GSA11	b2	12.760	13	1.0 ± 0.3
7	GGA10	c2	12.590	51	4.1 ± 0.6
8	GGA7	d2	12.590	31	2.5 ± 0.4
9	GSA10	b3	12.180	24	2.0 ± 0.4
10	GGA3	d3	12.760	22	1.7 ± 0.4
11	GGA5	c4	12.830	48	3.7 ± 0.5
12	GGA11	d4	12.660	33	2.6 ± 0.5
14	GGA8	c5	12.490	22	1.8 ± 0.4
15	GSA8	d5	12.850	19	1.5 ± 0.3
17	GGA4	c6	12.320	12	1.0 ± 0.3
18	GGA9	d6	12.670	16	1.3 ± 0.3
19	GSA7	b7	12.400	19	1.5 ± 0.4
21	GSA1	d7	12.450	46	3.7 ± 0.5
22	GGA1	b10	12.160	110475	9085.1 ± 27.3
23	GSA3	c10	9.750	107	11.0 ± 1.1

Table A.16: Alpha rates for low background physics run (fiducial volume without quality cuts.

No	Name	Pos	low bck		
			kg·d	counts	α rate
4	GGA14	c1	22.090	80	3.6 ± 0.4
5	GGA13	d1	22.390	115	5.1 ± 0.5
6	GSA11	b2	22.380	52	2.3 ± 0.3
7	GGA10	c2	22.080	105	4.8 ± 0.5
8	GGA7	d2	22.090	77	3.5 ± 0.4
9	GSA10	b3	21.380	82	3.8 ± 0.4
10	GGA3	d3	22.390	121	5.4 ± 0.5
11	GGA5	c4	22.530	94	4.2 ± 0.4
12	GGA11	d4	22.230	74	3.3 ± 0.4
14	GGA8	c5	21.930	78	3.6 ± 0.4
15	GSA8	d5	22.550	54	2.4 ± 0.3
17	GGA4	c6	21.630	51	2.4 ± 0.3
18	GGA9	d6	22.240	57	2.6 ± 0.3
19	GSA7	b7	21.760	105	4.8 ± 0.5
21	GSA1	d7	21.850	140	6.4 ± 0.5
22	GGA1	b10	21.350	11833	554.2 ± 5.1
23	GSA3	c10	17.120	143	8.4 ± 0.7

Table A.17: Alpha rates for low background physics run (total volume) without quality cuts.

Type	No	bck -7V	
		α rate Total Volume	α rate Fiducial Volume
Cu-Cu	8	3.77±0.15	1.92±0.14
Cu- Ge	1	4.8±0.50	2.60±0.50
Ge - Ge	3	4.49±0.26	2.00±0.23
Si-Si	3	3.91±0.24	2.50±0.26

Table A.18: Alpha average rate based on cover categories for rate coming out from alpha selection (0.01<Q<0.6 and 3000<Er<7000 keV).

Bibliography

[1] G. Hinshaw et al. Five-Year Wilkinson Microwave Anisotropy Probe (WMAP) Observations:Data Processing, Sky Maps, & Basic Results. *Astrophys. J. Suppl.*, 180:225–245, 2009.

[2] K. A. Olive. TASI Lectures on Dark Matter. Summary of lectures given at the Theoretical Advanced Study Institute in Elementary Particle Physics at the University of Colorado at Boulder - June 2-28, 2002.

[3] Joseph Silk and Mark Srednicki. Cosmic-ray antiprotons as a probe of a photino-dominated universe. *Phys. Rev. Lett.*, 53:624, 1984.

[4] Veronique Sanglard et al. Final results of the EDELWEISS-I dark matter search with cryogenic heat-and-ionization Ge detectors. *Phys. Rev.*, D71:122002, 2005.

[5] Edwin Hubble. A relation between distance and radial velocity among extra–galactic nebulae. *Proc. Nat. Acad. Sci.*, 15:168–173, 1929.

[6] H. Ohanian and R. Ruffini. Gravitation and space-time. New York, USA: Norton (1994) 679 p.

[7] Carlo R. Contaldi, Henk Hoekstra, and Antony Lewis. Joint CMB and Weak Lensing Analysis: Physically Motivated Constraints on Cosmological Parameters. *Phys. Rev. Lett.*, 90:221303, 2003.

[8] Ian Affleck and Michael Dine. A New Mechanism for Baryogenesis. *Nucl. Phys.*, B249:361, 1985.

[9] M. Joyce and Mikhail E. Shaposhnikov. Primordial magnetic fields, right electrons, and the Abelian anomaly. *Phys. Rev. Lett.*, 79:1193–1196, 1997.

[10] Opik E. *Bull. de la Soc. de Russie*, 21:150, 1915.

[11] F. Zwicky. Spectral displacement of extra galactic nebulae. *Helv. Phys. Acta*, 6:110–127, 1933.

[12] George R. Blumenthal, S. M. Faber, Joel R. Primack, and Martin J. Rees. Formation of galaxies and large-scale structure with cold dark matter. *Nature*, 311:517–525, 1984.

[13] Gianfranco Bertone, Dan Hooper, and Joseph Silk. Particle dark matter: Evidence, candidates and constraints. *Phys. Rept.*, 405:279–390, 2005.

[14] K. G. Begeman, A. H. Broeils, and R. H. Sanders. Extended rotation curves of spiral galaxies: Dark haloes and modified dynamics. *Mon. Not. Roy. Astron. Soc.*, 249:523, 1991.

[15] Neta A. Bahcall, Lori M. Lubin, and Victoria Dorman. Where is the dark matter? *Astrophys. J.*, 447:L81, 1995.

[16] Ray Carlberg et al. Galaxy Cluster Virial Masses and Omega. *Astrophys. J.*, 462:32, 1996.

[17] August E. Evrard, Christopher A. Metzler, and Julio F. Navarro. Mass Estimates of X-Ray Clusters. *Astrophys. J.*, 469:494, 1996.

[18] I. Smail et al. *Astrophys. J.*, 479:70, 1996.

[19] Antonino Del Popolo. Improvements in the M-T relation and mass function and the measured Omega_m through clusters evolution. *Astrophys. J.*, 599:723–737, 2003.

[20] D. N. Spergel et al. Wilkinson Microwave Anisotropy Probe (WMAP) three year results: Implications for cosmology. *Astrophys. J. Suppl.*, 170:377, 2007.

[21] N. W. Halverson et al. DASI First Results: A Measurement of the Cosmic Microwave Background Angular Power Spectrum. *Astrophys. J.*, 568:38–45, 2002.

[22] R. Stompor et al. Cosmological implications of the MAXIMA-I high resolution Cosmic Microwave Background anisotropy measurement. *Astrophys. J.*, 561:L7–L10, 2001.

[23] P.J.E Peebles et al. *Phys. Rev. Lett.*, 16:410–413, 1966.

[24] Robert V. Wagoner, William A. Fowler, and Fred Hoyle. On the Synthesis of elements at very high temperatures. *Astrophys. J.*, 148:3–49, 1967.

[25] David Tytler, John M. O'Meara, Nao Suzuki, and Dan Lubin. Review of Big Bang Nucleosynthesis and Primordial Abundances. *Phys. Scripta*, T85:12, 2000.

[26] S. Burles et al. *Astrophys. J.*, 483:778, 1997.

[27] S. Perlmutter et al. Measurements of Omega and Lambda from 42 High-Redshift Supernovae. *Astrophys. J.*, 517:565–586, 1999.

[28] Adam G. Riess et al. Type Ia Supernova Discoveries at z>1 From the Hubble Space Telescope: Evidence for Past Deceleration and Constraints on Dark Energy Evolution. *Astrophys. J.*, 607:665–687, 2004.

[29] Katherine Freese, Fred C. Adams, Joshua A. Frieman, and Emil Mottola. Cosmology with Decaying Vacuum Energy. *Nucl. Phys.*, B287:797, 1987.

[30] Cedric Deffayet, G. R. Dvali, Gregory Gabadadze, and Arkady I. Vainshtein. Nonperturbative continuity in graviton mass versus perturbative discontinuity. *Phys. Rev.*, D65:044026, 2002.

[31] Sean M. Carroll, Vikram Duvvuri, Mark Trodden, and Michael S. Turner. Is cosmic speed-up due to new gravitational physics? *Phys. Rev.*, D70:043528, 2004.

[32] Scott Dodelson. Modern cosmology. Amsterdam, Netherlands: Academic Pr. (2003) 440 p.

[33] Gerard Jungman, Marc Kamionkowski, and Kim Griest. Supersymmetric dark matter. *Phys. Rept.*, 267:195–373, 1996.

[34] Edward A. Baltz. Dark matter candidates. 2004.

[35] Kim Griest and Marc Kamionkowski. Unitarity Limits on the Mass and Radius of Dark Matter Particles. *Phys. Rev. Lett.*, 64:615, 1990.

[36] M. Beck et al. Searching for dark matter with the enriched detectors of the Heidelberg - Moscow Double Beta Decay Experiment. *Phys. Lett.*, B336:141–146, 1994.

[37] M. Ambrosio et al. Limits on dark matter WIMPs using upward-going muons in the MACRO detector. *Phys. Rev.*, D60:082002, 1999.

[38] Y. Fukuda et al. Evidence for oscillation of atmospheric neutrinos. *Phys. Rev. Lett.*, 81:1562–1567, 1998.

[39] Kim Griest and Joseph Silk. PROSPECTS FADE FOR NEUTRINO COLD DARK MATTER. *Nature*, 343:26–27, 1990.

[40] Stephen P. Martin. A Supersymmetry Primer. 1997.

[41] N. Gehrels and P. Michelson. GLAST: The next-generation high energy gamma-ray astronomy mission. *Astropart. Phys.*, 11:277–282, 1999.

[42] Alessandro Cesarini, Francesco Fucito, Andrea Lionetto, Aldo Morselli, and Piero Ullio. The galactic center as a dark matter gamma-ray source. *Astropart. Phys.*, 21:267–285, 2004.

[43] A. Morselli and P. Picozza. Search for dark matter using antiproton and positron spectra with PAMELA. Prepared for 4th International Workshop on the Identification of Dark Matter (IDM 2002), York, England, 2- 6 Sep 2002.

[44] M. Sapinski. Indirect search for dark matter with AMS experiment. *Acta Phys. Polon.*, B37:1991–1995, 2006.

[45] Gianfranco Bertone, Emmanuel Nezri, Jean Orloff, and Joseph Silk. Neutrinos from dark matter annihilations at the galactic centre. *Phys. Rev.*, D70:063503, 2004.

[46] Lars Bergstrom, Joakim Edsjo, and Paolo Gondolo. Indirect neutralino detection rates in neutrino telescopes. *Phys. Rev.*, D55:1765–1770, 1997.

[47] M. Ackermann et al. Limits to the muon flux from neutralino annihilations in the Sun with the AMANDA detector. *Astropart. Phys.*, 24:459–466, 2006.

[48] T. DeYoung. Status of the IceCube neutrino telescope. *Int. J. Mod. Phys.*, A20:3160–3162, 2005.

[49] J. Brunner. Status of the ANTARES project. *Nucl. Phys. Proc. Suppl.*, 145:323–326, 2005.

[50] P.F Smith and J.C. Lewin. *Phys. Rep.*, 187:203, 1990.

[51] Andriy Kurylov and Marc Kamionkowski. Generalized analysis of weakly-interacting massive particle searches. *Phys. Rev.*, D69:063503, 2004.

[52] V. A. Bednyakov and H. V. Klapdor-Kleingrothaus. Update of the direct detection of dark matter and the role of the nuclear spin. *Phys. Rev.*, D63:095005, 2001.

[53] A. K. Drukier, K. Freese, and D. N. Spergel. Detecting Cold Dark Matter Candidates. *Phys. Rev.*, D33:3495–3508, 1986.

[54] S. Cebrian et al. Sensitivity plots for WIMP direct detection using the annual modulation signature. *Astropart. Phys.*, 14:339–350, 2001.

[55] David N. Spergel. THE MOTION OF THE EARTH AND THE DETECTION OF WIMPs. *Phys. Rev.*, D37:1353, 1988.

[56] Ben Morgan, Anne M. Green, and Neil J. C. Spooner. Directional statistics for WIMP direct detection. *Phys. Rev.*, D71:103507, 2005.

[57] David O. Caldwell et al. Laboratory limits on galactic cold dark matter . *Phys. Rev. Lett.*, 61:510, 1988.

[58] R. Bernabei et al. Searching for WIMPs by the annual modulation signature. *Phys. Lett.*, B424:195–201, 1998.

[59] R. Bernabei et al. On a further search for a yearly modulation of the rate in particle dark matter direct search. *Phys. Lett.*, B450:448–455, 1999.

[60] A. Benoit et al. First Results of the EDELWEISS WIMP Search using a 320 g Heat-and-Ionization Ge Detector. *Phys. Lett.*, B513:15–22, 2001.

[61] D. S. Akerib et al. First results from the cryogenic dark matter search in the Soudan Underground Lab. *Phys. Rev. Lett.*, 93:211301, 2004.

[62] A. Bottino, F. Donato, N. Fornengo, and S. Scopel. Do current WIMP direct measurements constrain light relic neutralinos? *Phys. Rev.*, D72:083521, 2005.

[63] C. E. Aalseth et al. Experimental constraints on a dark matter origin for the DAMA annual modulation effect. *Phys. Rev. Lett.*, 101:251301, 2008.

[64] E. Behnke et al. Improved Spin-Dependent WIMP Limits from a Bubble Chamber. *Science*, 319:933–936, 2008.

[65] H. S Lee. et al. Limits on WIMP-nucleon cross section with CsI(Tl) crystal detectors. *Phys. Rev. Lett.*, 99:091301, 2007.

[66] H. S. Lee. Dark matter search with CsI(Tl) crystals. *AIP Conf. Proc.*, 870:208–211, 2006.

[67] G. Angloher et al. Limits on WIMP dark matter using scintillating CaWO-4 cryogenic detectors with active background suppression. *Astropart. Phys.*, 23:325–339, 2005.

[68] Anne M. Green and Ben Morgan. Optimizing WIMP directional detectors. *Astropart. Phys.*, 27:142–149, 2007.

[69] Craig J. Copi and Lawrence M. Krauss. Angular signatures for galactic halo WIMP scattering in direct detectors: Prospects and challenges. *Phys. Rev.*, D63:043507, 2001.

[70] N. J. C. Spooner, A. Bewick, G. J. Homer, P. F. Smith, and J. D. Lewin. Demonstration of nuclear recoil discrimination for low temperature dark matter detectors, by measurement of simultaneous ionization and thermal pulses in silicon. *Phys. Lett.*, B273:333–337, 1991.

[71] T. Shutt et al. Measurement of ionization and phonon production by nuclear recoils in a 60g crystal of germanium at 25-mK. *Phys. Rev. Lett.*, 69:3425, 1992.

[72] D. S. Akerib et al. Limits on spin-dependent WIMP nucleon interactions from the Cryogenic Dark Matter Search. *Phys. Rev.*, D73:011102, 2006.

[73] D. S. Akerib et al. Limits on spin-independent WIMP nucleon interactions from the two-tower run of the Cryogenic Dark Matter Search. *Phys. Rev. Lett.*, 96:011302, 2006.

[74] Z. Ahmed et al. Search for Weakly Interacting Massive Particles with the First Five-Tower Data from the Cryogenic Dark Matter Search at the Soudan Underground Laboratory. *Phys. Rev. Lett.*, 102:011301, 2009.

[75] S. Cebrian et al. First underground light versus heat discrimination for dark matter search. *Phys. Lett.*, B563:48–52, 2003.

[76] R. Bernabei et al. New limits on particle dark matter search with a liquid Xenon target-scintillator. *Phys. Lett.*, B436:379–388, 1998.

[77] R. Bernabei et al. Improved limits on WIMP Xe-129 inelastic scattering. *New J. Phys.*, 2:15, 2000.

[78] M. G. Boulay, A. Hime, and J. Lidgard. Design constraints for a WIMP dark matter and p p solar neutrino liquid neon scintillation detector. 2004.

[79] Y. D. Kim. The status of XMASS experiment. *Phys. Atom. Nucl.*, 69:1970–1974, 2006.

[80] G. J. Alner et al. First limits on nuclear recoil events from the ZEPLIN I galactic dark matter detector. *Astropart. Phys.*, 23:444–462, 2005.

[81] V. N. Lebedenko et al. Result from the First Science Run of the ZEPLIN-III Dark Matter Search Experiment. 2008.

[82] J. Angle et al. First Results from the XENON10 Dark Matter Experiment at the Gran Sasso National Laboratory. *Phys. Rev. Lett.*, 100:021303, 2008.

[83] R. Trotta et al. *New Astron. Rev.*, 51:316, 2007.

[84] John R. Ellis, Keith A. Olive, Yudi Santoso, and Vassilis C. Spanos. Update on the direct detection of supersymmetric dark matter. *Phys. Rev.*, D71:095007, 2005.

[85] D. S. Akerib et al. The SuperCDMS proposal for dark matter detection. *Nucl. Instrum. Meth.*, A559:411–413, 2006.

[86] H. Krauss et al. *J. Phys. Conf. Ser.*, 39:139, 2006.

[87] Katherine Freese, Joshua A. Frieman, and Andrew Gould. Signal Modulation in Cold Dark Matter Detection. *Phys. Rev.*, D37:3388, 1988.

[88] Richard H. Helm. Inelastic and Elastic Scattering of 187-Mev Electrons from Selected Even-Even Nuclei. *Phys. Rev.*, 104:1466–1475, 1956.

[89] S. Eidelman et al. Review of particle physics. *Phys. Lett.*, B592:1, 2004.

[90] S. Yellin. Finding an upper limit in the presence of unknown background. *Phys. Rev.*, D66:032005, 2002.

[91] Veronique Sanglard. Searches for Non-Baryonic dark matter using double- ionixation cryogenic detectors : Analysis and interpretation of data from Edelweiss-I. PhD, Université Claude Bernard -Lyon, France, 2007.

[92] A. Heister et al. Absolute mass lower limit for the lightest neutralino of the MSSM from e+ e- data at s**(1/2) up to 209-GeV. *Phys. Lett.*, B583:247–263, 2004.

[93] Mark W. Goodman and Edward Witten. Detectability of certain dark-matter candidates. *Phys. Rev.*, D31:3059, 1985.

[94] Laurent Chabert. Study of the background noise of neutrons induced by muons in the experiment EDELWEISS-II.

[95] V. Chazal et al. Neutron background measurements in the underground laboratory of Modane. *Astropart. Phys.*, 9:163–172, 1998.

[96] S. Fiorucci et al. Identification of backgrounds in the EDELWEISS-I dark matter search experiment. *Astropart. Phys.*, 28:143–153, 2007.

[97] T. Shutt et al. A solution to the dead-layer problem in ionization and phonon-based dark matter detectors. *Nucl. Instrum. Meth.*, A444:340–344, 2000.

[98] P.N. Luke. *IEEE Trans. Nucl. Sci.*, NS-42:207, 1995.

[99] X. Defay. *J. Low Temp. Phys.*, 151:896, 2008.

[100] Oliver Markus Horn. Simulations of the muon-induced neutron background of the EDELWEISS-II experiment for dark matter search. FZKA-7391.

[101] A. Juillard. Résolution dans des bolomètres équipés de couches minces d'isolant d'Anderson pour des événements impliquant des reculs de noyaux. PhD, CEA Saclay, DSM/DAPNIA/SPP, France, 2005.

[102] A. Juillard et al. Development of Ge/NbSi detectors for EDELWEISS-II with identification of near-surface events. *Nucl. Instrum. Meth.*, A559:393–395, 2006.

[103] B. Censier, A. Broniatowski, A. Juillard, L. Berge, and L. Dumoulin. Surface trapping and detector degradation in Ge bolometers for the EDELWEISS Dark Matter search: experiment and simulation. *Nucl. Instrum. Meth.*, A520:156–158, 2004.

[104] P.N. Luke. *IEEE Trans. Nucl. Sci.*, NS-41:1074, 1994.

[105] G. F. Knoll. RADIATION DETECTION AND MEASUREMENT. New York, USA: John Wiley & Sons (2000) 816 p.

[106] P.N. Luke. *J. Appl.Phys.*, 64:6858, 1988.

[107] E. Simon et al. SICANE: A detector array for the measurement of nuclear recoil quenching factors using monoenergetic neutron beam. *Nucl. Instrum. Meth.*, A507:643–656, 2003.

[108] P. Di Stefano et al. Background discrimination capabilities of a heat and ionization germanium cryogenic detector. *Astropart. Phys.*, 14:329–337, 2001.

[109] S. Fiorucci. Acquisition et Analyse des données pour léxpérience de recherche de matière noire EDELWEISS. PhD, Université Paris XI, France, 1999.

[110] O. Martineau et al. Calibration of the EDELWEISS cryogenic heat-and-ionisation germanium detectors for dark matter search. *Nucl. Instrum. Meth.*, A530:426–439, 2004.

[111] A. Broniatowski et al. A new high-background-rejection dark matter Ge cryogenic detector. 2009.

[112] M. Luca. Sapphire Scintillation Tests for Cryogenic Detectors in the EDELWEISS Dark Matter Search. PhD, Université Claude Bernard -Lyon, France, 2007.

[113] S. Agostinelli et al. GEANT4: A simulation toolkit. *Nucl. Instrum. Meth.*, A506:250–303, 2003.

NOM : SCORZA
(avec précision du nom de jeune fille, le cas échéant)
Prénoms : Silvia

DATE de SOUTENANCE

6 novembre 2009

TITRE : EDELWEISS-II, direct Dark Matter search experiment : first data analysis and results

Numéro d'ordre : 199-2009

DIPLOME DE DOCT.	DOCTEUR-INGENIEUR	DOCTORAT D'ETAT	DOCTORAT DE 3e CYCLE
X	☐	☐	☐

Spécialité : Physique des Particules

Cote B.I.U. – Lyon : T 50/210/19 / et bis

CLASSE :

RESUME : One of the greatest mysteries of the universe that, for the present, puzzles the mind of most astronomers, cosmologists and physicists is the question: "What makes up our universe?". This is due to how a certain substance named Dark Matter came under speculation. It is believed this enigmatic substance, of type unknown, accounts for almost three-quarters of the cosmos within the universe, could be the answer to several questions raised by the models of the expanding universe astronomers have created, and even decide the fate of the expansion of the universe.

There is strong observational evidence for the dominance of non-baryonic Dark Matter (DM) over baryonic matter in the universe. Such evidence comes from many independent observations over different length scales. The most stringent constraint on the abundance of DM comes from the analysis of the Cosmic Microwave Background (CMB) anisotropies. In particular, the WMAP (Wilkinson Microwave Anisotropy Probe) experiment restricts the abundance of matter and the abundance of baryonic matter in good agreement with predictions from Big Bang Nucleosynthesis.

It is commonly believed that such a non-baryonic component could consist of new, as yet undiscovered, particles, usually referred to as WIMPs (Weakly Interacting Massive Particles). Some extensions of the standard model (SM) of particle physics predict the existence of particles that would be excellent DM candidates. In particular great attention has been dedicated to candidates arising in supersymmetric theories: the Lightest Supersymmetric Particle (LSP). In the most supersymmetric scenarios, the so-called neutralino seems to be a natural candidate, being stable in theories with conservation of R-parity and having masses and cross sections of typical WIMPs.

The EDELWEISS collaboration is a direct dark matter search experiment, aiming to detect directly a WIMP interaction in a target material, high purity germanium crystal working at cryogenic temperatures. It relies in the measurement of nuclear recoils that produce measurable effects in the crystal such ionization and heat.

My PhD thesis is organized as follows. The first chapter aims to provide an introduction to the theoretical framework and the scientific motivation for the following work. The nature of DM has been one of the most challenging topics in contemporary physics since the first evidences of its existence had been found in the 1930s. Cosmologists and astrophysicists on one side, together with particle theorists on the other have put a lot of effort into this field: I will briefly account for their achievements and for the experimental strategies which can be set in this scenario. Since this thesis work was carried out within the EDELWEISS-II direct dark matter experiment, I will focus the next chapter on this topic, describing the main features.

The second chapter is related to the set-up of the EDELWEISS-II, the current stage of the EDELWEISS experiment necessary after a first phase that achieved the best upper limit on the WIMP elastic scattering on nucleon as a function of WIMP mass in 2004. The set-up was conceived to reduce radioactive background observed in the first experiment phase. Thus, describing the starting point for this second stage, I will present detectors involved in, with a peculiar regard to the Ge-NTD type, the same implied in EDELWEISS-I, on which I have focused my thesis work.

In the third chapter the performed Ge-NTD analysis chain is presented. Starting with the signal processing of the recorded data, I will enter in the essential analysis steps from calibration signals passing through measurements of thresholds and resolutions in order to predict nuclear and electronic recoil band and definition of fiducial zone to conclude determining a selection for likely WIMP candidate.

These suggestions are applied in the fourth chapter, which presents the analysis and the results of the 8th cool down that takes places from November 2007 to March 2008. This cool down allows a first real look at the EDELWEISS-II environment and it represents a first real test of Ge-NTD type detectors at large scale. Thus, it follows that two goals are envisaged: a better understanding of radiative background overwhelming the experiment and an improvement of current upper limit on the WIMP scattering cross section.

MOTS-CLES : astroparticules – matière noire – détection directe de WIMPS – détecteurs cryogéniques

Laboratoire de recherche : Institut de Physique Nucléaire de Lyon

Directeurs de recherches : Jules Gascon

Président du jury : B. Ille
Composition du jury : J. Gascon – G. Gerbier – A. Giuliani – J. Jochum

141 pages